Dissertation
submitted to the
Combined Faculties for the Natural Sciences and for Mathematics
of the Ruperto-Carola University of Heidelberg, Germany
for the degree of
Doctor of Natural Sciences

presented by
Dipl.-Phys. Siegfried Falter
born in: Amberg
Oral examination: July 26, 2006

Searching for Distant Galaxy Clusters:
Optical Observations, Cluster Search Algorithms and the Cluster Selection Function.

Referees: PD Dr. Hermann-Josef Röser
Prof. Dr. Matthias Bartelmann

Abstract

HIROCS is a multi-color survey designed to construct a statistically significant galaxy cluster sample for galaxy evolution studies using a multi-color classification scheme in the redshift range $0.5 < z < 1.5$. After contributing to the survey specifications, tests of the multi-color classification with the observational setup showed the feasibility of the project. The photometric redshift accuracy of $\delta_z = 0.076$ was estimated at the R band limit of ∼25 mag. The new algorithm for the galaxy cluster detection was developed and tested with COMBO-17 data. In the three COMBO-17 fields covering 0.78 square degrees 15 cluster candidates were identified in the redshift range $0.3 < z < 0.9$. The power of the search method was demonstrated by a comparison with the cluster detections from the Voronoi tessellation. For the determination of the cluster selection function in HIROCS and COMBO-17 procedures to simulate galaxy clusters were introduced. Due to the lack of fully reduced HIROCS data, the COMBO-17 selection function was quantified; rich clusters are expected to be found in the redshift range covered by COMBO-17. First steps towards an analysis of cluster candidates were carried out using the COMBO-17 candidates. Finally, a rich cluster at redshift ∼0.7 was identified in the first HIROCS infrared data.

Zusammenfassung

HIROCS ist eine Mehrfarbendurchmusterung, um einen statistisch signifikanten Galaxienhaufenkatalog bei Rotverschiebungen zwischen 0.5 und 1.5 für Studien der Galaxienentwicklung zur Verfügung zu stellen. Photometrische Rotverschiebungen werden durch eine Mehrfarbenklassifikation bestimmt. Zu Beginn wurden Teile der Beobachtungsspezifikationen durchgeführt. Tests der Mehrfarbenklassifikation unter den Spezifikationen der Beobachtungen zeigten die Machbarkeit des Projekts. Die Genauigkeit der Rotverschiebungen bei der Grenzhelligkeit im R-Filter von ∼25 mag wurde mit $\delta_z = 0.076$ abgeschätzt. Es wurde eine neue Suchmethode für Galaxienhaufen vorgestellt und mit Daten der COMBO-17-Durchmusterung getestet. In den drei Feldern, die 0.78 Quadratgrad abdecken, wurden 15 Galaxienhaufen im Rotverschiebungsbereich $0.3 < z < 0.9$ identifiziert. Anhand einer Vergleichsstudie mit der sogenannten "Voronoi tessellation" wurde die Leistung der neuen Methode demonstriert. Die Methodiken zur Bestimmung der Auswahlfunktion von Galaxienhaufen wurden für HIROCS und COMBO-17 vorgestellt. Aufgrund des Fehlens eines vollständig reduzierten HIROCS-Datensatzes konnte die Auswahlfunktion nur für COMBO-17 erarbeitet werden. Danach können alle reichen Galaxienhaufen im von COMBO-17 abgedeckten Rotverschiebungsbereich gefunden werden. Erste Schritte zur Analyse von Galaxienhaufen wurden anhand der Haufenkandidaten aus COMBO-17 vorgenommen. Schließlich wurde während der Reduktion der Infrarotdaten des ersten HIROCS-Datensatzes ein reicher Galaxienhaufen bei Rotverschiebung 0.7 gefunden.

Contents

Chapter 1

Introduction

Galaxy clusters are the largest gravitationally bound systems in the Universe. These systems of several hundred to even a few thousand galaxies for the richest clusters formed from Gaussian density perturbations in the matter field during the early phases of the Universe. The highest density peaks collapsed at the earliest times to form the first galaxies and accumulated more and more matter later on to form the galaxy clusters. All this is described by the picture of the hierarchical structure formation where small units are built up first which then merge to build even larger units.

The structure of the Universe, traced by the galaxies, appears as a foam-like web (Fig. 1.1). Galaxies are preferably found in filaments and at the crossings of these filaments groups as well as clusters of galaxies have formed. In the picture of the hierarchical structure growth, the galaxies fall first onto the filaments and then stream towards the groups/clusters. The galaxy density thus increases from filaments to groups to clusters. The latter are the highest density peaks in the Universe. Between these building blocks of the cosmic web there are large, almost empty regions which are called voids. The size of voids is on the order of 25 Mpc, rich galaxy clusters extend over 3 to 10 Mpc, and galaxy groups over 1 to 2 Mpc. For more details about general cluster properties see Bahcall (1999).

The first galaxy clusters were recognized as associated objects even before Hubble discovered the extragalactic nature of the nebulae in the 1920s. In 1901, Max Wolf discovered the Coma galaxy cluster with the Bruce telescope of the Königstuhl Observatory as a "strange agglomeration of nebulae" on a photographic plate. Zwicky (1933) measured the radial velocities of galaxies in the Coma galaxy cluster from their redshifted spectra. On the basis of the Virial theorem the mass of a galaxy cluster can be estimated with the before mentioned redshift measurements. It was found that a large amount of matter is not visible in the form of galaxies. This was the first discovery of dark matter. Clusters contain baryonic matter not only in the stars and gas inside galaxies but also

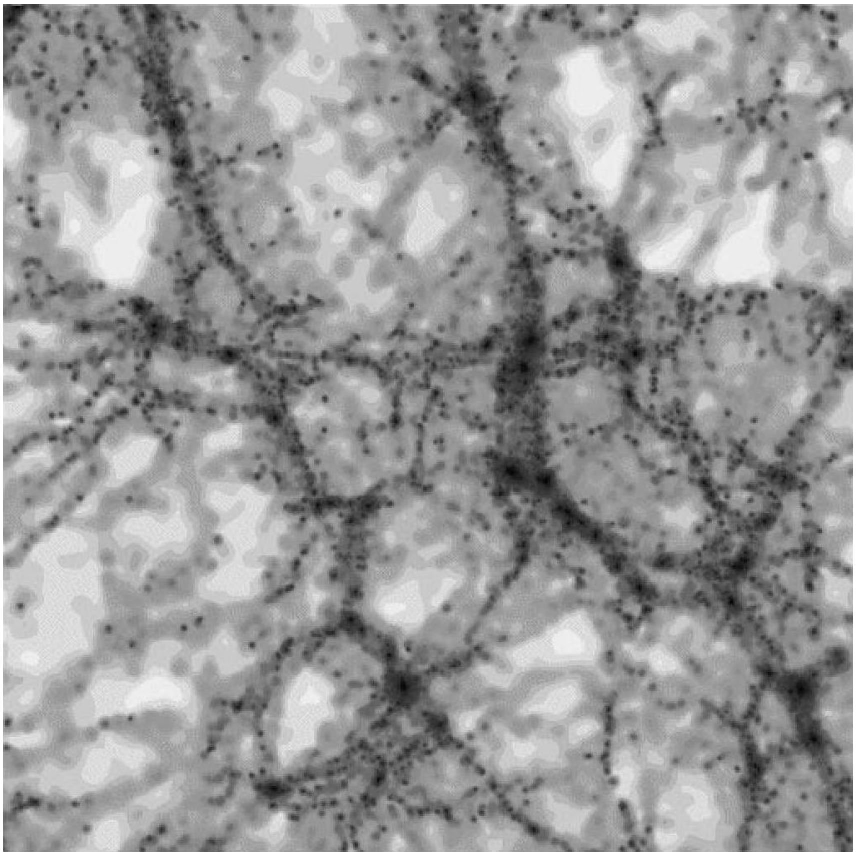

Figure 1.1: Cut through the dark matter distribution (slice thickness: 8 h^{-1} Mpc) from a cosmological simulation (Kauffmann et al., 1999). White to light grey regions are the voids. Filaments are the long structures appearing dark grey. At the crossings of filaments groups and clusters of galaxies are found as dark grey to black knots of dark matter particles. Density increases from white to black in the coding.

large amounts are found as a hot gas ($\sim 10^6 - 10^8$ K) in the intra-cluster medium which is detected by its free-free emission of X-ray photons. 15% of the total cluster mass is found in the hot gas of the intra-cluster medium while galaxies make up a smaller mass fraction. The largest contribution, up to a mass fraction of ~80%, comes from the dark matter. All these constituents form a deep gravitational potential well which is dominated by the dark matter contribution. Galaxy clusters are rare objects in terms of the galactic content; only around 5% of the bright galaxies in the Universe are part of rich clusters. However, about half of all galaxies are found in less rich systems like galaxy groups.

Galaxy clusters as scientific probes

Galaxy clusters as the most massive quasi-equilibrium objects in the Universe serve as probes for two different branches of extra-galactic research. The first branch deals with the galaxy evolution in general and with the peculiarities of the evolution of galaxies in clusters. Clusters as single objects provide a sample of galaxies with different masses/luminosities at the same redshift and close together so that they are easy to observe. At high redshifts beyond 0.5, however, it is increasingly difficult to identify clusters due to superpositions of fore- and background galaxies.

The dense galaxy environment and the presence of the hot intra-cluster gas have a strong influence on the properties of galaxies in clusters. For example, cD galaxies, which are extraordinarily extended elliptical galaxies with a large halo of stars and are found in the centers of clusters, are assumed to be formed exclusively in clusters. When studying galaxy evolution in clusters the environmental effects have to be taken into account. These effects comprise interactions of the gas and the stars of a galaxy, that travels through the galaxy cluster, with the cluster gas (e.g "ram-pressure stripping") and the cluster gravitational potential (e.g. "harassment" = frequent high-velocity encounters). As a result, gas and stars are transferred to the intra-cluster medium and the galaxy properties are altered.

Some properties of galaxies are only observed in dense galaxy environments. Elliptical and lenticular (S0) galaxies (early-type galaxies) are found preferentially in the cores of clusters while spiral galaxies (late-type galaxies) tend to populate the outskirts. This finding is termed the *morphology-density relation* and was quantified in a study of Dressler (1980) for the first time. Recently, Postman et al. (2005) showed that the *morphology-density relation* is already in place at high lookback times at a redshift of 1.0. Elliptical galaxies appear to have formed within a short period at early times (z=2−4) of the Universe and evolved passively to the present day (van Dokkum et al., 2003). Since this seems to be un-physical to some extent, the hierarchical build up by galaxy merging and collisions has to play a role (White & Frenk, 1991). These galaxies are thus old, non-starforming galaxies which fade with time. In addition, the fraction of elliptical/S0 galaxies is significantly higher compared to the field galaxy environment. van Dokkum et al. (2000) published a collection of early-type fractions up to redshifts of ∼0.8 for several clusters. While the early-type fraction is about 30% in the field, in cluster centers it can be as high as 80%. This trend, though weaker, is observed yet at high redshifts beyond 0.5.

Moreover, there is redshift evolution of cluster properties observed. Butcher & Oemler (1984) measured the fraction of blue galaxies in clusters up to redshifts of 0.5 and found an increase of the blue fraction. How to quantify the so-called *Butcher-Oemler effect* is under debate since its discovery. Because is it is hard to measure due to projection

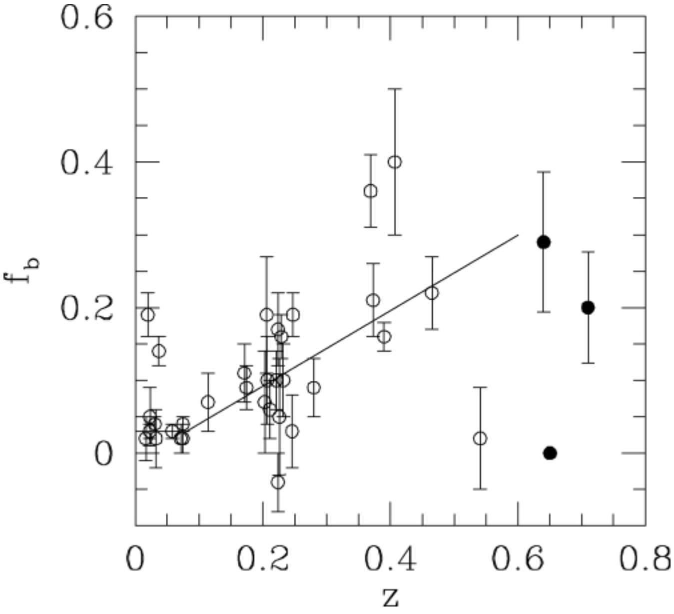

Figure 1.2: Blue galaxy fraction as a function of redshift (*Butcher-Oemler effect*) from (Andreon et al., 2004).

effects and color segregation within clusters (Andreon et al., 2004), the amplitude of the *Butcher-Oemler effect* is insecure (see Fig. 1.2). These problems cause a large spread of estimated blue fractions for clusters at different redshifts if not the same selection criteria are used by different authors.

The luminosity function is one of the most important tools for the study of the evolution of galaxies in different environments and at all redshifts. There is a continued debate about the universality of the luminosity function in all environments. On the one hand, many findings support the idea that it is universal, e.g. Paolillo et al. (2001) and Andreon (2004). Amongst others, Christlein & Zabludoff (2003) or Goto et al. (2002) on the other hand have found significant differences between luminosity functions of different clusters and between clusters and the field.

Galaxies show a bimodal color distribution in the color-magnitude diagram irrespective of environment. There is a blue and a red peak in this diagram. Blue galaxies populate a broader region which is often called the blue cloud. The so-called red-sequence is a relation with low scatter in this diagram which is formed by red and non-starforming early-type galaxies. The origin of the red-sequence galaxies can be understood by an initial single starburst at early times, or high redshifts of ∼3, respectively, and the subsequent passive

fading of the stars in these galaxies. A detailed study of the red-sequence and its evolution over the redshift range $0.2 < z < 1.1$ was published by Bell et al. (2004) based on the COMBO-17 (Classifying Objects by Medium-Band Observations in 17 filters) survey.
The second research branch, which is not topic in this doctoral thesis, is the study of the large-scale structure and the role of clusters in constraining cosmological models. The study of their number density as a function of mass and redshift provides a tool to decide between different cosmological parameters. P. Schücker provided a review article about this topic (Schücker, 2005). In concert with complementary studies of the cosmic microwave background and supernova Ia, accurate estimations of these cosmological parameters were achieved. The Universe is best described by the so-called Λ Cold Dark Matter model (ΛCDM) with a cosmological constant Λ and with dark matter which only interacts via gravity.

Finding galaxy clusters

Galaxy evolution studies along these lines for large cluster samples rely on the availability of homogeneously selected cluster catalogues. Many studies were based on the Abell (1958) catalogue and its southern extension (Abell et al., 1989) which were constructed by visual selection on photographic plates. Zwicky et al. (1968) created another catalogue of galaxy clusters by inspection with the human eye. The problem about this selection procedure is the incompleteness and the lack of reproducibility. Furthermore, for large amounts of data it is slow and the selection function is extremely difficult to quantify.
With the advent of plate scanning machines and optical as well as near infrared detectors in the 1980s and 1990s, automated search methods became possible. The APM Cluster Survey (Dalton et al., 1997) was one of the surveys that made use of data from automatically scanned photographic plates. The detector technology provided the possibility of taking uniform and much deeper data sets. At the beginning the detector formats were rather small (the optical CCDs had a lead over the infrared detectors until the late 1990s). Resulting from this, only small sky areas could have been covered. To give an example, the Palomar Distant Clusters Survey (PDCS), Postman et al. (1996), covered a sky area of 5.1 square degrees. Large cluster catalogues at redshifts below 0.5 were constructed later on using the Sloan Digital Sky Survey or SDSS (York et al., 2000). Goto et al. (2002) selected clusters on 350 square degrees on the basis of the SDSS early data release.
The first automatic cluster search was a counts-in-cells method (Shectman, 1985) where galaxies were counted in cells on the sky to estimate the galaxy density. An also parametric approach, which was widely used up to now, is the so-called matched-filter algorithm (Postman et al., 1996) which was developed for the PDCS. This technique applies a radial profile for the cluster and a luminosity function for its member galaxies as a filter. To

separate the cluster galaxies the likelihood of matching the cluster model to the observations is maximized. Assuming certain input parameters is a drawback for the detection of clusters because the findings will be biased to clusters that match these parameters.

Another approach for the cluster detection is to benefit from the tight color-magnitude relation of the early-type galaxies. The Red-sequence Cluster Survey (RCS), initialized by Gladders & Yee (2000), was doing a cluster search on 100 square degrees with observations in only two filters (R_c, z'). Basically, the technique searches for enhanced galaxy densities in overlapping color slices where red-sequences of clusters are expected as a function of redshift. Limited by the optical filters, the survey can extend to slightly higher redshifts than 1.0. This technique is sensitive to clusters with sufficiently pronounced red-sequences but may miss clusters with low fractions of early-type galaxies.

The friends-of-friends technique identifies excesses of number densities in three dimensions (3D) by searching for galaxy pairs. These pairs have to be closer than a predefined separation limit. It was applied exclusively to spectroscopic redshift surveys, e.g. Ramella et al. (2002), or N-body simulations, e.g. Valageas, Lacey, & Schaeffer (2000), until C. Botzler modified it within her PhD thesis (Botzler, 2004) for the MUNICS (Botzler et al., 2004) survey. This modified "extended friends-of-friends algorithm" enabled the use of photometric instead of spectroscopic redshifts. Several other finding methods were introduced over the last years which shall be mentioned here: the "cut-and-enhance method" (Goto et al., 2002) which uses color cuts and an algorithm for density enhancement, the "C4 algorithm" (Miller et al., 2005) searches for clusters in a seven dimensional position and color space which should minimize projection effects.

Galaxy clusters are detectable also on the basis of their X-ray emission of the hot intra-cluster gas. The detection in this wavelength regime has the advantage that the emission is proportional to the square of the gas density. Furthermore, projection effects are by far less severe than in the optical – most extragalactic, extended X-ray objects are galaxy clusters. However, the detection of clusters in the X-rays may be biased compared to the optical selection. The emission process is enhanced during and after evolutionary phases like galaxy cluster mergers where the compression and shocks of the intra-cluster gas can boost the X-ray brightness. Comparison studies of optically and X-ray selected clusters yield interesting insights in the properties of the gas and the galaxies in clusters, see e.g. Lopes et al. (2006).

Two further techniques, which may be important in the future, can be used for detecting clusters and were refined over the last years. The first one benefits from the effect that galaxy clusters imprint signatures on the structures of the Cosmic Microwave Background (CMB). The so-called Sunyaev-Zeldovich effect (Sunyaev & Zeldovich, 1980) is the Compton scattering of photons emitted at the recombination epoch off the free electrons of the intra-cluster medium in galaxy clusters. This causes a deficit of CMB photons in the direction of clusters. The drawbacks are the weakness of the amplitudes and the confusion with other sources of temperature fluctuations in the CMB. Since the Sunyaev-Zeldovich effect is a scattering effect, its magnitude is independent of redshift which is important to find clusters out to high redshifts. Up to now, no clusters have been discovered with the Sunyaev-Zeldovich effect. Techniques for the cluster detection and the data analysis of high redshift clusters are under development (Mohr, 2005).

A second important technique for the future is based on the weak lensing of a suitable sample of background galaxies caused by a galaxy cluster in the foreground. The deflection of the light from the background sources by the cluster gravitational potential induces tiny changes of the galaxy shapes. Due to its weakness, the effect is hard to measure. A pre-requisite to detect a cluster with weak lensing is the presence of suitable background galaxy distribution at higher redshifts. This fact complicates the application to detect high redshift clusters, especially at redshifts beyond unity. Very deep surveys with cameras having wide field-of-views are thus needed. Additionally, excellent seeing conditions are required to be able to measure the weak lensing signal (Hamana, 2005).

Considering all the detection methods with their advantages and drawbacks, complementary search results can be expected for future studies of galaxy clusters on samples from different search techniques.

The main problem of cluster finding in the optical/near infrared at increasing redshifts is the fore- and background galaxy contamination. Clusters have to be filtered out of this background efficiently by the search method. Otherwise, the cluster catalogue will be affected by a contamination of spurious cluster detections or many clusters are missed. The best way would be a spectroscopic survey because redshifts measured from galaxy spectra are most accurate. Such a survey is not feasible on large sky areas of several square degrees due to the long exposure times and due to the necessary object pre-selection. Because of the availability of photometric redshift determinations on the basis of multi-band photometry (Wolf et al., 2001), dedicated imaging surveys can yield large cluster samples. Imaging surveys are unbiased because no object selection is done in advance. Using the photometric redshifts, a new 3D detection algorithm was developed for the cluster search project presented in this PhD thesis. The strength of this algorithm is the incorporation of the photometric redshifts and, at the same time, the redshift errors for each galaxy in a given object table. This strategy helps minimizing the background contamination problem. Furthermore, the code is fast in terms of CPU time. The speed of the algorithm allows the determination of the selection function by means of a large number of simulated clusters.

Another essential ingredient to find galaxy clusters at redshifts beyond unity is the availability of large near infrared detector arrays. The 4 000Å break is shifted into the infrared for galaxies at these high redshifts. This makes the use of infrared observations necessary. Large-format near infrared detectors like the HAWAII2 detector, which is used for the OMEGA2000 camera at the Calar Alto 3.5m telescope, are available only since the beginning of this century. The field-of-view of $\sim 15' \times 15'$ of OMEGA2000 is vital to be able to cover the large sky areas for a galaxy cluster survey.

The way to the HIROCS project

At low redshifts up to 0.5 large homogeneously selected cluster samples, e.g. from the SDSS (Miller et al., 2005, worked on 2 600 square degrees), do exist. Also at redshifts up to 1.1 significantly large cluster searches were carried out like the RCS (100 square degrees) or are ongoing like the ESO Distant Cluster Survey (White et al., 2005). However, at redshifts significantly beyond unity no large homogeneously selected cluster sample exists yet. The reason was the lack of large area near infrared detectors which became available only in the past few years. Galaxy clusters in the redshift regime $0.8 < z < 1.4$ were found mostly from serendipitous X-ray surveys, like the cluster MS 1054−03 at $z = 0.83$ (van Dokkum et al., 2000) or XMMU J2235.3−2557 at $z = 1.39$ (Mullis et al., 2005). With the infrared space observatory *Spitzer*, an infrared selected cluster at redshift 1.41 was presented recently by Stanford et al. (2005).
In light of the above mentioned galaxy evolution studies, galaxy cluster samples at these high redshifts will give new insights into the evolution of galaxy properties. First results were obtained for the single clusters but a more systematic study needs homogeneous samples based on infrared observations. Motivated by this, the Heidelberg InfraRed/Optical Cluster Survey (HIROCS) was developed to create such a sample of high redshift galaxy clusters.
But what lead to the invention of HIROCS? During the last 12 years multi-band imaging has been used for the study of galaxy clusters at intermediate redshifts as well as for galaxies in the field at the MPIA. Multi-band and Fabry-Perot imaging was used before for the study of galaxy populations in clusters at intermediate redshifts, see Thimm et al. (1994), Belloni et al. (1995), and Belloni & Röser (1996). These techniques were developed further and refined for the Calar Alto Deep Imaging Survey (CADIS) and the COMBO-17 survey. Regarding the large number of objects – several 10 000s of galaxies – the object classification and accurate estimation of redshifts (Wolf et al., 2001) up to the survey limit based on the multi-color data is one of the most important tools for such projects.
Finally, the development of OMEGA2000 paved the way for a galaxy cluster survey at redshifts significantly beyond unity. In combination with the Large Area Imager for Calar Alto (LAICA) and the WFI working in the optical, the suitable instrumentation is available. All this lead to the HIROCS project which is described in this thesis.

The author joined the project in April 2003 after its basic definition phase. The main goals of this PhD thesis are the following:

- optical observations in concert with data reduction and photometric calibration,
- refinement of the newly developed 3D galaxy cluster search method, and
- development of procedures for the evaluation of the cluster selection function

During the PhD time of the author, the optical observations were hampered by instrument problems as well as bad weather. The delay of the project did not allow the use of HIROCS survey data to be used for the application of the cluster search technique. The first data will be available only after the PhD time.

In the mean time, COMBO-17 data serve as a test ground for tests of the multi-color classification and the cluster search algorithm. This survey offers a multi-color data set in 17 optical filters covering 0.78 square degrees of sky at high galactic latitudes. All observations were conducted with the Wide Field Imager (WFI) at the MPG/ESO 2.2m telescope on La Silla, Chile (sky area covered: $34' \times 33'$). The filter set includes 5 broad band ($U\,B\,V\,R\,I$) and 12 medium band filters covering the wavelength range from 350 to 930 nm. COMBO-17 is designed to study galaxy evolution at redshifts $\mathrm{z} \leq 1.2$ within three disjoint fields: the Chandra Deep Field South (CDFS), the equatorial field named S11 and the third field is centered on the low redshift super-cluster A901/A902. Altogether ∼160 ksec of exposure time were taken in the complete filter set. The R band exposure is the deepest exposure with 20 ksec integration time with seeing below $0.8''$. More details about the sample selection, redshift estimation, calculation of rest-frame luminosities, red-sequence evolution, and completeness were published in Wolf et al. (2001), Wolf et al. (2003), Wolf et al. (2004), and Bell et al. (2004).

The doctoral thesis is structured along the following lines:

Chapter 2 gives the basic survey definition including the motivation of the HIROCS survey area, the choice of the filter set, and the calculation of the required depth of the observations. After that the observational issues like the selection of suitable fields, the instruments in use as well as the basic data reduction procedures, and the strategy of the photometric analysis are presented in Chapter 3. Two basic methods are the key ingredients for HIROCS. These are the multi-color classification scheme and the 3D cluster finding technique which are explained in Chapter 4. For the detailed understanding of the galaxy cluster selection procedure and its selection function simulations of clusters are performed. The setup of these simulations for HIROCS and COMBO-17 are found in Chapter 5 where for COMBO-17 the selection function is presented, too. Since no calibrated HIROCS data set was available in the last months of the thesis the cluster finding was applied in three fields of the COMBO-17 survey to test the procedures developed within the thesis work. The search results are described in Chapter 6. Comparison studies of cluster finding techniques provide valuable information about strengths and weaknesses of the selection techniques. For one example field from COMBO-17 the search results from the newly developed 3D algorithm is compared with the Voronoi tessellation technique (Chapter 7). A more detailed analysis of the COMBO-17 cluster candidates was carried out and is presented in Chapter 8. During the data reductions of the first HIROCS data set on 1 square degree of the 03h field the first cluster candidate was identified. Its detection and first analysis is introduced in Chapter 9.

Throughout this thesis, a cosmology in which $\Omega_m = 0.3$, $\Omega_\Lambda = 0.7$, and $H_0 = 72\,\mathrm{km\,s^{-1}}$ $\mathrm{Mpc^{-1}}$ is assumed. The Hubble constant is given in dimensionless form: $\mathrm{h} = \frac{H_0}{100} = 0.72$.

Chapter 2

The Heidelberg InfraRed/Optical Cluster Survey

The Heidelberg InfraRed/Optical Cluster Survey (= HIROCS) is a multi-color survey designed to homogeneously select galaxy cluster candidates in the redshift range $0.5 < z < 1.5$. HIROCS is part of the large MPIA key programme MANOS (= MPI for Astronomy Near-infrared Optical Surveys). The overall aim of the programme is to study the evolution of galaxies as a function of time and local galaxy density. MANOS is split into two independent sub-projects. MANOS-deep is an extension of the existing COMBO-17 optical data base with deep exposures in four infrared filters. It is going to cover approximately 0.77 square degrees and is also named COMBO-17+4. HIROCS (or MANOS-wide) is imaging less deep compared to COMBO-17+4 but covers a much larger area with 11 square degrees. It uses five filters in the optical/near infrared regime.

The space density of rich clusters is very low and at redshifts beyond 1.0 no large-area cluster sample is known to date. For the creation of a statistically significant cluster catalogue a large area of the sky has to be imaged with deep exposures to measure the flux for very faint objects at redshifts beyond unity. Two basic steps which are discussed in this Chapter have to be undertaken to achieve the survey goals. First an estimation of the expected number of clusters per redshift range and unit sky area leads to the desired survey sky coverage to obtain a significantly large cluster sample. The second step involves the calculation of the required exposure times to be able to measure cluster galaxies to a certain limit of the luminosity distribution. These two issues are the pre-requisite to carry out the HIROCS observations.

2.1 Survey area and filter set

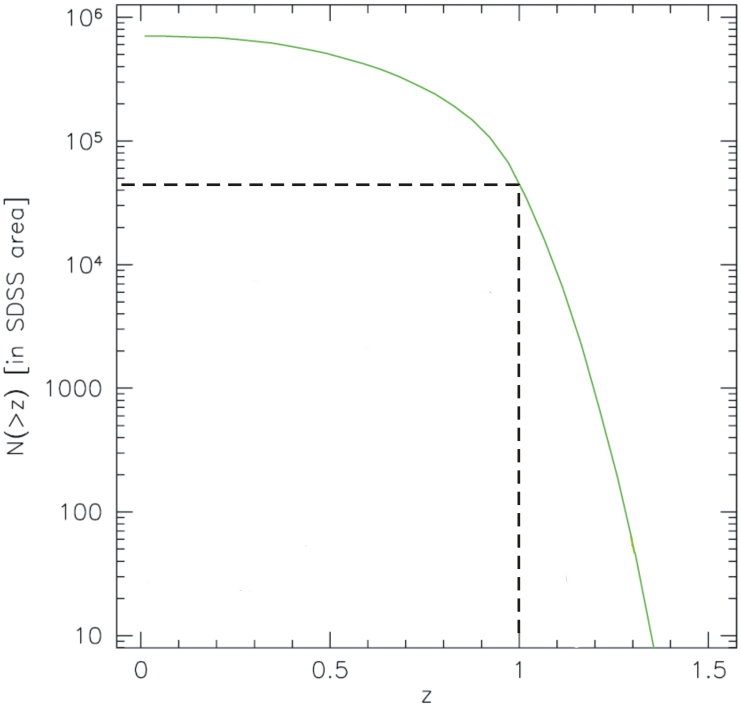

Figure 2.1: Cumulative redshift distribution (green curve) N(>z) of galaxy clusters with $M \geq 5\times 10^{13}\,M_\odot$ from Bartelmann & White (2002). For the calculations summed r'+i'+z' SDSS data have been used. The clusters are detected at 2σ significance. The black dashed line is the limit for the estimation of the expected total number of clusters at redshifts beyond unity.

The following explanations concerning the choice of the survey area and the filter set were published in Röser, Hippelein & Wolf (2004).
Bartelmann & White (2002) made predictions for the number of expected galaxy clusters as a function of redshift for the Sloan Digital Sky Survey (SDSS). The cumulative redshift distribution shown in Fig. 2.1 is exploited for estimating the number of clusters with redshifts beyond unity. Here the estimation is based on the cluster detections on the 2σ significance level. While the stacking of the three SDSS bands which was applied for the Bartelmann & White study served to enhance the image depth for the cluster finding, the significantly longer HIROCS exposure times will certainly reveal more clusters. HIROCS clusters shall be detected at the 3σ over-density level. Expressed in numbers,

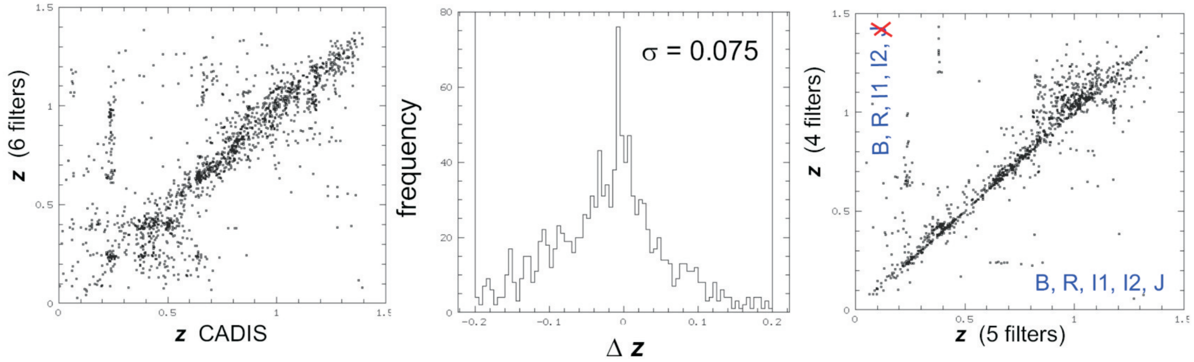

Figure 2.2: Filter selection procedure at survey layout planning: Comparison of classification results from a reduced filter set as it will be used in HIROCS with the results from the full CADIS data set. The photometric redshifts from CADIS are compared with those derived with a HIROCS-like filter set (B, R, CADIS $I1$, CADIS $I2$, and J) plus the zJ filter (left panel). The central panel shows the resulting uncertainty in photometric redshift using these six filters. As could be shown, the information provided by the zJ filter is redundant and it can be omitted. However, if the J band is also dropped, the redshifts above unity become very uncertain (right).

at redshift 1.0 N(>z) yields approximately 40 000 clusters in the total SDSS survey area of more than 8 000 square degrees. Based on these numbers and the envisioned depth of the HIROCS data more than five clusters per square degree are expected at these redshifts. Consequently a minimum of 10 square degrees is necessary to yield a statistically significant cluster sample of more than 50 clusters with $z > 1.0$ in the whole survey area. In total HIROCS will cover a field size of 11 square degrees. The detailed field selection procedure is explained in Chapter 3.

After fixing the necessary sky coverage first feasibility tests of the multi-color classification on a suitable filter set were performed. The CADIS survey provides an imaging data set including observations in the infrared using the J band. These tests were done on the CADIS-01h field by reducing the number of filters to several different subsets and reclassifying all objects with $I < 23$ mag. The comparison of the original redshifts with the ones from a reduced data set is shown in Fig. 2.2. The final HIROCS filter set is B, R, SDSS-i, SDSS-z, and H (see Fig. 2.3). The filters CADIS $I1$ and CADIS $I2$ had to be replaced by the SDSS filters because LAICA (see Sect. 3.2) is not equipped with the CADIS filters and these are equivalent in terms of effective wavelength. To reach a redshift of 1.5 the J band would be sufficient but the H band provides the possibility to go out to even higher redshifts. Since the 4000 Å break is shifted into the infrared for

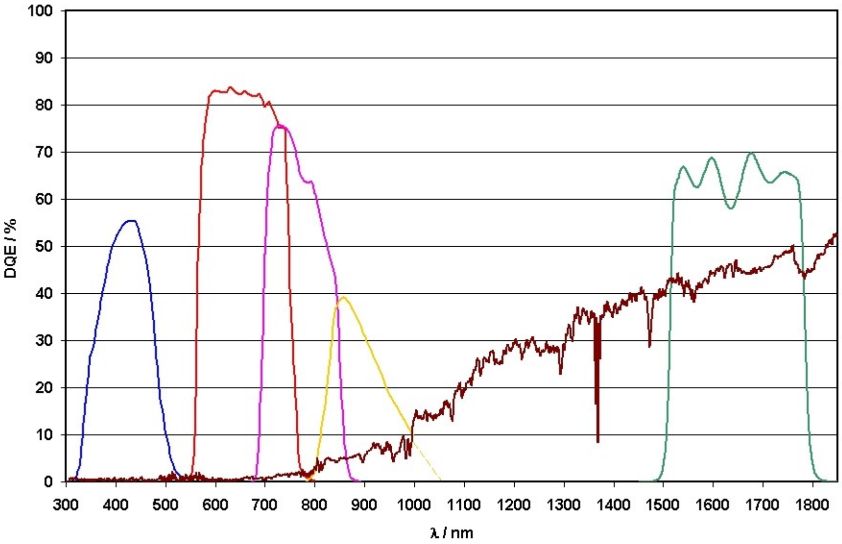

Figure 2.3: The HIROCS filter set: *B* (blue), *R* (red), SDSS-i (magenta), SDSS-z (yellow), *H* (green). The transmission curves for the optical filters are already convolved with the CCD quantum efficiency (vertical axis DQE in %). For illustrating the importance of the *H* band the brown line indicates a template spectrum of an elliptical galaxy at redshift 1.5: most of the flux is emitted in the infrared while only little flux can be detected in the reddest optical bands.

objects with redshifts larger than ∼1.1 (also illustrated in Fig. 2.3) the *H* filter is the backbone of the survey. The limiting magnitude in *H* is expected to be deep enough because the spectra of elliptical galaxies are flat in the corresponding wavelength regime. Even strongly dust-enshrouded galaxies can be identified more easily when the *H* filter is used.

2.2 Limiting magnitudes

Since the HIROCS survey is focussing on the search for high-redshift clusters of galaxies the calculation of the limiting magnitudes and the determination of exposure times is based on a suitable galaxy template spectrum. The galaxy population in clusters is dominated by elliptical galaxies (see Introduction) which are expected to be centrally concentrated in terms of their spatial distribution even at high redshifts (van Dokkum et al., 2000). Therefore a synthetic spectrum of an elliptical galaxy at redshift 1.5 is chosen from the galaxy template library (see Sect. 4.1.2) of the multi-color classification

to compute the magnitude limits:
To identify a realistic spectrum for an elliptical galaxy a redshift-dependent fit for the rest-frame $(U-V)$ color of the red-sequence galaxies from COMBO-17 is used. For the red galaxies the following estimation was found (Faber et al., 2006):

$$(U-V)_{\rm red} = 1.4 - 0.31{\rm z} - 0.08({\rm M}_V - 5{\rm log}h + 20) \tag{2.1}$$

with the redshift z and the rest-frame V band magnitude M_V. For a redshift of 1.5 and the given cosmological parameters the estimated color is 1.04 and the spectrum in Fig. 2.3 shows a spectrum of an elliptical galaxy which comes closest to this color. From COMBO-17, Bell et al. (2004) measured the absolute rest-frame magnitude in the B band for early-type galaxies in the redshift range $0.2 < \mathrm{z} < 1.1$ (Fig. 2.4). This relation is extrapolated linearly to redshift 1.5 which yields an absolute B band magnitude of -22.0 mag for the determination of the HIROCS limits and the template spectrum has been scaled accordingly. The first column of Table 2.1 shows the resulting five absolute magnitudes of the HIROCS filter set computed by convolving this template spectrum with the filter transmission curves. The advantage of this procedure is that no evolutionary correction term is needed to be applied afterwards because the spectrum already describes a galaxy at redshift 1.5.
With the absolute magnitude at hand the magnitudes in the observed frame can be calculated by, see Hogg (1999) and Hogg et al. (2002):

$$\mathrm{m}^\star = \mathrm{M}^\star + \mathrm{DM} + \mathrm{Kcorr}, \tag{2.2}$$

taking into account the distance modulus DM:

$$\mathrm{DM} = 5\log\left(\mathrm{D_L}/10\right), \tag{2.3}$$

and the luminosity distance $\mathrm{D_L}$ (L: emitted luminosity, S: observed flux):

$$\mathrm{D_L} = \sqrt{\frac{\mathrm{L}}{4\pi \mathrm{S}}} \tag{2.4}$$

Kcorr denotes the so-called K correction, a detailed derivation of formulae is collected in Poggianti (1997). Equation 2.2 is interpreted as the definition for the K correction. It quantifies the part of the relation between the emitted or rest-frame absolute magnitude of a distant galaxy and its observed apparent magnitude when a certain photometric bandpass is considered. The apparent magnitudes are listed in the column $\mathrm{m}^\star$ of Table 2.1.
Usually the distribution of luminosities is described by a Schechter (1976) luminosity function:

$$\Phi\left(\mathrm{L}\right) = \frac{\Phi^\star}{\mathrm{L}^\star}\left(\frac{\mathrm{L}}{\mathrm{L}^\star}\right)^\alpha \mathrm{e}^{-\mathrm{L}/\mathrm{L}^\star} \tag{2.5}$$

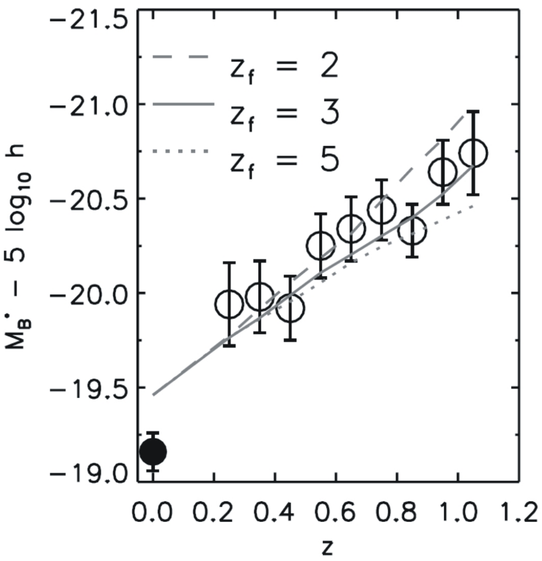

Figure 2.4: (Bell et al., 2004): Evolution of the rest-frame B-band luminosity function of the red-sequence galaxy population from COMBO-17. M_B is the magnitude of the "knee" of the luminosity function. The expectations of a passive evolution model are overlayed as smooth gray lines (with formation redshift shown in the figure legend). The solid point shows the M_B of the SDSS low-redshift comparison sample.

It is characterized by the specific luminosity $L^\star$ where the distribution shows a knee-like change of its slope. α is the slope at the faint end of the distribution and $\Phi^\star$ fixes the overall normalization. The values $M^\star$ and $m^\star$ given in Table 2.1 are the values at the knee of the magnitude distribution. For a better sampling of the luminosity function the survey limits go 1 mag deeper. Furthermore this is important because the bright end shows a steep drop so that only a small number of objects is expected there. The HIROCS limiting magnitudes are listed in column obsLim. The calculations are made assuming detections on the 5σ confidence level.

Having provided the desired depth to which elliptical galaxies at redshift 1.5 should be detected the required exposure times per individual pointing were calculated and are listed in column Δt. These calculations are based on a detailed model taking into account the telescope/instrument response, the atmospheric transmission as well as absorption, and the desired seeing limit of $1.5''$ (courtesy H.-J. Röser). In September 2003 the first OMEGA2000 (see Sect. 3.2) observations confirmed the limiting magnitudes in the *H* band within the uncertainties like seeing and instrument efficiencies. With an exposure

Table 2.1: HIROCS limiting magnitudes and exposure times for the filters B, R, i, z, and H. The left column lists the absolute rest-frame magnitude for an elliptical galaxy at redshift 1.5, the next shows the corresponding K correction term. The column $\mathrm{m}^{\star}$ indicates the apparent magnitude after applying the distance modulus for redshift 1.5. Up to this point the magnitudes are denoting the characteristic magnitude $\mathrm{M}^{\star}$ of a Schechter (1976) luminosity function. At redshift 1.5 it is necessary to sample the luminosity function more deeply. Therefore the survey limits are 1 mag deeper (column obsLim). Considering an individual pointing the exposure time shown in the column Δt is needed to reach the magnitude limits at the confidence level given in the column S/N. This results in the integration times denoted in column Δt/□° to cover 1 square degree.

	M*	K-corr	m*	obsLim	Δt	S/N	Δt / □ °
B	-22.00	1.06	24.2	25.2	3.0	12.2	12 ksec
R	-23.09	1.73	23.8	24.8	3.0	12.3	12 ksec
i	-23.45	1.42	23.1	24.1	3.0	6.8	12 ksec
z	-23.79	1.10	22.4	23.4	9.9	5.1	40 ksec
H	-25.02	-0.26	19.9	20.9	3.0	5.1	48 ksec

time of 3 ksec the 5σ limit was measured to be 21.2 mag. During the reductions of the optical bands the observing limits were confirmed with one exception. Concerning the B band it was found that the exposure times have to be considerably longer to yield the foreseen limiting magnitude. Table 2.1 lists 3 ksec for the B band but now 10 ksec exposures are made for the survey. The reason may have been a wrong estimation of the K correction. The signal-to-noise (S/N) ratio from this calculation appears in the corresponding column. The necessary overall exposure time to cover 1 square degree has to take into account the different detector setups (column Δt/□°). In total to cover a field size of 1 square degree 5.2 clear nights are needed. The whole survey with 11 square degrees takes $11 \times 5.2 = 57$ clear nights.

Chapter 3

HIROCS – Observations and data

The goal of HIROCS is the setup of a significant galaxy cluster sample at high redshifts. In the previous Chapter, the necessary framework comprising the area, filter set, and the limiting magnitudes for the observations was introduced. With these basics the practical observational issues are explained in the following. After the description of the field selection criteria, the instrumentation is presented. Furthermore, the data reduction for the data obtained with the different instruments, the photometry, and the photometric calibrations are explained in this Chapter.

3.1 Field selection

The HIROCS observations are done on four disjunct fields at different locations in right ascension (RA) to enable observations in all seasons. Two of the fields are built up on fields from the CADIS (see http://www.mpia-hd.mpg.de/GALAXIES/CADIS/) and MUNICS (Drory et al., 2001) surveys. The CADIS and the MUNICS fields cover smaller areas than HIROCS on the sky with $\sim 13' \times 13'$ and $28' \times 13'$ (in the 03h field, MUNICS-S2F1), respectively, and thus comprise only small parts of the HIROCS fields (consider the field layout in Appendix A). For these fields large data sets comprising deep imaging and even more importantly long-slit spectra are accessible. Based on these data, tests of the multi-color classification and the cluster search technique can be carried out. The third field is centered on the COSMOS field. COSMOS is a multi-wavelength survey covering two square degrees in multiple bands from radio to X-rays including high-resolution Hubble space telescope (HST) imaging. This publicly available data set was chosen because it will substitute largely the HIROCS data set. As part of the thesis work two new fields were selected under consideration of the criteria which will be explained in this section.

Table 3.1: Names and coordinates of the HIROCS fields. Also shown are the corresponding galactic latitude b, field sizes as well as the galactic extinction E(B−V) in mag.

Field name	RA (J2000)	DEC (J2000)	b	Size	E(B-V)
MUNICS-S2F1	$03^h06^m12^s.0$	-00° 20' 35"	-48°.2	3° x 1°	0.080 mag
COSMOS-10h	$10^h00^m28^s.6$	02° 12' 21"	42°.1	2° x 1°	0.018 mag
CADIS-16h	$16^h24^m32^s.0$	55° 44' 32"	42°.1	3° x 1°	0.006 mag
HIROCS-22h	$21^h59^m58^s.7$	02° 23' 14"	-39°.2	3° x 1°	0.065 mag

While one of these was omitted in favor of the COSMOS field at the same RA, the fourth field is the newly selected HIROCS 22h field. Table 3.1 lists the HIROCS fields with their coordinates [RA, DEC], galactic latitude, field sizes, and the average galactic extinction E(B−V) in mag.

3.1.1 Selection criteria

Large-scale structure (see Introduction) imposes a need for large field sizes. Both the typical dimensions of the voids covering 25 Mpc and clusters of galaxies with only a few Mpc appear smaller as a function of redshift up to redshifts of about 0.9 (see Fig. 4.7). At even higher redshifts the apparent extension increases again. The apparent angular extent of an object on the sky is:

$$\mathrm{d_{ang}} = \frac{(1+\mathrm{z})^2 \mathrm{d_{phy}}}{\mathrm{D_L}} \tag{3.1}$$

with the true physical size $\mathrm{d_{phy}}$ and the luminosity distance $\mathrm{D_L}$ (equation 2.4). According to this equation clusters with a true physical extension of 2 Mpc appear with approximately $\mathrm{d_{ang}} = 5.5'$ on the sky at redshift 0.5 and with $4'$ at redshift 1.5. A void with 25 Mpc at the survey redshift limit of 1.5 shows up with $60'$. Therefore the field sizes of $1^\circ \times 3^\circ$ are chosen to be able to cover these dimensions. With four disjunct fields the risk that the cluster finding suffers from a pointing by chance into a largely empty or overdense sky region is reduced.

The selected fields should not contain bright stars which would saturate very fast in the long science exposures and the strong blooming (transfer of charge to neighboring pixel rows or columns) would leave a large part of the exposures unusable. Moreover increased reflections in the camera optics would deteriorate the images because of stray light. For the large area fields of HIROCS which are of the order of a few square degrees it is not easy to find fields with a low number of bright stars. The brightest stars in the fields as a practical limit have approximately 9 mag. Consider Fig. A.4 which shows the 22h field. Bright stars are found close to the field borders which have not allowed a different field position. This is also the reason why the 1 square degree patches are not aligned in declination.

The goal of the survey is to observe faint extra-galactic objects. For the flux measurement and for the exact evaluation of colors the elimination of foreground reddening is vital. High foreground extinction would also not allow to reach the desired limiting magnitudes. Therefore fields with low galactic foreground extinction have to be selected. The Galaxy contains large amounts of gas and dust which is mainly located in the galactic disk. In general it is convenient to observe at high galactic latitudes ($b > 30°$) because of low star density. The galactic latitude b of the HIROCS fields is listed in Table 3.1. A map of the galactic extinction has been provided by Schlegel, Finkbeiner & Davis (1998). This study provides a $100\,\mu$m all-sky map of the dust emission combining data from the DIRBE instrument onboard the *COBE* satellite and from the IR satellite *IRAS*.

Once suitable fields have been identified obeying the above mentioned criteria their extinction is estimated by inspection of the dust maps at the fields' positions and their surroundings. Looking at the DIRBE maps low extinction values are not only found at high galactic latitudes but also in hole-like structures at low latitudes. Fig. 3.1 shows the HIROCS 22h field and its surroundings in the dust map where the 1°×3° field edges are marked with white lines. At three positions the extinction value has been measured and it is found to be in the range $E(B-V) = 0.04 \ldots 0.07$ mag. The average extinction across the other survey fields is shown in Table 3.1 in the rightmost column.

Another requirement was that the new field(s) should be equatorial to enable follow-up observations from both hemispheres. Observation proposals are planned at the ESO Very Large Telescope (VLT) and at the Large Binocular Telescope (LBT) once it is accessible for the science community.

3.2 Instrumentation

The instrumentation with wide-field capabilities at the Calar Alto 3.5m telescope has been supplemented in the year 2003 in the near-infrared by the OMEGA2000 instrument (Fig. 3.2, left). It was at that time the first camera in the world equipped with a Rockwell HAWAII2 detector at a 4m class telescope. OMEGA2000 is used as the most vital building block for the survey because imaging in the infrared enables rest-frame optical studies of galaxies at higher redshifts. Additionally the large field of view of this instrument is unique in the infrared covering $15.4' \times 15.4'$ which permits the conduction of a large-area extragalactic survey like HIROCS. In the optical the observations are done with LAICA

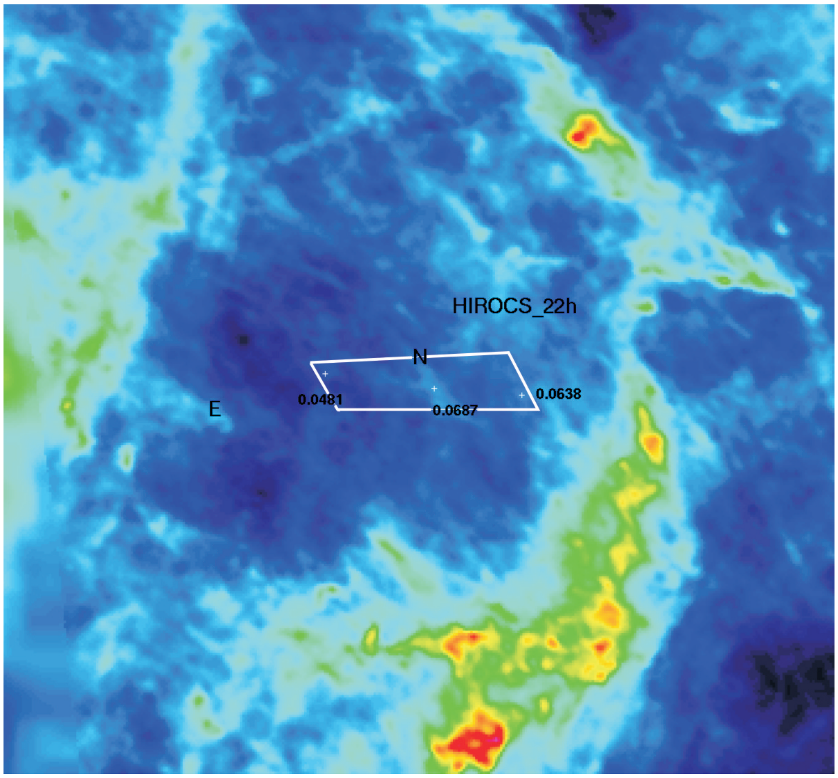

Figure 3.1: The DIRBE/*IRAS* dust map in the region of the newly selected 22h field (white quadrangle). The extinction E(B−V) is color-coded – blue indicates low extinction whereas red means high values. Within the field borders the extinction values range from approximately 0.04 to 0.07 mag in the maximum. The fields appear twisted due to the projection of the map.

(Fig. 3.2, right) which is the Large Area Imager for Calar Alto. The detector setup is shown in Fig. 3.3. The gaps between the CCDs are sized in a way to enable the contiguous coverage of 1 square degree with four individual pointings. The layout of LAICA guided the design of the HIROCS fields comprising of independent 1 square degree patches of which always three/two overlap. This leads to a total size for each of the four fields of $1^\circ\times3^\circ$ and $1^\circ\times2^\circ$.

Due to the availability of guaranteed time of the MPIA the optical observations in the two bluest bands B and R are supplemented by data taken with the Wide-Field Imager (WFI) at the ESO MPG 2.2m. For these two filters WFI and LAICA data cannot be mixed on the same survey patch due to the different detector geometry. The WFI has a field of view of $34'\times33'$ and consists of eight CCDs with 2048×4096 pixels. The arrangement of the

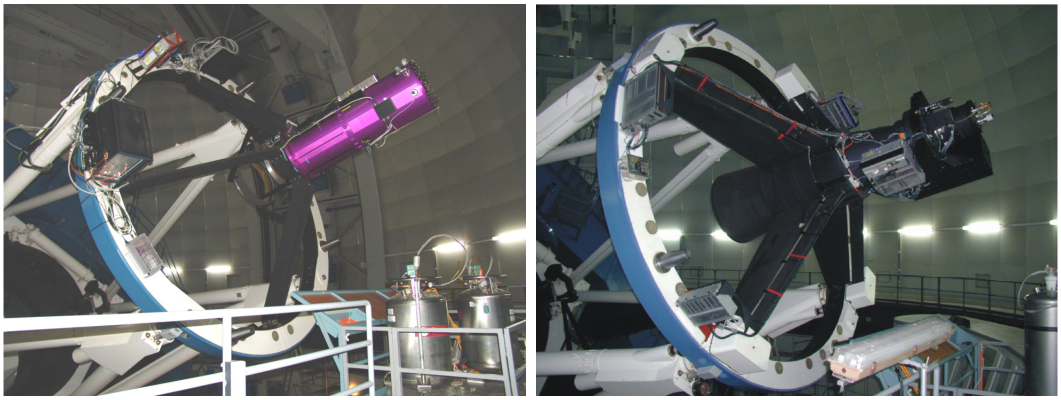

Figure 3.2: Left: OMEGA2000 mounted on the prime focus of the Calar Alto 3.5m telescope. The telescope has been moved to the service position. Right: LAICA also on the prime focus.

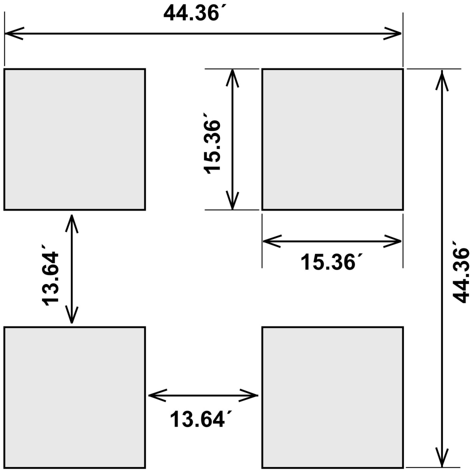

Figure 3.3: The four detectors of LAICA are arranged with gaps just as large as one CCD size minus an overlap of approximately $100''$. The sizes and spacings are indicated in arc minutes. A field size of 1 square degree can be covered contiguously with four pointings off-set by $14.3'$.

detectors in a 4 × 2 array is shown in Fig. 3.4. With the WFI 1 square degree patches are achieved by four independent but overlapping pointings. For filling up the gaps between the CCDs a dithered series of exposures has to be taken.
Dithering is a technique where several images for a certain field (also called pointing) with

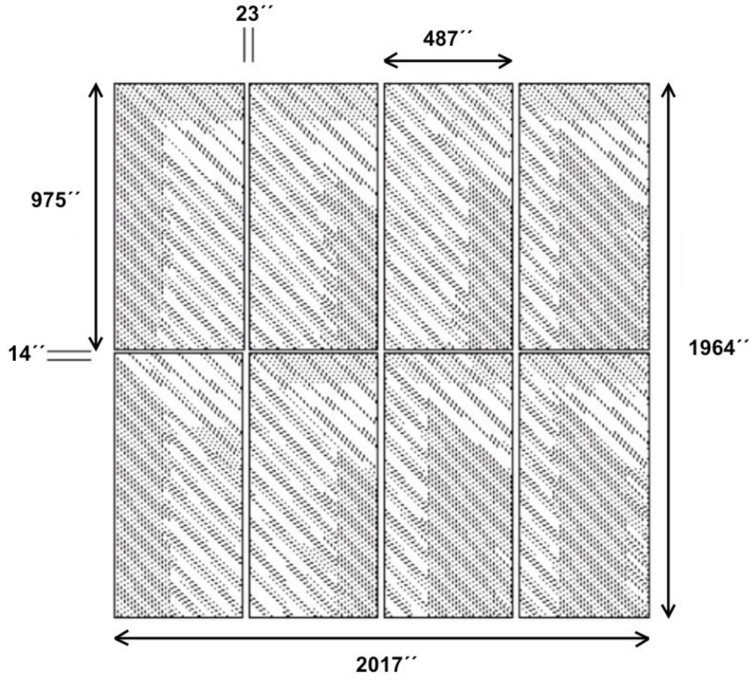

Figure 3.4: Wide-Field Imager (WFI) layout: The eight detectors are arranged with small gaps of 23′′ and 14′′ in a 4×2 array. To cover the gaps of this setup a series of dithered exposures has to be co-added. The sizes and spacings are indicated in arc seconds. A field size of 1 square degree can be covered with four pointings.

fixed offsets that follow a pre-defined pattern are collected. Two purposes can be fulfilled with that: on the one hand gaps between detectors can be filled up with data. The offset exposures on the other hand are used to remove detector defects, objects (for flatfield generation), and cosmic ray events from the exposures within a median routine. This is possible because the positions of such signals on the CCD vary within the dither series. The dithering technique is therefore applied for all cameras. Only for extremely extended objects which do not occur in the HIROCS fields dither offsets are sometimes too small. Dithering leads to a loss of area for the science analysis because the overlap common for all positions is smaller than for a single deep exposure. Splitting the long survey exposures into a series allows additionally the measurement of rather bright objects. Many of these would saturate on ultra-deep exposures. In the end the single exposures can be co-added to yield a deep sum frame.

3.3 Data reduction

The HIROCS survey observations are done with three cameras each having a different detector setup and even a different detector technology in the infrared. Thereby the optical and near infrared observations in the five non-standard filters have to be accurately calibrated to be able to perform a multi-color classification of the objects. To achieve this and to handle data taken under non-photometric conditions synthetic photometry with the help of standard stars in the fields is carried out. Moreover the large fields to be observed are split into many sub-fields which leads to the creation of mosaic images. This is a complication compared to CADIS and COMBO-17 which are based on single fields where the field-of-view of the instrument used (e.g. WFI) determined the field size. All these issues bring up the need for changes and new developments in the existing software packages which are based on the MIDAS image processing programs. At the MPIA several context environments like WFI, MPIAPHOT, or CADIS have been developed which provide customized routines to handle photometric data from different projects/instruments. The data reduction strategy for the first 1 square degree data set (for the project status see Sect. 3.10) in all survey filters was to split the tasks between three people. Hans Hippelein took care of the LAICA data comprising observations in the i and z bands. He had to create new techniques due to the presence of special problems (see details in 3.3.2). The infrared data were reduced by Hermann-Josef Röser using the OMEGA2000 data reduction pipeline which was developed by René Faßbender in his Diploma thesis (Faßbender, 2003). Problems about the infrared data are discussed in Sect. 3.3.3. The B and R band data were gathered with the Wide Field Imager (WFI) and these data were reduced by the author. A more detailed description of the procedures are presented in Sect. 3.3.1.

3.3.1 WFI

On the COMBO-17 web page a detailed WFI data reduction cookbook[1] explains all the reduction steps for dithered survey images. Based on the above mentioned context environments with specially tailored routines the basic reduction sequence was carried out until the creation of deep stacked frames (part I of the pipeline). The bias-, flatfield- and fringe pattern corrected images are subsequently joined with the reduced frames from the other instruments (see the following sections). Here a short summary of the necessary steps shall be given.

The reduction pipeline is semi-automatic which means that after certain steps the user

---

[1] http://www.mpia.de/COMBO/combo_cookbook.html

has to provide input parameter specifications as well as file lists in the form of MIDAS catalogues. It is also possible to combine all or a subset of reduction steps (guided by commands) into a larger procedure. After the read-in, the creation of an input catalogue, and the debiasing, the eight single files of the chips are combined ("mosaiced") in a single frame. Thereby chip rotations are respected and hot pixels as well as bad columns are masked out.

The most vital and time-consuming step is the creation of a flatfield frame which serves to correct for the pixel-to-pixel variations of the detector(s) and for global sensitivity patterns caused by detector non-uniformity and vignetting induced by the instrument optics. In the optical so-called sky flatfield exposures during twilight are the best option because these provide the best possible illumination of the CCDs. Ideally each pixel should be exposed to the same illumination level. The command FLAT/WFI is used to create an average flatfield frame where a minimum of three and in the optimal case five sky flats are needed to remove outlier pixel values with a median procedure. It is essential that the flatfield exposures have consistent global intensity patterns to really yield the correct pixel-to-pixel variation as well as global intensity pattern. To find a suitable set of such exposures, either two candidate frames can be divided and checked for flatness. If the resulting frame is not flat and still shows structure these cannot be used together. Unfortunately, it was rather hard to find a suitable set of sky flatfield images. From service mode observations only sets of three flatfield exposures per observing night are delivered by ESO. Moreover flatfield sets from different nights often cannot be combined because these show varying illumination patterns. This meant that for a certain observing run all possible combinations of such exposures had to be checked to yield a suitable correct flatfield. In the simplest case the science exposures are subsequently corrected with the average flatfield frame (command CORRECT/WFI).

A severe problem about the reduction of WFI data is posed by the contribution of scattered light within the camera which has to be taken into account. The instrument optics redistributes light from e.g. bright stars in or close to the observed field in an additive manner in contrast to the multiplicative flatfield terms. Effectively this leads to an increased background level in the center of the pointings and a decrease towards the edges. The photometry is thus systematically wrong across the observed fields. Klaus Meisenheimer (priv. communication) has determined this contribution and fitted a 2D polynomial of 3rd order to the deviations which is applied within the data reduction process.

The correction scheme works as follows: first the average sky flatfield frame is multiplied by the 2D polynomial frame. Then the science frames are corrected with this modified flatfield using CORRECT/WFI. After this multiplicative correction the straylight term is left in the exposures which is evident as a bell-like shape of the background intensity distribution. This global additive term is modelled by means of the median procedure implemented in FLAT/WFI. But here the science exposures are the input for the flatfield routine. Science exposures with long integration times on the same field are full of objects and some are so bright that large areas on the exposures are affected by straylight haloes. If large areas are affected the dither offsets are too small to be able to remove these haloes with FLAT/WFI. Therefore ideally as many as possible different pointings which are treated with the same modified flatfield have to be put into the procedure. The result contains a radially symmetric structure which is modelled with the command RINGEX/WFI which performs a fit with a smoothed function. Having produced the model for the additive straylight contribution the science exposures are corrected by CORRECT/ADD.

In the same step possible fringe patterns which are additive terms can also be corrected for. Fringes are interference patterns in the thin detector layers which are induced by light which penetrates into the detector and is reflected at the backside. Travelling in the opposite direction it interferes with the incident light. Multiple reflections are possible. The amplitude of the fringes is dependent on wavelength since light with lower frequency is able to penetrate deeper into the detector material (silicon for CCDs) and also the thickness of the material. Thus fringe patterns are most pronounced in the z band. Remanent fringes after applying CORRECT/ADD have to be corrected separately by using the science frames after the straylight correction and feeding these into FLAT/WFI. Finally after a second CORRECT/ADD application the flatfield corrected science exposures are ready for the next steps like stacking, removal of cosmic ray events, object finding, and photometry. The former two procedures are carried out with the command STACK/MOSAIC of the pipeline while the latter two were not performed by the author. These steps will be explained in Sect. 3.4.

3.3.2 LAICA

Hans Hippelein developed in the course of the last 1.5 years new software to deal with LAICA specific problems. One of these problems are strong distortions which exceed $20''$ in the field corners. The standard procedures available at MPIA are not designed to deal with such extreme distortions. Guided by the recipe of the drizzle procedure (Fruchter & Hook, 2002) the new algorithm carries out a rebinning of the single images in a dither series onto a common celestial coordinate grid. These drizzled images are stacked to a sum image using a median routine. Cosmic ray events are located in the drizzled sum images. After that the cosmics can be removed from the undrizzled frames. The fringe behaviour of the LAICA detectors poses the second complication. In the i and z band the superposition of atmospheric emission lines of different molecules with varying strength are responsible for the appearance of the fringe pattern and its temporal variations. To overcome this problem the fringe correction is done in an iterative process.

3.3.3 OMEGA2000

Observing in the near-infrared – OMEGA2000 is designed for observations between 1 and 2.5 μm – is governed by a high sky background due to the blackbody radiation of the atmosphere and the thermal background of the telescope surroundings. Additionally the infrared-detector technology is different compared to the optical regime. To circumvent these issues short exposure times are applied. As a consequence a much higher number of exposures is collected compared to the optical observations. More details can be found in the manual for the instrument[2].

Currently René Faßbender's OMEGA2000 pipeline is refined to allow a sky subtraction with an improved signal-to-noise ratio in the background. To achieve this a 2-pass strategy comes into play where in the second pass all objects are omitted. The infrared observations with OMEGA2000 are complicated by the problem of determining a suitable flatfield. Unfortunately, the sky background derived from either twilight flatfield exposures or the night sky is variable on short time scales so that the background shape is changing within series of such exposures. Moreover dome flatfields are useless, too, because the optics of OMEGA2000 image the structure of the primary mirror which leaves sharp edges on these exposures. The treatment of these problems is solved in the meantime.

3.4 Object finding and photometry

The determination of statistically correct multi-color classification results relies mainly on accurate error estimations for each measured flux value. Color indices together with their errors which are calculated from the flux measurements form the basis for the classification procedure (see Sect. 4.1). For this the exact relative calibration between the filters is vital whereas the absolute photometric calibration is not needed for the classification.

In CADIS and COMBO-17 the following procedure was applied: Each single exposure is used to measure the object fluxes so that a series of measurements yields the possibility to calculate the flux errors from the variance of the resulting values. Following Röser & Meisenheimer (1991) the objects are integrated over an aperture weighted by a Gaussian distribution. This optimizes the signal-to-noise ratio in the measurement procedure. Since the exposures are split into a series of sub-exposures which are often observed under varying seeing conditions the different seeing values have to be taken into account when

---

[2] http://w3.caha.es/CAHA/Instruments/O2000/OMEGA2000_manual.pdf

the photon count rates are determined. Additionally, the same apertures around the single objects on the different exposures have to be taken for the count rate determination.
Due to the creation of mosaics for HIROCS changes have been necessary which come into play after the data reduction procedure comprising bias, flatfield, background distortion, and cosmic correction (see Sect. 3.3). First of all deep sum images for the individual pointings and filters are produced from the dithered single exposures for which also the orientation and shifts have been determined in advance. The object detection is performed automatically with the SExtractor software (Bertin & Arnouts, 1996) which is called from within the context MPIAPHOT on the sum images for each filter independently. All objects with a minimum number of connected pixels are identified on a smoothed image. For the smoothing the seeing PSF[3] derived from the reduced images is used. From the SExtractor results – the positions, shapes, extensions, and signal-to-noise ratios of the objects – a weight image is derived. This weight image serves to respect the possibly varying signal-to-noise ratio and photometric quality of the pointings for the creation of the mosaic images of WFI, LAICA, and OMEGA2000. SExctractor has to be tuned to reject spurious objects which are found in the vicinity of very bright stars. Artefacts are also found close to diffraction spikes and satellite trails which have to be identified and removed from the SExtractor object lists. The so-called "master list" is a joint object list which is produced by combining the object lists from the sum images of the different filters. This is done on an artificial noise-free image which combines the detections in the different filters according to the signal-to-noise ratios of the objects. The SExtractor results provide the objects' shapes. In the end the master list results from an object search on this artificial image and the object coordinates represent the sky positions.
For the photometry which is performed on the original images the coordinates have to be transformed to the system of the individual frames and the distortions of the different instruments used have to be respected thereby. The images are often gathered under different seeing conditions. To circumvent the occurrence of spurious colors when these images are combined the photometric analysis of all frames is performed with a common effective PSF using a different Gaussian weighting function such that (s: e-folding widths):

$$s_{\text{eff}}^2 = s_{\text{seeing}}^2 + s_{\text{weight}}^2 = const \tag{3.2}$$

Consequently broad weighting functions are applied for frames with good seeing and the contrary is true for worse seeing. The survey seeing limit is 1.5″. By examining the histogram of the count rates locally around each object the background is determined. After that the photometric calibration is carried out which is introduced in the next section.

---

[3] = point spread function

3.5 Photometric calibration

Observational astronomy relies on the availability of reference sources for the calibration of brightness measurements. Standard stars are used for a relative measurement of the brightness of the objects the astronomer is interested in. Historically Vega has been selected as the primary reference star. A suite of secondary standards, see e.g. Oke (1990) and Hamuy et al. (1992), has been set up for which the absolute spectral energy distributions[4] have been determined. These spectra are calibrated from the UV to the near infrared spectral range.

At the beginning of this section the strategy for the flux calibration comprising three mayor steps is introduced. After that the selection of suitable standard stars, an outline of the reduction steps, and finally first results are described.

3.5.1 Basic strategy

The photometric measurements for HIROCS are performed with three different cameras, with a non-standard filter set, and often under non-photometric conditions. The three steps of the calibration procedure for the synthetic photometry are:

- Relative calibration of the flux levels on the single exposures for each filter,
- Relative calibration between the survey filters with the help of standard star spectra,
- Absolute calibration to the flux outside the atmosphere using SDSS (York et al., 2000) and 2MASS (Skrutskie et al., 2006).

The first step is performed by common stars which should not be saturated but show a good signal on the exposures. To transfer this flux normalization to neighboring pointings of the mosaics short offset exposures centered on the chip edges are utilized. If the long exposures do not yield enough well-measured stars the acquisition images (exposure time $10 - 50\,\mathrm{s}$) can be used to carry out the relative calibration. Note that this step ensures that the relative flux level of the exposures for a single filter is adjusted. This means that 500 counts on one detector correspond to 500 counts on the other. The exact treatment of the mosaic frames is currently under development. For the second and third step tertiary standard stars in the survey fields are observed. The resulting spectral energy distributions (SED) of the stars can be convolved with filter transmission functions to yield synthetic photometry which serves for the calibration. On each square degree survey patch eight tertiary standard stars have been selected in the field corners

---

[4] see also the compilation at http://www.eso.org/observing/standards/spectra/

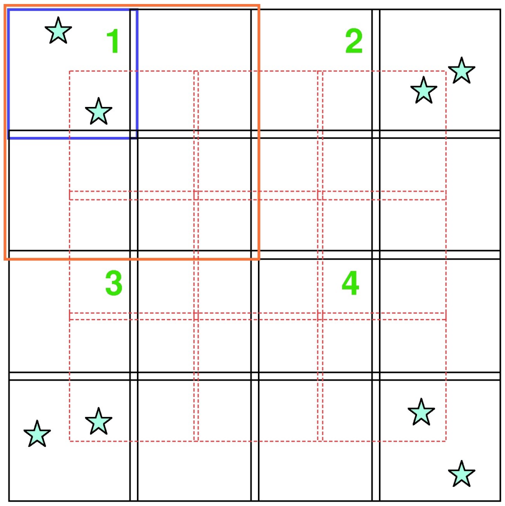

Figure 3.5: Survey exposure setup to cover 1 square degree – LAICA: black pattern, CCDs marked by green numbers, 4 pointings to cover 1 square degree), OMEGA2000 (detector size marked by blue square, 16 pointings) and WFI (field of view marked by red square, 4 pointings).

(indicated by light blue stars in Fig. 3.5). This ensures the relative calibration of the data taken with WFI and LAICA because for each pointing two standard stars can be measured. OMEGA2000 exposures with no standard star coverage are calibrated by short exposures off-set such that the calibration can be transferred to the neighboring pointings (red dotted squares in Fig. 3.5). With the Calar Alto Faint Object Spectrograph (CAFOS) at the 2.2m telescope the spectra are collected in the optical/near infrared wavelength range ($\lambda \sim 3500 - 9000\,\text{Å}$). Two grisms (blue-200 and green-200) are deployed to cover the desired wavelengths. Matching the observed spectra in this wavelength range to the Pickles empirical spectral library (Pickles, 1998) provides spectra for the calibration purpose. Besides enabling survey observations under varying observing conditions the availability of flux-calibrated SEDs offers greatest possible flexibility e.g. in the case when follow-up observations in the survey fields using new filters are scheduled. Details of the reductions and calibration are shown later on in this Chapter.

After having provided homogeneous flux levels for each filter separately (first step) the relative calibration between the filters forms the second step of the calibration procedure. For this the spectral shape of the tertiary standard stars is exploited by using their

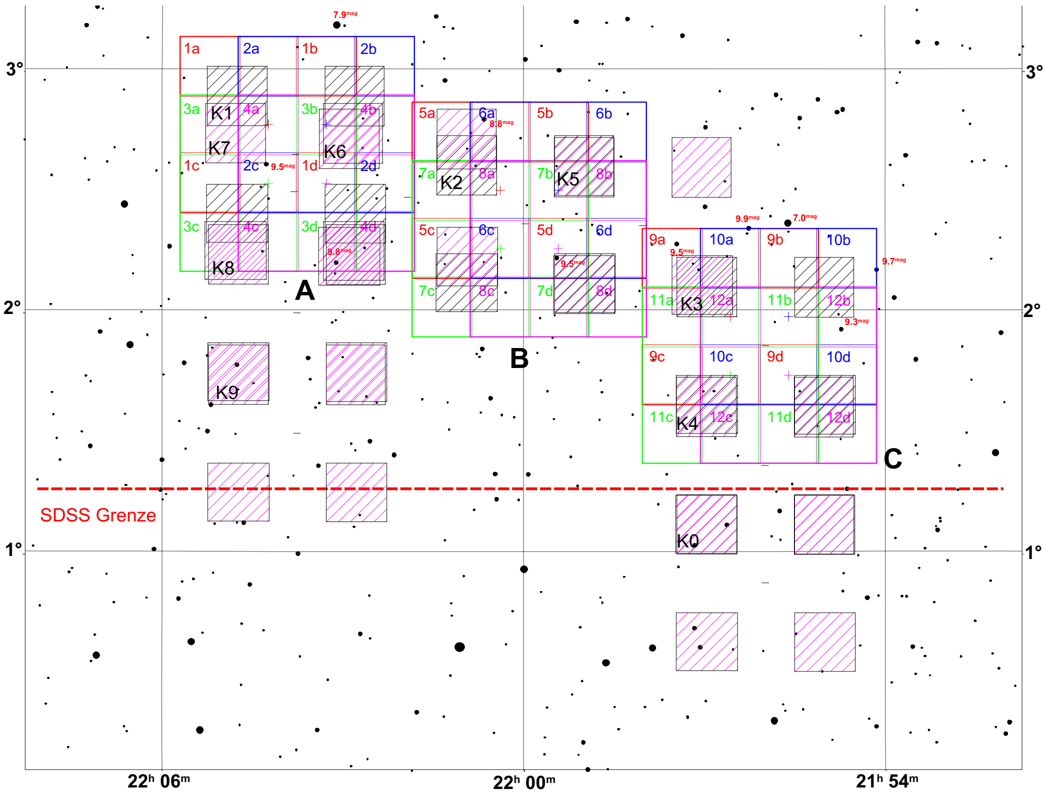

Figure 3.6: HIROCS 22h field with the sequence of LAICA calibration exposures (magenta hashed squares). The upper border of the SDSS coverage is shown as horizontal red dashed line.

synthetic photometry in the HIROCS filters. In the case any discrepancies between the measured and the synthetic instrumental magnitudes exist scaling factors are calculated and applied to the measured photometry.

As the third and last step of the reduction procedure the intensities have to be transformed to the flux outside the Earth's atmosphere. This is done by the absolute flux calibration of the tertiary stars' spectra with the help of SDSS/2MASS ensuring to be independent of the varying observing conditions. The former is not possible for all fields because these are not covered by SDSS.

The new 22h field is close to a SDSS stripe (distance of approximately 13′). The calibration can be achieved by offset exposures with LAICA (see Fig. 3.6). To do so one pointing with all four detectors has to be done on the SDSS stripe (the lower right pointing in the Figure). The offset exposures were carried out following the depicted scheme to transfer the calibration to the other sub-fields A, B, and C. For security this scheme ends again in the area covered by the SDSS (to the south of field A). These calibration exposures have been secured already in October 2005 but have to be reduced and analyzed.

3.5.2 Selection of stars

Originally the selection of the standard stars has been done by eye-ball for the CAFOS observations. For this purpose images have been downloaded from the STScI Digitized Sky Survey[5] (= DSS). This archive offers an internet tool to retrieve digitized images from several reference sky surveys. The images to search for the stars are taken from the POSSII/UKSTU which offer data for blue, red as well as infrared wave bands. By visual inspection suitable stars with visual magnitudes of approximately $14-16$ mag have been selected. Stars brighter than 14 mag have been omitted because these could eventually be saturated even on the short survey acquisition images. These are used not only to check the accurate pointing but also to measure the filter flux of the standard stars in the case that these are saturated on the long survey exposures. This secures the calibration of the single survey images. The exposure time for the acquisition images is usually $10-50$ s. For stars fainter than 17 mag the exposure times for the CAFOS spectroscopy would exceed 2 000 s and therefore be uncomfortably long.

After having reduced and inspected the first spectra problems became obvious: Stars of spectral type later than K0V show broad molecular absorption features in their spectra. The continuum of the spectra is hardly defined and the spectral fitting to the Pickles library is uncertain. Moreover a large uncertainty arises during the convolution process when an absorption band happens to lie at the steep border of a filter transmission function.

In the fields with SDSS coverage stars of a desired spectral type can be chosen using color criteria (Finlator et al., 2000). Stars with late-type spectra were replaced and new candidates with spectral type earlier than G5V selected. The $(g-r)$-$(r-i)$ diagram for the standard stars in the HIROCS 03h field is shown in Fig. 3.7. The objects left of the red line have spectral types earlier than G5V and are kept for the photometric calibration.

On two of the HIROCS fields no SDSS data are available and another procedure has to be applied. The first idea was to take advantage of the USNO-B astrometric and photometric catalogue (Monet et al., 2003) which is based on 7 435 Schmidt plates from various photographic surveys conducted over the past 50 years. Due to their photographic origin the accuracy of the filter exposures is on the order of 0.3 mag. This rather high uncertainty leads to a large spread in color-color diagrams so that in contrast to the

---

[5] see http://archive.stsci.edu/cgi-bin/dss_form

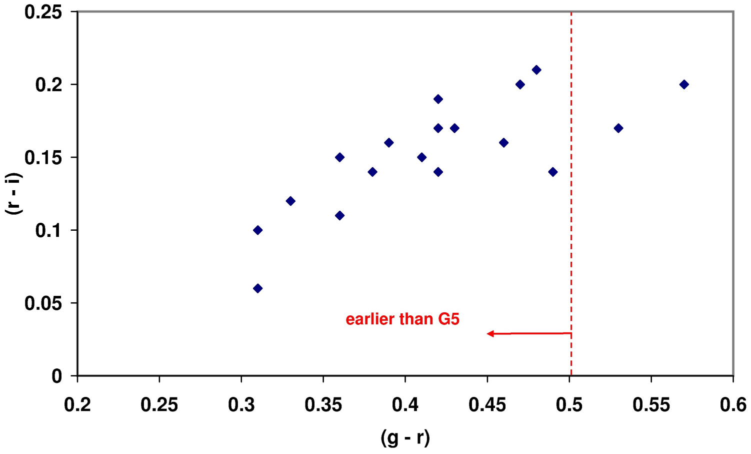

Figure 3.7: Color criteria from the SDSS along the lines described in Finlator et al. (2000) applied to standard stars in the HIROCS 03h field. The vertical dashed line is the division between spectral types earlier and later than G5V.

accurate SDSS data no reliable selection by spectral type can be carried out. Thus if stars have to be replaced POSSII images are used like this: blinking blue and red/infrared images gives a hint whether the spectrum is more late- or early type. Early-type spectra have more flux in the blue band while being weaker in the red/infrared. The opposite is true for late-type spectra. Spectra of K stars have a strong increase in their infrared energy distribution and can thus be separated rather effectively. Several stars in the 16h and 22h fields have been replaced this way.

3.5.3 Reduction procedure

The reduction of the standard star long-slit spectra is done using standard procedures of the MIDAS software with its context LONG. After the usual reduction steps like bias subtraction, flatfield correction, and wavelength calibration (determined by computing the dispersion solution for the grisms, resolution ~5Å per pixel) the spectrum is extracted according to Horne (1986): perpendicular to the dispersion direction a polynomial fit of degree 4 serves to model the sky background which is subsequently subtracted. The remaining object spectrum can be then integrated along the spatial direction to yield a 1D spectrum. The extracted spectrum is a convolution of the intrinsic spectral shape of the object and the response curve of the observing system. Due to the influence of the

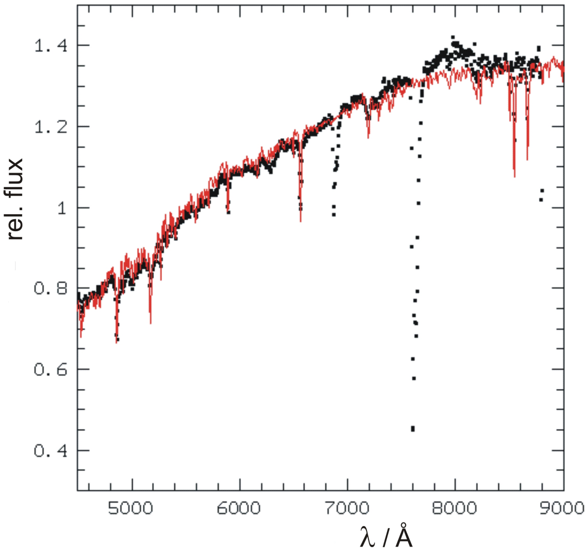

Figure 3.8: Illustration of the best match between the observed spectrum of a tertiary standard star (small black squares) and the Pickles library spectrum (red line).

atmosphere an extinction correction is applied which is proportional to the airmass. Here a typical extinction curve for Calar Alto is used.

The absolute flux calibration is achieved by two major steps: first the match of the spectra to the Pickles (1998) library gives the spectral type of the stars as well as the best-matching spectrum which is scaled in the second step to match the flux measurements from SDSS and 2MASS. For the first step the response curve which represents the overall quantum efficiency of the telescope system including the instrument serves for the calibration of the spectrum. The response curve is determined from the secondary standard stars by dividing the measured and the already calibrated spectrum which is available as a MIDAS table. In this context it is not necessary to observe the stars under photometric conditions because the spectral matching should only yield the spectral type. As stated before the final absolute flux calibration is done with SDSS/2MASS. The two spectra from the blue and green grisms are connected after the response correction where these are weighted with the local quantum efficiency in the overlap region. The calibration procedure is accurate in the wavelength range $\lambda \sim 4\,500 - 7\,500$ Å. Redwards of this range the signal-to-noise ratio of the green spectrum is low because there the transmission of the grism decreases and furthermore several atmospheric absorption bands due to water vapor dominate the spectra. Therefore only the above mentioned wavelength region is used for the spectral matching to the Pickles library.

The spectral matching which is done by eye is performed by plotting the measured spectrum and over-plotting the Pickles library spectrum which best follows the continuum and the intrinsic stellar absorption features (see Fig. 3.8). This best-matching spectrum is then convolved with the filter transmission curves of the SDSS (u, g, r, i, z) and the 2MASS (J, H, K_s) filter set to yield the expected filter magnitudes measured in these surveys. A comparison of these expected magnitudes with the measured ones provides the contribution of the atmospheric extinction to the observation. In the case that the spectral shape does not fit very well to that observed in SDSS/2MASS the matching procedure with the Pickles library is iterated. In the end the best-matching Pickles template is available for the absolute flux calibration of the HIROCS survey filter data.

3.5.4 Results

The reduction and calibration of the spectra is ongoing. 84 of a total of 88 calibration stars in all fields have been observed. Some of them have to be replaced because the spectral type complicates the flux calibration (see Sect. 3.5.2). A large part of the spectra is finished to the stage of wavelength calibration. For the HIROCS 03h field 7 stars are flux calibrated and the best-matching Pickles spectrum can be used for the calibration of the photometric imaging. Fig. 3.9 shows the result for standard star #1 in the 03h field. This star is of spectral type G2V. The detailed results from the spectral matching are shown in Appendix B.

The analysis of the first sample of standard stars shows that the relative accuracy of the fitting is $\delta\mathrm{m} < 0.04\,\mathrm{mag}$ in the optical and $\delta\mathrm{m} < 0.08\,\mathrm{mag}$ in the H band. While the accuracy in the optical bands is satisfactory in the infrared the results are less secure. This stems from the fact that the spectral matching is done in the optical. Remember that the CAFOS wavelength coverage is $\lambda \sim 3\,500 - 9\,000\,\text{Å}$. The spectral leverage from the matching region to the infrared bands (J: 12 600 Å, H: 16 500 Å, K: 21 600 Å) is rather high and leads to higher uncertainties for these filters. Considering this the relative uncertainty of $\delta\mathrm{m} < 0.08\,\mathrm{mag}$ is acceptable.

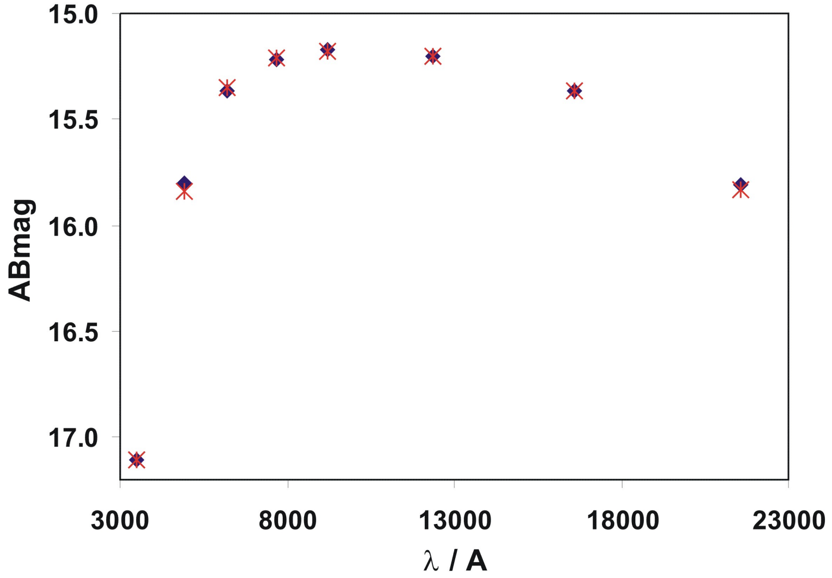

Figure 3.9: AB magnitudes for standard star # 1 in the HIROCS 03h field: the dark blue diamonds represent the brightness of the best-fitting Pickles spectrum obtained by convolution with the five SDSS filters and the three 2MASS filters. Red stars indicate the values measured by the reference surveys.

3.6 Current project status

At this point the status of the HIROCS project in March 2006 shall be described. The main goal of the PhD project is the development of the cluster search technique and of the techniques for the determination of the selection function. Whereas the basic techniques (see Chapter 4) have been established the data collection mainly in the optical (LAICA) was seriously affected by bad weather and instrument as well as telescope problems (see Table 3.2 with observing runs in which the author was involved). The first good LAICA observing run was in October 2005 by Michael Zatloukal (PhD student since September 2005). Additionally the WFI observations were hampered by bad weather leading to an efficiency of only 30%. At half time of the PhD the observational focus was to obtain data in all five filters for at least 1 square degree. This was successful in the 03h field. The above mentioned problems with the new instruments LAICA and OMEGA2000 made the development of new software and data reduction strategies necessary. As a result the reductions are still in progress at the end of the PhD thesis.

Table 3.2: List of observing runs at Calar Alto observatory using the 3.5m telescope equipped with the LAICA instrument which Siegfried Falter carried out. Column "Nights" gives the scheduled number of nights. The success rate in column "Data" denotes the percentage of observing time during which useful data have been taken.

Observing period					
Start	End	Observers	Nights	Data	Problems
26/5/2003	1/6/2003	Falter,Röser	12	0%	Two detectors broken, bad weather
17/11/2003	24/11/2003	Falter,Röser	8	0%	Bad weather
14/6/2004	20/6/2004	Falter,Hippelein	7	0%	Overhaul of telescope control system, bad weather
11/9/2004	16/9/2004	Falter,Hippelein	6	40%	Overhaul of telescope control system, bad weather
5/4/2005	9/4/2005		5	0%	Broken detector, OMEGA2000 service mode instead

From the beginning of the thesis the COMBO-17 data set was available for applying the cluster search and for testing procedures. The search results are presented in Chapter 6. Concerning the procedures to fix the selection function the first focus was laid on HIROCS for which the algorithms were developed until autumn 2005. The setup for the COMBO-17 selection function required a different approach in some parts compared to HIROCS. These changes were made starting in late 2005. In Chapter 5 the simulation setups for both data sets and the COMBO-17 selection function are introduced.

The overall data status as of March 2006 is the following (see also Fig. 3.10): OMEGA2000 observations have progressed rather well after the successful commissioning in 2003. More than 50% of the total survey area in the H band already have been imaged. For three of the four HIROCS fields at least 1 square degree in all filters is available yet. A large effort in early 2005 to collect H band data in the 10h field with sufficient quality (seeing better than $1.1''$) for the COSMOS team failed but the quality criteria of the MUNICS, HIROCS, and ALHAMBRA[6] surveys are fulfilled. After analysis of the data status as of March 2006 a new observational strategy until the end of 2006 has been proposed which would lead to the availability of 6.6 square degrees under perfect exploitation of telescope time. Under the pressure of the up-coming near infrared public surveys, like e.g. UKIDSS[7] (Lawrence et al., 2006) and FLAMEX (Elston et al., 2006), the optical data shall be gathered in the fields where already H band coverage is available. There the cluster analysis is planned to be carried out to secure the lead of HIROCS in comparison to these surveys which is based on the earlier commissioning of OMEGA2000.

---

[6] http://www.caha.es/newsletter/news05a/Moles/CANL_ALHAMBRA.html

[7] The UKIRT Infrared Deep Sky Survey, see http://www.ukidss.org/

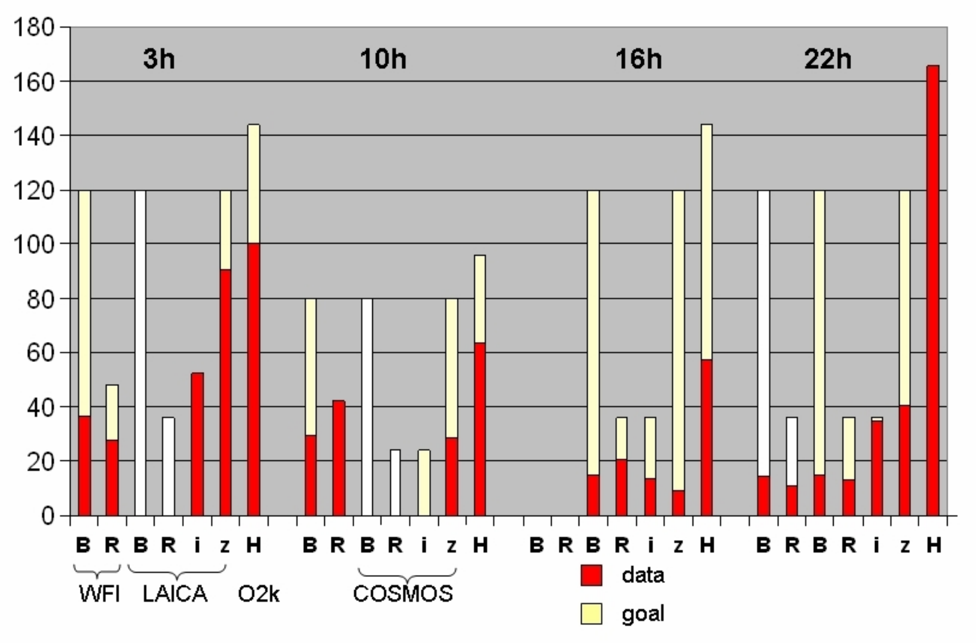

Figure 3.10: Exposure time histogram for the HIROCS fields in the different filters: The integration time is given in ksec. For the 10h field optical data from COSMOS are available. The total desired exposure time is indicated by the light yellow bars while the already observed data are marked red. For three of the fields the B and R band can be observed either with WFI or LAICA (the 16h field is not accessible from La Silla with WFI). White bars mean that the data are taken with the other instrument, respectively. Note that the data have not yet been cleaned for quality.

Chapter 4

HIROCS – Methodology

The previous Chapters described the definition of HIROCS as a survey dedicated to galaxy cluster finding at high redshifts. Here the two basic methodological ingredients to establish this survey shall be introduced and explained. In the first part the multi-color classification scheme which provides the object class as well as an estimation of the photometric redshift is described. After the general introduction of this procedure Monte-Carlo simulations to characterize the expected redshift accuracy for HIROCS show the feasibility of the survey in terms of the chosen filter set and depth of the exposures. With the knowledge of object class and redshift at hand the object catalogues can be selected for galaxies and after that searched for 3D object density enhancements. The description of the newly invented method to identify galaxy cluster candidates forms the second part of this Chapter.

4.1 Multi-color object classification

The experience from the CADIS and COMBO-17 surveys has shown that the accurate determination of the object class as well as redshift estimation is vital for studies of galaxy evolution with look-back time. These surveys rely on imaging data obtained with a set of medium and/or broad band filters. Taking spectra for a large number (several 1000) of extra-galactic faint objects on wide sky areas is extremely time consuming. Christian Wolf has developed as part of his PhD thesis (Wolf, 1998) a multi-color classification scheme which determines the object class for a large range of astrophysical objects and photometric redshifts for galaxies as well as quasars. This allows the creation of object catalogues in an unbiased way because no object pre-selection is imposed.

4.1.1 Method

The physical flux for all objects up to a given magnitude limit on the large-area survey exposures is determined with a specially for the survey goals tailored filter set. Based on these accurate flux measurements (see discussion of error determination in Chapter 3.4) color indices serve as indicators to classify the objects as well as to estimate the photometric redshift for galaxies and quasars. The spectrum of an object is sampled in this procedure by discrete filter measurements of the flux. Stars, galaxies and quasars are identified by matching the measured object colors in $n-1$ dimensions ($n=$number of filters) with synthetic colors collected in template libraries (see Sect. 4.1.2). After assigning the probability to belong to a certain class for each object, the redshift estimation is carried out using a Minimum Error Variance method which also delivers photometric redshift errors. The model libraries are assumed to be a widely complete representation of the objects' spectral energy distributions. The detailed mathematical outline of the method can be found in Wolf, Meisenheimer & Röser (2001) and the application to COMBO-17 is discussed in Wolf et al. (2004). Fig. 4.1 shows an example of the best-fitting template spectral energy distribution from the multi-color classification to an object measurement in the five HIROCS filters. This example galaxy was taken from the first HIROCS cluster candidate at z$\sim$0.7. It clearly shows the good match resulting from the fitting procedure and confirms the ability to accurately classify objects and determine photometric redshifts with the HIROCS filter set in concert with the depth of the exposures.

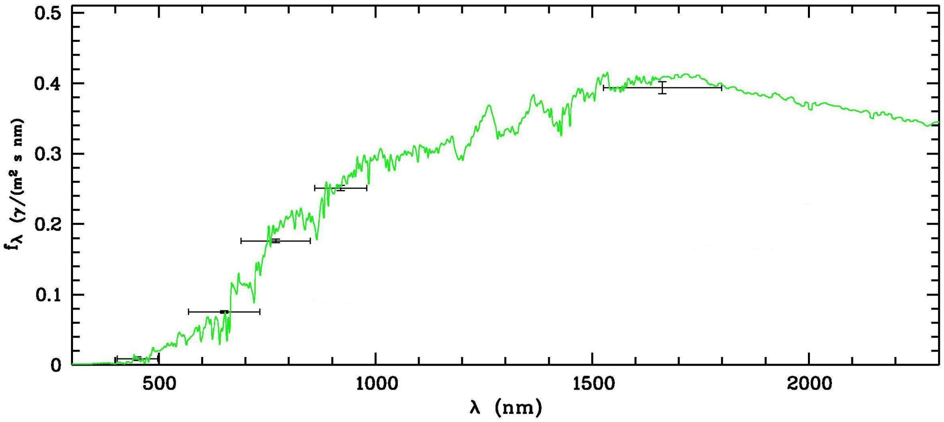

Figure 4.1: Example for the best-fitting template galaxy spectrum (green line) to the filter flux measurements in B, R, i, z, and H (black error bars). The estimated photometric redshift is 0.67 for this early-type galaxy with $R=22.82$.

4.1.2 Template color libraries

The variety of objects measured on the exposures is enormous ranging from stellar objects to galaxies and quasars. Each group has its own specific spectral features that could help or even complicate the multi-color classification. As a whole four template libraries are available which comprise the libraries for main-sequence stars, white dwarfs/horizontal branch stars, galaxies, and for quasars.
Here is a short description of the libraries[1]:

- The star library:
  It is based on the UK spectra of the Pickles catalogue (Pickles, 1998) which lists empirical spectra of 96 stars of the spectral types F, G, K, and M. Thereby it covers loosely the luminosity classes I to V.

- The white dwarf/blue horizontal branch star library:
  These library spectra are computed from theoretical models which are provided by D. Köster. The synthetic grid of DA type spectra covers effective temperatures from 6 000 to 40 000 K and surface gravities in the range $\log g = [6, 9]$. The low gravity values are consistent with models of subdwarf B-type (sdB) stars or blue horizontal branch (BHB) stars.

- The galaxy library:
  Since HIROCS is tailored to find high density peaks in the galaxy distribution the galaxy library is the most important ingredient of the multi-color classification. Recently it has been expanded to cover redshifts up to 2.0. On the basis of the PEGASE population synthesis code (Fioc & Rocca-Volmerange, 1997) galaxy template spectra have been calculated on a 2D grid covering 60 ages and 6 extinction levels. The ages range from 50 million to 15 billion years and the star formation rate was set up with an exponential decline ($\tau = 1$ billion years). The following assumptions were applied: Kroupa initial mass function, initial metallicity 0.01 and no extinction. Extinction plays an important role and is thus applied thereafter as a screen following the SMC law defined by Pei (1992) with six values of $\mathrm{E(B-V)} = [0.0, 0.1 \ldots, 0.5]$. The old library based on PEGASE covered the redshift range $\mathrm{z} = [0 \ldots 1.4]$ at a resolution of 0.005 on a log(1+z) scale (177 steps). The extension to $\mathrm{z} = 2$ became necessary because the MANOS project involves infrared observations including the *H* band (MANOS-deep). Therefore the templates have to cover a larger wavelength regime. Moreover it is foreseen to go out to redshifts of 1.5 for HIROCS or even 2.0 for COMBO-17+4.

---

[1] for more details see http://www.mpia.de/COMBO/combo_classy.html

- The quasar library:
  Quasars play a minor role compared to the galaxies for HIROCS. The SDSS template library is the basis for the quasar template which is varied in intensity, added to a power law continuum and multiplied by a redshift-dependent throughput function. The latter is modelling the absorption of Hydrogen bluewards of the Lyman alpha line. The redshift coverage is also on a log(1+z) scale (step size 0.01, 155 steps) from redshift 0.504 to 5.96. There are 20 different values covering the spectral index of the continuum and eight values of intensity relative to the mean template for the intensity of the emission line shape.

4.1.3 Redshift accuracy in COMBO-17

In the context of HIROCS the results from COMBO-17 serve as an optimal comparison sample. For the cluster survey it is not feasible to observe in as many filters due to the large area coverage. COMBO-17 has been carried out with 5 broad band and 12 medium band filters in the optical/near infrared at wavelengths from 350 to 930 nm. The large number of filters provides a good coverage of the objects' spectral energy distributions yielding very accurate photometric redshifts derived by the multi-color classification scheme. The deepest exposure was made in the R band and the photometric redshifts are most reliable at $R < 24\,\mathrm{mag}$. Applying a selection $R < 21\,\mathrm{mag}$ to the data in the Chandra Deep Field South the redshifts have an accuracy $\delta_{\mathrm{z}}/(1+\mathrm{z}) \sim 0.01$. With $R \sim 22\,\mathrm{mag}$ it is worse being around 0.02 and for $R > 24\,\mathrm{mag}$ the errors are on the order of 10% (Wolf et al., 2004).
The effects on the redshift accuracy of reducing the filter set to the five HIROCS filters and the planned depth of the exposures will be discussed in the following.

4.1.4 Accuracy of multi-color classification

As was shown before the photometric redshifts determined by the multi-color classification scheme from the measurements in 17 filters are extraordinarily accurate. The number of filters for HIROCS had to be reduced to only 5 as the aim is to search for clusters on a large sky area (see Sect. 2.1). The following questions arise: How well can the multi-color classification work for this reduced data set? What is the accuracy of the photometric redshifts? These issues will be tackled in this subsection by two approaches. The first is a complete Monte-Carlo simulation using the galaxy template library of the multi-color classification while the second approach uses the existing classified data set from COMBO-17 and takes advantage of the accurate knowledge of the best-fitting templates.

Monte-Carlo simulation with template library

The galaxy template library provides a large sample of synthetic galaxy spectra for the Monte-Carlo simulation. The strategy of this approach is to initially fix the R band magnitude for each library object. The simulation covers values in the range $R = [20, 21, ..., 25]$ mag. Using the colors of the library objects the other filter magnitudes used in HIROCS are calculated. The classification procedure works with the CD magnitude system. Consequently for the calculation of the color indices for the filters A and B the corresponding Vega color has to be taken into account. Each filter flux is accurate to an error $\sigma_{F_{phot}}$ due to the measurement. In the case of sufficiently small relative errors the corresponding magnitude error is of the order $\sigma_m \sim \sigma_{F_{phot}}/F_{phot}$. Following the definition of the color indices and the assumption of small flux errors the magnitude errors can be calculated by:

$$\sigma_m = \sigma_{flux,lim}\, 10^{0.4(m-m_{lim})} \tag{4.1}$$

with $\sigma_{flux,lim}$ being the flux error at the survey limits and m_{lim} denotes the limiting magnitudes of HIROCS, respectively. Normally the measurement procedure induces a spread

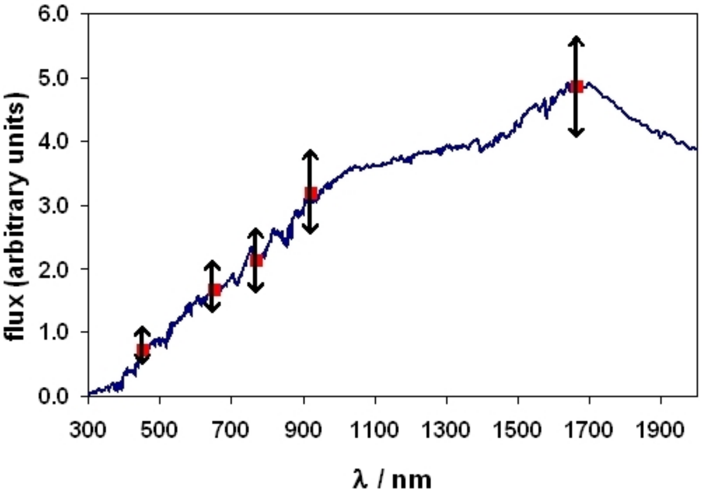

Figure 4.2: Illustration of imprinting Gaussian deviations to the flux/magnitude: the flux is given in arbitrary units, each filter is treated independently. The blue line is an arbitrary spectrum while the red squares mark the five filter measurements. The arrows indicate the measurement uncertainty which shall be simulated.

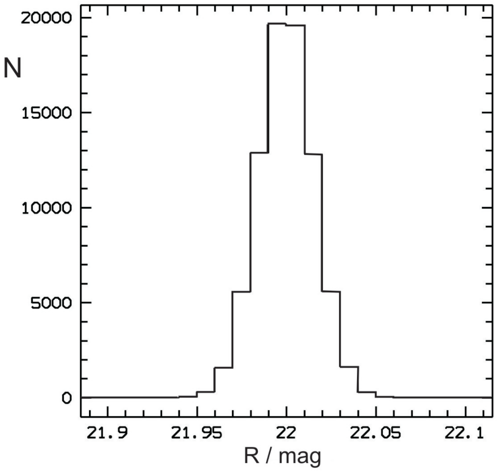

Figure 4.3: Distribution of the R band magnitudes after imprinting Gaussian deviations to the input R values of the library objects (here $R = 22$ mag).

in the magnitudes due to the measurement uncertainty. To come close to a real measured distribution Gaussian deviations (see Fig. 4.2) are computed and applied to the simulated magnitudes independently for each filter. Fig. 4.3 shows a histogram of the R magnitudes illustrating the result of imprinting Gaussian offsets for the simulation with $R = 22$ mag. After setting up the simulated catalogue the classification routine is run using the color indices $(B - R)$, $(R - i)$, $(i - z)$, and $(z - H)$ and all template libraries.

The subsequent analysis of the resulting redshifts and their accuracies as a function of the input R magnitude shows the following: As the survey is built up to search for elliptical galaxies at $z > 0.5$ in clusters the catalogues are selected accordingly to contain only this type of galaxies for the analysis. The galaxy template library contains model spectra for early and late-type galaxies at different redshifts and thus it contains a certain total number of elliptical galaxies which serves as reference. Comparing this number with the number of re-classified ellipticals from the simulation gives the rate of successful re-identifications. Fig. 4.4 shows the trend as a function of the input R magnitude. For the bright objects with values up to $R \sim 22$ mag this fraction is constant at a percentage of approximately 95%. It is not 100% because of the restriction to only five filters. Considering values of $R > 23$ mag the rate of re-classified ellipticals goes down reaching values of $\sim$50% at $R \sim 25$ mag. This decrease is ascribed to the limiting magnitudes. When objects fainter than the observing limit in one or more of the filters are analyzed the accuracy of the measurement is deteriorated and thus the classification becomes worse if not even

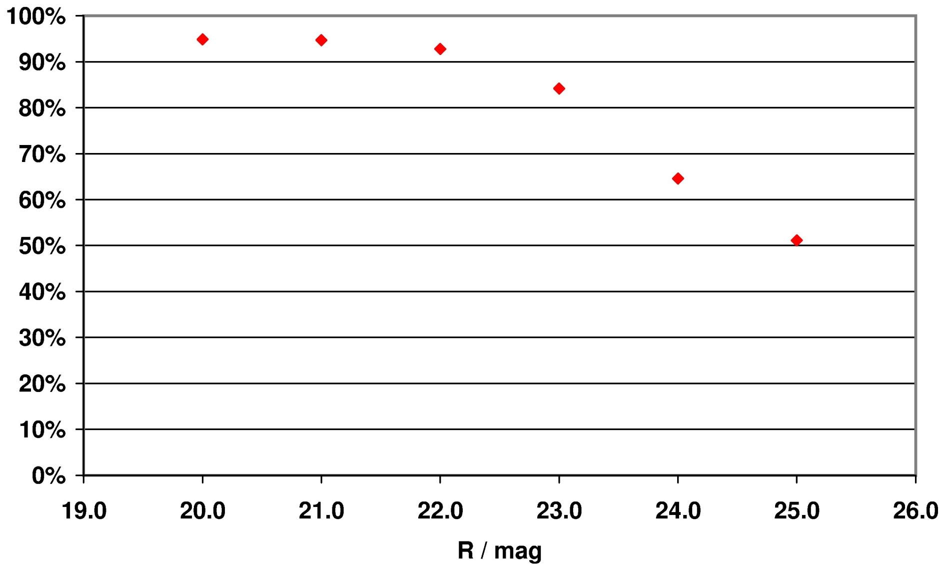

Figure 4.4: Percentage of successfully re-classified elliptical galaxies as a function of the input R magnitude. Only galaxies with original library redshifts $\mathrm{z} > 0.5$ are selected. At the survey limit in the R band more than 50% can be re-classified correctly.

impossible in the case too many filters are affected. Consequently the number of classified objects decreases.

Furthermore it is important to examine the quality of the multi-color classification in terms of redshift accuracy. It is quantified by the standard deviation $\sigma_{\mathrm{z_{lib}-z}}$ of the difference δ_{z} between the original library redshift $\mathrm{z_{lib}}$ and the redshift determined with only 5 filters. Again only elliptical galaxies are examined here. As a function of the input R magnitude Fig. 4.5 illustrates the deterioration of the redshift accuracy. At the bright end ($R = 21$ mag) the deviation is $\sigma_{\mathrm{z_{lib}-z}} < 0.02$ while at the very faint magnitudes $R = 25$ mag it is found to be of the order 0.16. Often the redshift errors are expressed in terms of $\delta_{\mathrm{z}}/(1{+}\mathrm{z})$ because the errors scale with $(1{+}\mathrm{z})$ for different redshifts. As a result the standard deviation of this quantity is 0.009 at $R = 21$ mag and 0.075 at $R = 25$ mag, respectively.

At this point it is important to note that this kind of simulation yields the best possible values for the redshift accuracies. The values are expected to be somewhat less accurate in reality. The explanation is that on the one hand the synthetic galaxy templates are only a limited representation of the variety of real galaxy spectra. On the other hand the

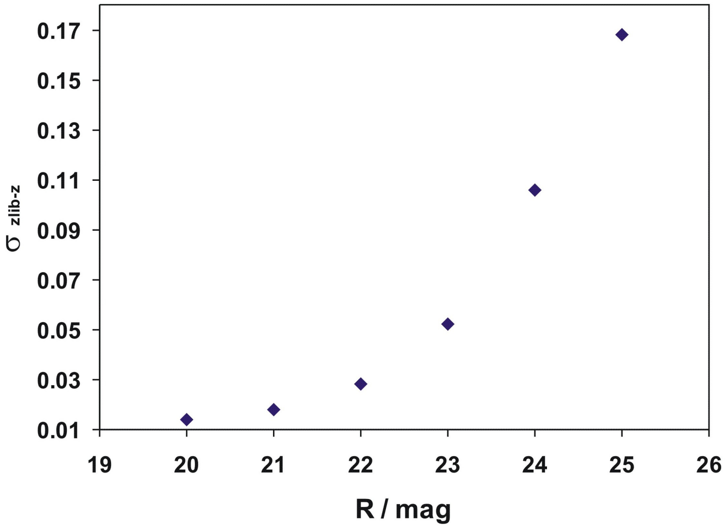

Figure 4.5: Standard deviation $\sigma_{\mathrm{z_{lib}-z}}$ as a function of input R band magnitude for the simulation based on the template library spectra.

assumption of Gaussian deviations for the measurement uncertainties is a simplification. As a whole the simulation shows that the redshift accuracy is worse in comparison to COMBO-17. This was expected due to the reduced number of filters but the rather high accuracies found in the simulation indicate that the survey will yield a well measured galaxy sample. The expected fraction of successfully reclassified elliptical galaxies supports this conclusion.

Simulation based on COMBO-17 data

COMBO-17 provides an extensive data set not only for the scientific exploitation but also for simulation purposes. The object catalogues have been classified with the multi-color classification scheme described in Sect. 4.1.1 and thus based on the measurements in 17 filters each object is assigned with a best-fitting template spectrum. Assuming these templates to be the best representation of the objects' spectral energy distributions the HIROCS measurements can be simulated by adopting the measured R band magnitude which is the deepest exposure and calculating the other HIROCS filter magnitudes via the best-fitting template colors. Again like in the Monte-Carlo simulation in the previous section magnitude errors are calculated using the limiting magnitudes (see equation 4.1).

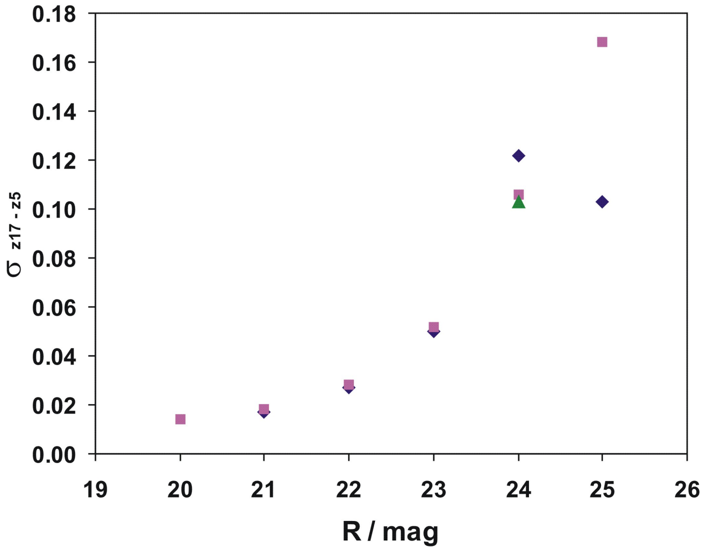

Figure 4.6: Standard deviation $\sigma_{z_{17}-z_5}$ as a function of input R band magnitude for the simulation based on the COMBO-17 best-fitting templates (dark blue diamonds). For comparison the magenta squares are the values $\sigma_{z_{lib}-z}$ from Fig. 4.5. The green triangle at $R = 24$ mag denotes σ with an additional selection $\sigma_{z_{17}} < 0.15$.

After that the magnitudes are deviated according to a Gaussian distribution for each filter measurement independently. The resulting 5-filter object catalogue is classified on the basis of four colors and analyzed.
Like in the previous simulation the redshift accuracy is estimated by the standard deviation $\sigma_{z_{17}-z_5}$ of the difference between the original redshift z_{17} from COMBO-17 and the newly determined redshift z_5. Fig. 4.6 illustrates the change of this indicator for objects which are classified as elliptical galaxies as a function of the R band magnitude. For this analysis a minimum and maximum redshift selection has to be imposed. At the high redshift limit at $z \sim 1.0$ COMBO-17 does not yield accurate redshifts anymore due to the filter set which only covers optical bands. The 4000 Å break of galaxies which is shifted into the near infrared sets this upper limit. HIROCS is set up to yield accurate redshifts at $z > 0.5$ with the B, R, i, z and the H filters. For lower redshifts the 4000 Å break is not straddled by two filters anymore and so an accurate redshift determination is not possible. The R band bin width is chosen to be ±0.2. At $R = 20$ mag no objects were left from the object table with these selection criteria. For $R < 24.0$ mag $\sigma_{z_{17}-z_5}$ is in very good agreement with the results from the simulation with the galaxy library. But at

$R = 24.0$ mag the standard deviation is higher. The reason is that the redshift accuracy from the 17-filter classification is lower for a significant fraction of the objects. In this case the re-classification with only 5 filters leads to a larger scatter of the newly determined redshifts. This issue can be tested by selecting at $R = 24.0$ mag objects which have original redshifts better than a certain threshold (here $\sigma_{\mathrm{z}} < 0.15$, see dark green triangle in Fig. 4.6). With that selection the agreement is very good and similar conclusions can be drawn as in the previously presented simulation. For even fainter R magnitudes the computation of $\sigma_{\mathrm{z}_{17}-\mathrm{z}_5}$ suffers from low number statistics.

4.2 Galaxy cluster finding

The ideal method for the selection of galaxy clusters is to search for object density enhancements in 3D space using the sky positions and the redshifts. Spectroscopic redshifts offer the highest accuracy but are observationally very expensive because of the extremely long exposure times to gain good enough signal-to-noise ratios for the detection of faint extragalactic objects. Although nowadays several multi-object spectrographs with high multiplexing capabilities – yielding up to 500 spectra with one exposure – exist, imaging is still dominating the field of large-area multi-band surveys. The survey imaging cameras provide the coverage of large sky parts with field sizes on the order of $15'$ to even 1° on a side. In connection with methods that determine very accurate photometric redshifts, surveys based on multi-color photometry are widely conducted. These photometric redshifts can be used for cluster finding procedures although their accuracy is worse than those derived from spectroscopy.

In Sect. 4.1.3 the redshift accuracy achieved in COMBO-17 has been discussed in more detail. Remind that at $R \sim 22$ mag $\delta_{\mathrm{z}}/(1+\mathrm{z}) \sim 0.02$ for the classification based on the 17-filter measurements. This redshift accuracy translates into an accuracy in velocity space of ~6 000 km/s using the simplifying assumption $\Delta\mathrm{z} \sim \Delta\mathrm{v}/\mathrm{c}$. From the simulations to test the 5-filter classification based on the galaxy template library at $R \sim 22$ mag the redshift accuracy was 0.028 leading to a velocity accuracy of ~9 000 km/s.

The redshift of a galaxy cluster is derived from the distribution of the galaxies' redshifts. The measurement is associated with an overall error which comprises the physical uncertainty due to the cluster's velocity dispersion and the uncertainty due to the measurement itself. Typical rich clusters show velocity dispersions in the range 800 to 1 000 km/s. Less rich systems like galaxy groups have somewhat lower velocity dispersions around 400 km/s. Regarding the rather large velocity accuracies with more than 6 000 km/s mentioned before it is clear that the cluster redshift uncertainty is dominated by the measurement uncertainty and does not sample the physical velocity distribution of

the galaxies. At this point the argument that the cluster finding on the basis of the photometric redshifts is highly insecure comes up. A significant physically bound galaxy over-density still shows up as an excess of the local galaxy density. The distribution of the galaxies' redshifts appears simply broader. Galaxy clusters contain a high number of galaxies which appear highly concentrated compared to the surrounding large-scale structure both in sky position as well as in redshift space. Although being washed out in redshift space a suitably strict selection of the density cut (explained later-on in this Chapter) is expected to filter out the group and cluster candidates. This means that the highest density peak namely the group/cluster center will be detectable to some significance level which is expected to depend on contamination issues. To be able to quantify the problem of fore- and background contamination and to characterize the finding scheme Monte-Carlo simulations of galaxy clusters which are inserted into the real data set are performed (see Chapter 5). These simulated clusters are subject to the cluster finding and the recovery rate $\mathrm{R_{rec} = N_{out}/N_{in}}$ characterizes the finding capabilities of the search method. With these simulations the effect of possible false discoveries and the ability of finding galaxy associations can be quantified. The result of the cluster finding is a catalogue listing cluster candidates. As these clusters are regarded only candidates follow-up observations are needed for their ultimate spectroscopic confirmation.
In the following the scheme for the galaxy cluster finding is described.

4.2.1 Finding scheme

The procedure uses the position on the sky and the photometric redshifts from the multicolor classification. Around each object of the object catalogue a suitable fraction of an Abell radius $\mathrm{R_A}$ (Abell, 1958) is drawn. The Abell radius is a rather arbitrary choice for the distance to the cluster center which was used by G. Abell to quantify the richness of clusters which has been published in his famous first catalogue of galaxy clusters in 1958. It is parameterized like this: $\mathrm{R_A} = 1.5\,h\,\mathrm{Mpc}$. Its choice has been motivated by the fact that a cluster has to be suitably compact to be identified as a physically bound entity. In combination with the richness estimation where the number of objects in a range of brightness $[\mathrm{m_3, m_3{+}2}]$ is counted the clusters have been identified at that time. $\mathrm{m_3}$ denotes the brightness of the third brightest galaxy. The value of the search radius adopted for the cluster search is motivated like this:
King's approximation (King, 1968) of the projected surface distribution of stars in globular clusters is based on the assumption of a self-gravitating isothermal sphere.

$$\mu = \mu_\circ \left[1 + \left(\frac{\mathrm{r}}{\mathrm{r_c}}\right)^2\right]^{-1} \tag{4.2}$$

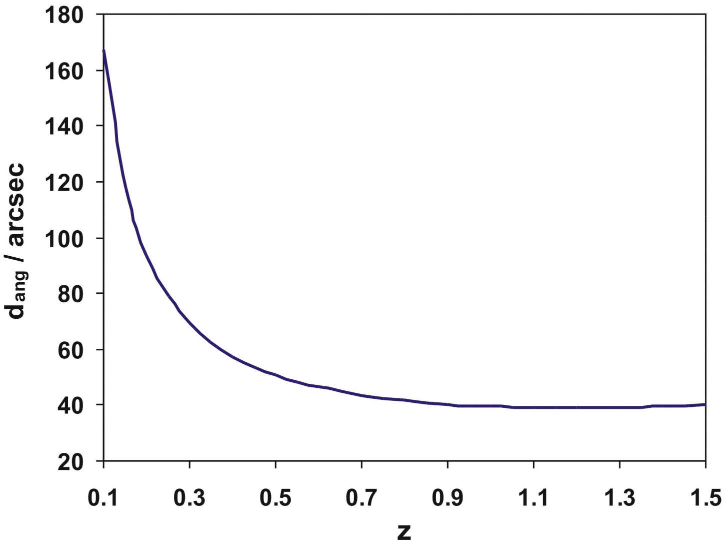

Figure 4.7: Apparent angular size, see equation 3.1, in arcsec as a function of redshift z for a true physical size of 300 kpc. The calculation is based on the analytical fit to the luminosity distance D_L from Pen (1999).

with r_c being the core radius and ρ_o the density at the center of the profile (Fig. 4.8). This approximation can be applied for the fitting of the projected number density distribution of the galaxies in clusters. Often the general form of a two-dimensional β-model with the exponent as a free parameter is used. Adami et al. (1998; 2001) found this kind of core models reproducing well the density profiles of rich clusters in the ENACS (ESO Nearby Abell Cluster Survey) catalogue. In a more recent study Strazzullo et al. (2005) analyzed a sample of 28 compact Abell clusters in terms of morphology and determined shapes as well as profiles. The median core radius of this sample is $r_c = 310$ kpc but 1/3 of their clusters appear to have core radii smaller than 100 kpc. This is an indication that a non-negligible part of the clusters rather show very cusped profiles.

Motivated by this study a value of 300 kpc (equivalent to 1/5 of an Abell radius) is chosen for the search aperture in our procedure. Lower values lead to a worse contrast because neighboring objects are lost within the counting procedure. Too large search apertures increase the noise due to the increasing number of objects which do not belong to the cluster candidate. The apparent angular sizes d_{ang} of cosmological structures like e.g. galaxy clusters with a physical size of $d_{phys} = 300$ kpc behave like it is shown in Fig. 4.7. The corresponding angular extent is $\sim 2.8'$ at a redshift of 0.1 and $\sim 38''$ at a redshift of

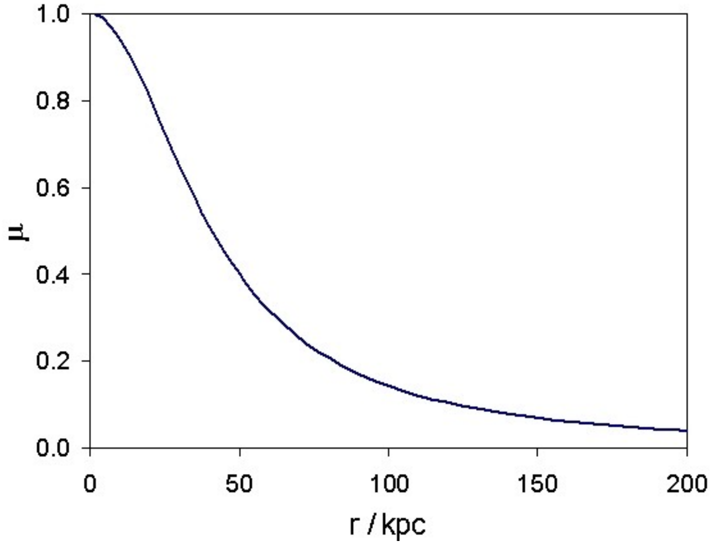

Figure 4.8: Surface density distribution according to King (1968): $\mu_\circ$ is set to 1 arbitrarily. The radii r are given in kilo parsecs kpc, $r_c = 41$ kpc.

1. This effect is taken into account, too.
The third dimension for the counting of physically close objects is opened up via applying a limit in velocity space. The multi-color classification provides an estimation of the photometric redshift and a corresponding dispersion which are used to calculate the distance in velocity space between either two objects. Perry & O'Dell (1978) have derived the velocity difference of two close objects at cosmological distances:

$$\left|\frac{v}{c}\right| = \left|\frac{(1+z_1)^2 - (1+z_0)^2}{(1+z_1)^2 + (1+z_0)^2}\right| \leq \left|\left(\frac{v}{c}\right)_{\lim}\right| \tag{4.3}$$

z_0 is the photometric redshift of the object around which the search aperture is drawn and for z_1 the redshifts of all other objects are inserted. To separate neighboring objects a velocity limit $v_{\lim}$ is applied along these lines. Since the distance calculation is done in velocity space the velocity scatter is calculated from equation 4.3 (see also Addendix D). Each object in the considered field has a certain probability to be found within $\pm v_{\lim}$. The probability distribution for the velocity difference v_{diff} (equation 4.3) between the respected object and all other objects is assumed to be Gaussian with the width calculated

Figure 4.9: Illustration of the counting procedure: For one example object (left image, red rectangle) a search aperture which is a fraction of the projected Abell radius (yellow circle) is drawn. Taking into account a velocity cut (see Fig. 4.11) in the redshift direction all objects within this 3D volume (right image, orange rectangles) are counted. For the choice of the exact values see the text.

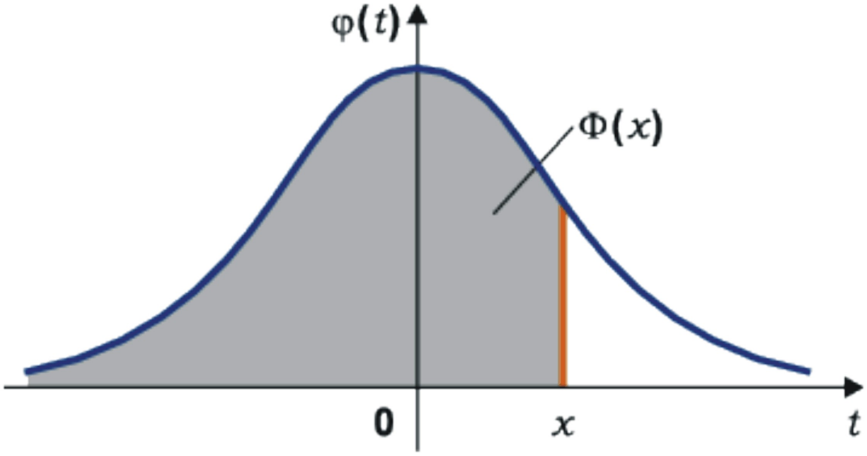

Figure 4.10: Normal distribution (Bronstein et al., 1999): ϕ(t) describes the Gaussian distribution while the area below the curve with the limit x denotes the integral of this function $\Phi(x)$. The (0,1)-normalized distribution function is available as a table.

from the photometric redshift errors ($1\,\sigma$, Fig. 4.10):

$$\Phi(\mathrm{v_{diff}}) = \frac{1}{\sqrt{2\pi}} \int_{-\infty}^{\mathrm{v_{diff}}} \mathrm{e}^{\frac{\mathrm{t}^2}{2}} \mathrm{dt} \tag{4.4}$$

For the counting only the area of the normal distribution – the probability – which falls into the velocity interval $[-\beta, +\beta]$ is included (see Fig. 4.11). Several cases can be distinguished because the distribution can fall almost completely or only partly into the interval $[-\beta, +\beta]$. This means that also objects with $\mathrm{v_{diff}}$ outside the interval can contribute to the counting due to large redshift errors.

Fig. 4.9 in combination with Fig. 4.11 illustrate this counting procedure.

From the number counts in the 3D aperture a density estimator is calculated. Before the counting procedure of the cluster finding an average object density from the whole image is computed. Thereby the redshift range is divided into bins. The density is determined by counting the probabilities of all objects to be found in the relevant redshift bin which is done the same way as the counting procedure on the basis of Gaussians explained before. The division of this number count by the area covered by the image yields an expected average object density as a function of redshift. These density values are later on interpolated at the redshift of each object considered in the cluster finding part to yield an expected object density and an expected number of objects respectively. The division of the number counts within the 3D search volume and these expected numbers yields the values for the density estimator which is normalized to 1. The selection of suitable galaxy cluster candidates is presented in the next subsection.

4.2.2 Over-density selection

The distribution of the normalized galaxy densities is used to select the galaxy cluster candidates. In the three COMBO-17 fields more than 20 000 objects have photometric redshifts assigned by the multi-color classification. In the case of a homogeneous distribution of such a large number of objects in 3D space the density distribution could be well approximated by a Gaussian. Following this assumption a Gaussian is fit to the rising flank of the density distribution and its width serves as a measure for significance levels to select the object catalogue to find regions with high object densities. For the analysis presented in this thesis $>3\sigma$ cuts are used to identify over-dense regions. This technique of enhancing the density contrast is illustrated in Fig. 4.12. The red continuous line represents the fit to the rising flank. There the true distribution is well described by a Gaussian while beyond the maximum at high density values considerable density excess is obvious. This stems from the regions where groups and/or clusters appear as high-density peaks. The procedure of enhancing the density contrast is visualized by the two vertical

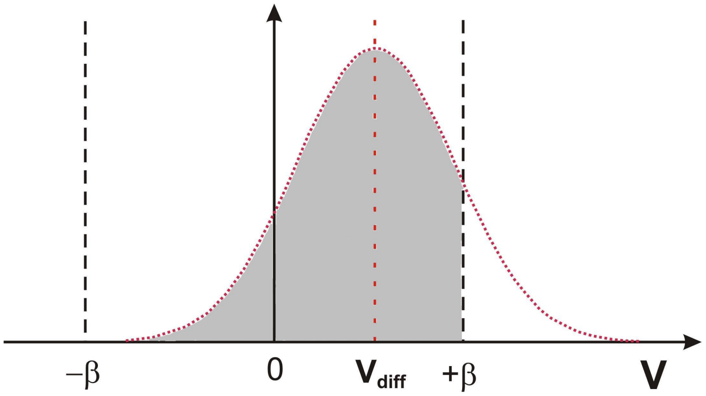

Figure 4.11: Illustration of the velocity limit $\pm\beta$ and Gaussian probability distribution: the velocities are always referred to the respected object which serves as the zero point of the relative velocity v. All other objects are checked for being close in the velocity interval $[-\beta, +\beta]$. $\mathrm{v}_{\mathrm{diff}}$ denotes the relative velocity of an arbitrary object. The grey shaded part is the area over which the integration has to be carried out.

red dashed lines. The left denotes the peak of the distribution and the right is placed at the 3σ cut mentioned before. Fig. 4.13 illustrates the contrast enhancement in the $[\mathrm{x}, \mathrm{y}]$ distribution of the objects (left: density > 1, right: density > 1.9). Without selection the field is so dense that no features would be visible but with the low-density selection the contrast already is better. The high-density 3σ cut significantly selects the densest regions which are regarded as the group/cluster candidates. The influence of imprinting this density cut will become more obvious in Chapter 6 when the results of the cluster search in COMBO-17 data are presented.

4.2.3 Position and redshift estimation

After the determination of the significance level and selecting the object catalogue accordingly, regions with high galaxy density remain. In the case several objects are so close together that these could be members of a possible cluster first the position and after that the redshift is estimated.

Estimating the candidates' positions is performed by the following procedure: The selected object catalogue is used to produce a smoothed image of the object distribution with high density contrast. At each galaxy position a Gaussian is placed with the value

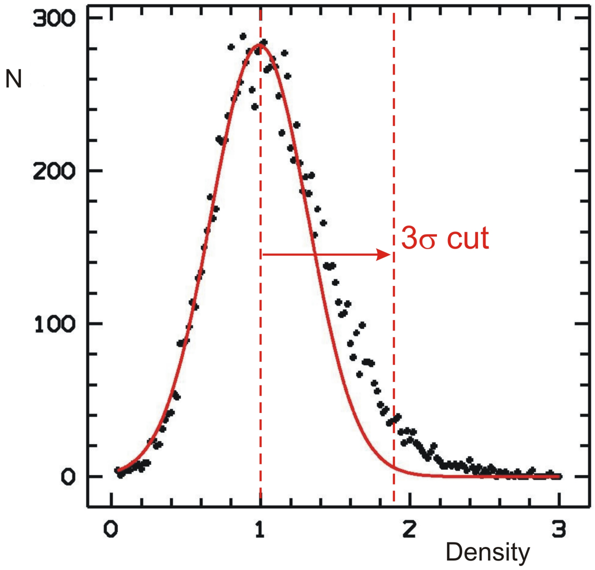

Figure 4.12: Normalized density distribution from one of the COMBO fields: Small black squares are data points, the red line is the fit to the rising flank of the distribution. The left vertical red dashed line indicates the position of the peak and the right red dashed line shows the cut assuming 3σ over-dense regions.

from the density estimator for the height and a FWHM[2] of a suitable value. The typical cluster profile is described by a King profile (see equation 4.2 and Fig. 4.8) and its size (core radius) is on the order of 300 kpc. This value was already chosen for the radius of the cluster search aperture and is applied in this context for consistency. The apparent angular size is dependent on redshift (equation 3.1) which is respected here, too (see Fig. 4.7).

The next step is the extraction of objects from these smoothed images with the help of the SExtractor (Bertin & Arnouts, 1996) software. For this the search parameters have to be tuned to the special purpose. The process of imposing Gaussians with widths on the order of $40''$ to $70''$ leads to a superposition of the Gaussians for very close objects. The closer the objects are and the more objects cluster together the broader and the higher the resulting distribution is. Single alone standing objects can be easily rejected by selecting objects with a "flux" value above a suitable limit. The "flux" value is determined by the SExtractor routine. For the position estimation of the cluster candidate

---

[2] full-width at half maximum

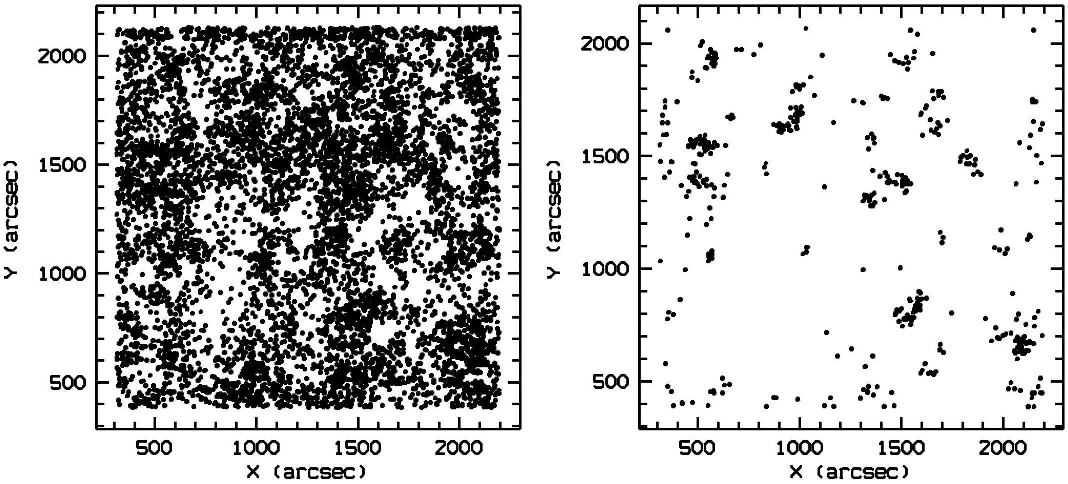

Figure 4.13: Effect of applying density cut: Left: [x, y] distribution in example field after selecting density > 1.0 (see Fig. 4.12 left vertical red dashed line). Right: Same field with density > 1.9 (Fig. 4.12 right vertical red dashed line).

the FLUX_PROFILE parameter is chosen which yields the peak flux weighted with the FWHM of the distribution. Alone standing galaxies have a "stellar" appearance while agglomerates of galaxies appear as "extended" objects. The cluster candidates and their positions in [x, y] determined by SExtractor are identified if the weighted flux exceeds a threshold in the parameter FLUX_PROFILE. At the end an output cluster candidate table with the flux estimations, the positions as well as several SExtractor morphology parameters is created.

Once the positions have been fixed the redshifts of the cluster candidates are measured by searching for peaks in the redshift distribution. Still at the same density contrast level all objects in a box with fixed size of 300 arc seconds in [x, y] are selected. To exclude objects of a possible foreground cluster an optional minimum redshift can be also given for the selection. The redshift histogram is produced under consideration of the redshift error of every single galaxy. For the counts the Gaussian probability of the object to be found within a certain redshift bin (width $\Delta z = 0.05$) is used. See also the description of the counting to determine the local object densities in the search procedure (Sect. 4.2.1). Consequently a galaxy with a well determined redshift within a redshift bin contributes more strongly to the counting because the Gaussian probability distribution is concentrated. A galaxy with a large redshift error has a broader Gaussian distribution and thus a smaller probability value is added. Although the probability of the latter is small it has to be respected for the counting to produce the histogram. The peak finding algorithm determines the maximum of the number of objects in the histogram and the corresponding redshift. It is assumed that at this central redshift the distribution of the redshifts is Gaussian. The width of this Gaussian is found by looking for the redshift where the object number decreases to half of the maximum value. Because in each histogram several peaks with varying object numbers can show up a range around the central redshift ($\pm 3\sigma$) is excluded from the subsequent search. The redshift and its 1σ scatter are added to the cluster candidate table.

4.2.4 Richness estimation

The total mass is one of the fundamental physical parameters of galaxy clusters. It can be measured on the basis of X-ray data, velocity dispersions, and strong as well as weak lensing. However, all these methods require data sets which are hard to obtain for a statistically large cluster sample. Low mass systems often can not be covered by these data. The cluster richness which quantifies the number of galaxies contained in a cluster can be expected to correlate with the total cluster mass. But the estimation of cluster richness poses a difficult task due to the problem of fore- and background contamination. Abell (1958) introduced his famous richness classification which sorts galaxy clusters according to the number of cluster members. For this all galaxies in an apparent magnitude range $[\mathrm{m}_3, \mathrm{m}_3{+}2]$ (m_3: magnitude of the third brightest cluster member) are counted. Richness class 0 means that the cluster contains 30 to 49 galaxies, more than 50 galaxies is richness 1, more than 80 corresponds to richness 2 and so on. A severe problem arises due to the choice of the third brightest galaxy in apparent magnitude. The richness is thus not measured in a fixed absolute magnitude range and therefore bright foreground galaxies can impose random errors. A more detailed discussion of the richness estimation problem can be found in Gal et al. (2003).

Gal et al. introduced an alternative to estimate cluster richness which is based on counting galaxies in the same absolute magnitude range for all clusters and within a radius of $1\,h^{-1}$ Mpc. The fixed magnitude range is $M_r^\star - 1 < M < M_r^\star + 2$ where they used r band data and assumed $M_r^\star = -21.53$ based on luminosity functions from Paolillo et al. (2001). At low redshifts the magnitude interval is not affected by completeness. But at higher redshifts these authors apply a correction to account for the richness underestimation caused by the fact that at the survey limits the objects can not be measured reliably anymore. As Gal et al. and later on Lopes et al. (2004) have shown this richness estimator yields better results and therefore it is adopted here to perform measurements of the candidates' richness.

Here is the recipe for the richness estimation: around the center positions of the cluster

candidates a rectangular box with a size of $1\,h^{-1}$ Mpc (∼1.4 Mpc with $h = 0.72$) is drawn to count all galaxies within a redshift range $\mathrm{z} \pm \sigma_{\mathrm{z}}$ and the above mentioned absolute magnitude range but now using the B band. The exact choice of the luminosity function parameters ($M_B^\star$, α) which differs from Gal et al. will be motivated in Sect. 5.2.1.
The resulting number has to be corrected for two different contributions. With the counting procedure cluster galaxies and interlopers cannot be separated which imposes a contamination and thus leads to a richness over-estimation. To estimate the degree of contamination the expected number of field objects is estimated by determining the object density from the whole image and dividing by the image area. This number is subtracted from the uncorrected richness. Additionally a completeness correction has to be carried out because at the faint end more and more galaxies cannot be classified and so have no redshift estimation. For COMBO-17 the completeness has been determined as a function of the R band magnitude (see equation 5.11) but for HIROCS this has yet to be determined after the final reductions. By simply comparing the object numbers with and without estimated photometric redshifts in the vicinity of the cluster candidate one gets a handle on the completeness. The difference between both is added to the number estimation.
The significance can be quantified by comparing the richness values (denoted $\mathrm{N}_{\mathrm{gal}}$) of the candidates with the results from the galaxy cluster simulations which serve to determine the selection function (Sect. 5.2.1).

Chapter 5

Cluster finding – Selection function

The search for galaxy clusters in the optical/near infrared regime is complicated by fore- and background contamination. While the sky position poses no problems – e.g. in COMBO-17 the astrometry is accurate to better than $0.15''$ (Wolf et al., 2004) – the accuracy of the photometric redshifts usually is an order of magnitude worse compared to typical velocity dispersions of rich clusters of galaxies (see discussion in Sect. 4.2).

The effects of the contamination are usually studied by simulating galaxy clusters and inserting them into the real object catalogue. The search for these artificial clusters provides a tool for understanding the selection procedure of a search algorithm. The analysis gives important hints concerning difficulties and/or peculiarities of the underlying search method. A Monte-Carlo simulation of a statistically significant number of simulated clusters leads to the selection function. It determines the recovery rate as a function of redshift and richness. For the simulations the real 3D galaxy distribution with its large-scale structure features is most suitable. No artificial background is used here because this would lack the cosmic structures and the selection function would possibly be too optimistic. A detailed discussion of these galaxy background issues can be found in Goto et al. (2002), Kim et al. (2002), and Lopes et al. (2004).

Another important characteristic is the false-discovery rate. It quantifies the number of false detections in case of an idealized 3D object distribution which is uniform and contains no density enhancements. The false-discovery rate can be determined by randomizing the positions in the real object catalogue (see e.g. Goto et al., 2002) and serves to fix detection thresholds.

The first part of this Chapter introduces the basic setup of the simulation procedure for HIROCS. Thereby first tests to find out the performance of the methods are presented. COMBO-17 has been intensely analyzed and thus empirical relations like for the redshift scatter as a function of the R band magnitude can be used to simplify the simulation procedure. The description of the simulation setup opens the second part of the Chapter where additionally the selection function for COMBO-17 is presented in detail.

5.1 HIROCS

The cluster search algorithm uses the position, photometric redshift in concert with its error and a magnitude which is usually the deepest filter exposure of a multi-color data set. Artificial clusters should thus contain galaxies which have the same photometric and redshift properties as would be measured in the survey observations. This means for the former that the magnitude accuracy shall be governed by the survey limiting magnitudes. Additionally, the spatial distribution of the galaxies and the luminosity function should be set up in an analogous way to that found in real clusters.

The simulations for HIROCS comprise four basic steps which are performed using three different procedures. First of all the input magnitudes for the simulation algorithm which sets up the synthetic clusters are determined. With this provided a cluster with magnitudes and positions for each member galaxy is calculated. After that the multi-color classification scheme is run to determine the photometric redshifts and finally the cluster is inserted in the real object catalogue. The last step will be possible not until the first HIROCS data set is available. Thus only the first three steps are explained in the following. At the end of this section the output of the simulations is discussed.

5.1.1 Calculation of magnitudes

The calculation of the HIROCS limiting magnitudes ($L^{\star}$+1) for an elliptical galaxy at redshift 1.5 (5σ) was explained in Sect. 2.2. The same basic procedure is applied for the calculation of the simulated absolute magnitudes. Here the redshift range $0.5 < z < 1.5$ will be covered in steps of 0.1. For each step in redshift the following has to be done:

Bell et al. (2004) provides an empirical relation for the redshift evolution of the rest-frame *B* band luminosity for red-sequence galaxies in COMBO-17 (Fig. 2.4). Up to redshift 1.1 the values can be directly adopted while beyond that the relation is extrapolated. For each redshift step a suitable template galaxy spectrum is searched for in the galaxy template library (see Sect. 4.1.2). At redshift 1.5 the template which was used for the determination of the HIROCS magnitude limits is kept. It was selected to have a rest-frame color following equation 2.1. This template is based on a certain formation age and its formation redshift serves as a zero-point for the age determination of the suitable templates at lower redshifts. For this calculation the internet tool "Cosmological Calculator"[1] is used which

---

[1] http://www.arcetri.astro.it/~zappacos/cosmo_calc.html

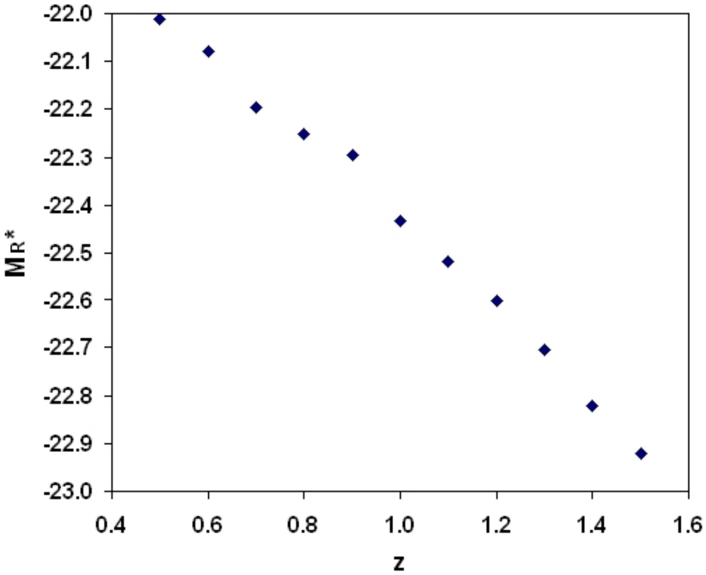

Figure 5.1: Rest-frame R band magnitudes $\mathrm{M}_R^\star$ for red-sequence galaxies as a function of redshift calculated from the galaxy template library spectra. These were selected to meet empirical color relations measured in COMBO-17.

incorporates the integration of a relation for the lookback time provided by Hogg (1999). The redshift difference between the respected and the zero-point redshift corresponds to a time interval which is the formation age of the galaxy template spectrum to be selected from the template library. The spectrum is then scaled so that its absolute B band magnitude equals the values from Bell et al. (2004). Convolving the spectrum with the filter transmission functions yields the corresponding rest-frame magnitudes in B, R, i, z, and H. Fig. 5.1 shows the absolute R band magnitude $\mathrm{M}_R^\star$ as a function of redshift resulting from these calculations. These serve as the characteristic magnitudes for the computation of the luminosity function in the cluster simulation. In this context, it is important to note that the selection procedure to find the galaxy template spectrum with the correct color intrinsically incorporates the evolution of the galaxies' SEDs. Thus no evolutionary correction needs to be applied for the calculation of magnitudes.
A similar calculation has been done for the blue galaxies. The empirical rest-frame B band relation for the blue templates was taken from Wolf et al. (2003). Values for $\mathrm{M}_B^\star$ at redshifts larger than 1.1 were extrapolated. The templates were selected by using the

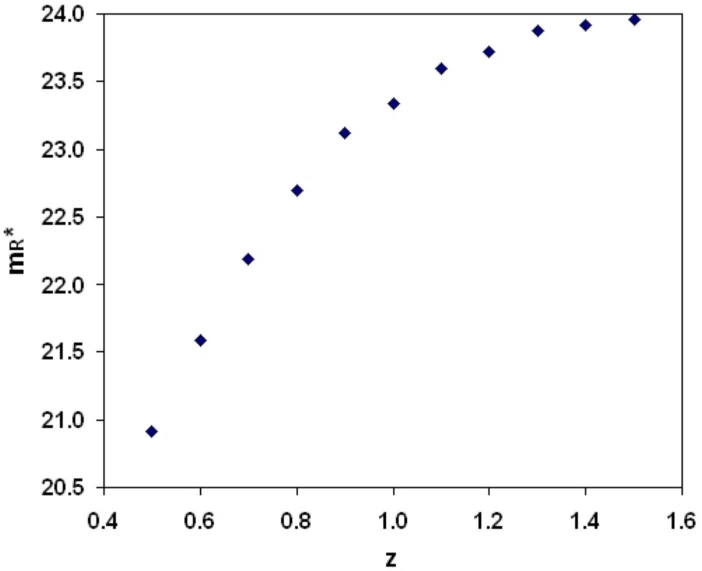

Figure 5.2: Apparent *R* band magnitudes $m^{\star}_{R}$ for red-sequence galaxies as a function of redshift.

following rest-frame color relation, again Faber et al. (2006):

$$(U - V)_{\text{blue}} = 0.75 - 0.65z - 0.08(\mathrm{M}_V - 5\log h + 20) \tag{5.1}$$

The template at redshift 1.5 is based on a certain formation age which serves as the zero-point for the ages of the templates at lower redshifts. These ages are estimated like described for the red-sequence galaxies. All other steps mentioned above are repeated for the blue galaxies to calculate the input magnitudes for the cluster simulation.
Having provided the input magnitudes the cluster simulation program can be run.

5.1.2 Synthetic clusters

Galaxy clusters are a mixture of all galaxy types while elliptical galaxies dominate the cluster population in most clusters (van Dokkum et al., 2000). For the simulations, which shall be carried out in the redshift range $0.5 < z < 1.5$ with steps of 0.1, two types of galaxies are selected to populate the cluster: 60% elliptical for the red-sequence population and 40% spiral galaxies representing the blue-cloud population. Each galaxy is assigned with absolute magnitudes (see Sect. 5.1.1) for the HIROCS filter set at a given redshift following a Schechter (1976) luminosity function. The simulated magnitudes in the desired filter should accurately follow the survey characterization (magnitude limits, see Sect. 2.2) on the one hand. On the other hand typical cluster peculiarities like the faint-end slope α have to be accounted for equally. In a recent study of the luminosity functions of 69 clusters from the RASS-SDSS galaxy cluster sample Popesso et al. (2006) have found $\alpha_{\mathrm{red}} = -0.8$ for the red and $\alpha_{\mathrm{blue}} = -1.6$ for the blue galaxy population. These parameters are adopted for the simulation procedure. The richness of the simulated clusters which is based on the definition presented in Gal et al. (2003), see Sect. 4.2.4, is controlled by the normalization of the luminosity function. The desired magnitude range is split into bins of width 0.5 mag and the magnitudes are distributed evenly in the bins. After that apparent magnitudes are calculated with the equations 2.2, 2.3, and 2.4. Additionally the K correction has to be applied (see Sect. 2.2). Fig. 5.2 shows the apparent R band magnitude as a function of redshift, it is the characteristic magnitude of the luminosity function. Magnitude errors are computed using equation 4.1. After having calculated the magnitudes the objects are distributed following a projected surface density profile. Here again a King profile (see Sect. 4.2.1, Fig. 4.8) is used to approximate the projected distribution of cluster galaxies. The values for the core radii are set to 300 kpc at the clusters' redshift and the profile is cut off at 2 Mpc in the co-moving frame. Usually the brightest cluster galaxy is found in center. Therefore it is assured that the brightest galaxy of the simulated cluster is located in the center.

For the next step, the multi-color classification, a catalogue with cluster galaxies listing the positions and all the synthetic filter magnitudes is provided.

5.1.3 Classification of clusters

The photometric output for a simulated cluster is set up to resemble as close as possible real measurements. COMBO-17 relations were used for that. Similar to the real case the synthetic object catalogue can be classified in terms of the colors. For HIROCS the relevant color indices are: $(B-R)$, $(R-i)$, $(i-z)$, and $(z-H)$. The errors of the color indices are essential and calculated from magnitude errors. As a result the object class and the estimated photometric redshift are provided for all the galaxies in the artificial cluster.

This step is necessary as long as no empirical relations for the redshift scatter as a function of e.g. the deepest exposed filter from HIROCS are available. As will be shown in the second part of this Chapter the simulations for the COMBO-17 selection function are based on such relations.

5.1.4 First tests

In summary the techniques as well as the corresponding algorithms are developed and can be applied to the HIROCS data set. But as outlined in Sect. 3.10 no reduced and classified HIROCS data set is available yet. Since the determination of the cluster selection function shall be carried out using a real galaxy catalogue the focus was directed to the COMBO-17 data set. To conclude this part some first tests of the procedures are presented in the following.

First of all the setup of the magnitudes can be tested by examining the K and evolutionary correction (termed K+E correction in what follows). Here the combination of the two is considered because the templates selected for the redshifts at which the simulations shall be carried out include the evolutionary correction. The K+E correction is calculated using the selected template spectrum with formation age t for redshift $\mathrm{z_i}$ by:

$$\mathrm{K + E = 2.5 \log \frac{f_{\nu,t}(z = 0)}{f_{\nu,t}(z = z_i)}} \tag{5.2}$$

with the flux of the template at the redshifts 0 and $\mathrm{z_i}$. Poggianti (1997) has provided a compilation of formulae and tables for the K corrections of different template spectra at various redshifts. A comparison to these values can give hints whether the above described technique to calculate the magnitudes is correct. In this work the galaxy template spectra are based on the spectro-photometric model from Poggianti & Barbaro (1996). For the comparison suitable templates with the correct age for the respected redshift were selected[2] and the K+E correction determined following the above described recipe. The result is displayed in Fig. 5.3. A different cosmology ($\mathrm{h = 0.5}$) in Poggianti's work leads to different formation ages of the templates. If the cosmology is changed such that $\mathrm{h = 0.72}$ like it is assumed in this thesis the orange triangles are the result. Clearly the solution for HIROCS lies in between the two solutions derived with the templates from Poggianti. At redshift 0.7 there is a deviation of ∼8% and of ∼10% at 1.0. These rather small deviations can be explained easily by the use of different spectro-photometric models, the templates in this thesis are based on the PEGASE code (Fioc & Rocca-Volmerange, 1997).

For a second test Fig. 5.4 shows the color-magnitude relation $(R-z)$-z for the elliptical galaxies. The magnitudes denote the characteristic knee magnitudes in the ABmag system. These are resulting from a convolution of the absolute magnitudes with the filter transmission functions, and calculating the apparent magnitude at the respected redshift. Each z magnitude corresponds to a certain redshift. The slope seen in this graph can be understood by considering the redshifting of the 4000 Å break through both filters. With

---

[2] from http://vizier.u-strasbg.fr/viz-bin/VizieR-3

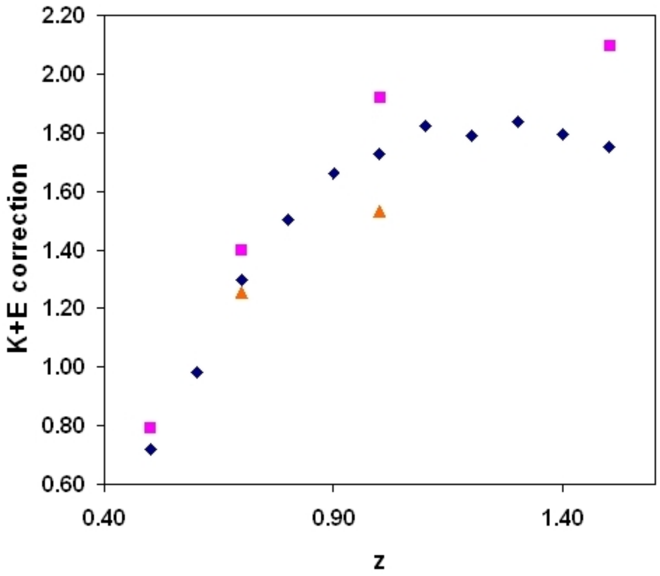

Figure 5.3: Combined K+E correction as a function of redshift for early-type galaxies. Dark blue diamonds: derived from the simulation input calculations based on COMBO-17 data. Magenta squares: based on template spectra with the formation age provided by Poggianti (1997). Orange triangles: based on the Poggianti templates but with formation age adjusted to the cosmology used in this thesis.

rising redshift it enters the R filter (at redshift ∼0.5) and leaves at even higher redshift (∼0.9). The intrinsic brightness thus decreases. At the same time the object becomes weaker due to its increasing distance. But this is valid for both filters so that the brightness decrease can be fully ascribed to the 4000 Å break and thus appears redder. At even higher redshift when the 4000 Å break has passed the R filter (R now about constant) it enters the z filter. From this point on z decreases so that the color decreases, too.
Third test: The simulation algorithm to set up and classify the clusters is tested for one redshift (z = 1.2). Its population mix is 60% elliptical and 40% spiral galaxies, it is a cluster of Abell (Abell, 1958) richness class 0. Fig. 5.5 shows the distribution of all the cluster galaxies in the left panel. After having simulated the object catalogue with the magnitudes the multi-color classification is run which yields the photometric redshifts. The right panel in Fig. 5.5 illustrates the corresponding photometric redshift histogram for which all galaxies brighter than the R band survey limit ($R < 24.8$ mag) have been selected. Clearly evident is a peak at redshift 1.23 with a redshift scatter Δz of ∼0.07.

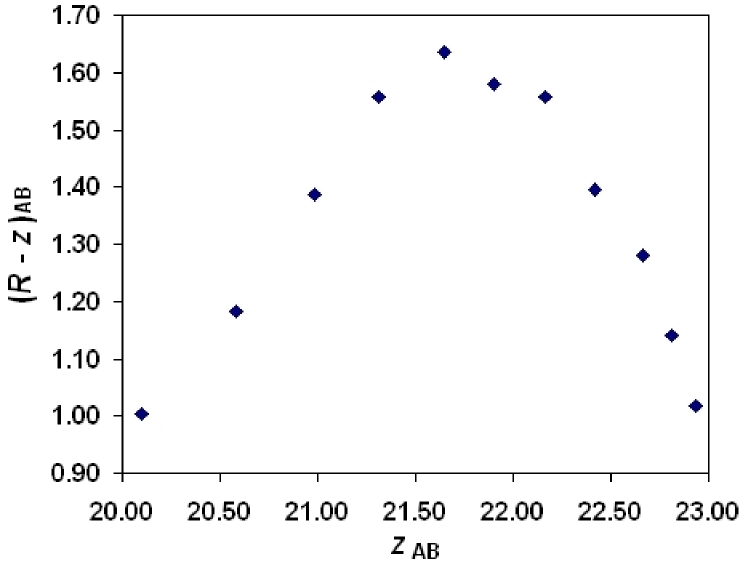

Figure 5.4: $(R-z)$-z color-magnitude diagram (AB magnitudes) in the observed frame for the early-type galaxies derived from the simulation input calculations.

The fact that the classification yields the correct redshift for most of the galaxies confirms the correct setup of the magnitudes and serves as a consistency check.
To summarize, the first three basic steps for the HIROCS simulations are set up. These can be applied in future when the HIROCS data are available and the real object catalogue can be used for the Monte-Carlo simulations.

5.2 COMBO-17

After having provided the simulation procedures for HIROCS the procedures were modified for the selection function determination in COMBO-17. In contrast to HIROCS, COMBO-17 already provides measured information like luminosity function parameters, relations for the photometric redshift scatter based on the 17-filter classification, and for the completeness as a function of the R band magnitude. With these relations at hand predictions of photometric properties as well as redshifts for any galaxy population can be made. Thus the procedure of simulating artificial clusters can be performed without the step of the multi-color classification which is necessary for HIROCS (see Sect. 5.1.3). Consequently in this case the three steps of calculating the input magnitudes, simulating

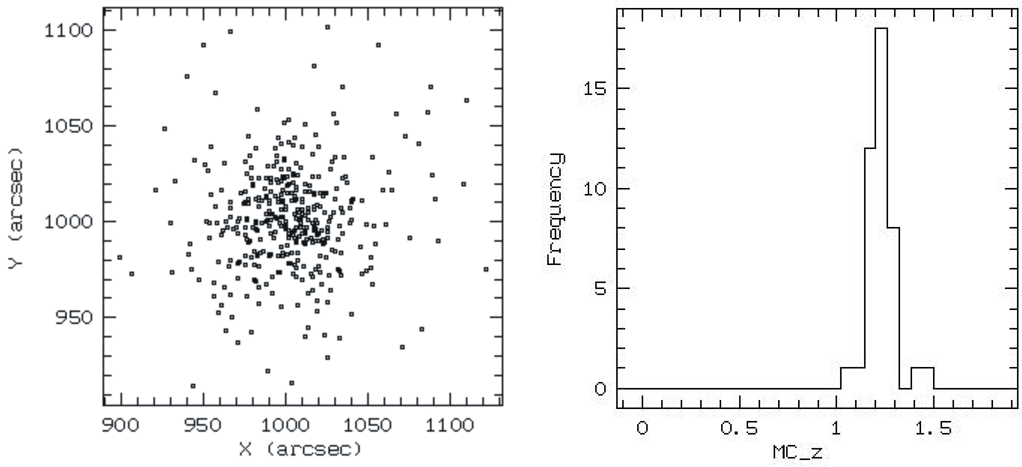

Figure 5.5: Synthetic cluster at redshift 1.2. Left: Distribution of the simulated galaxies, positions are given in arc seconds. Right: Histogram of the photometric redshifts MC_z from the multi-color classification, apparent magnitude selection: $R < 24.8$.

the galaxy clusters, and carrying out the Monte-Carlo simulations remain.
The second part of this Chapter is opened with the simulation setup for the COMBO-17 selection function. Changes compared to HIROCS are discussed therein. After that the results of the Monte-Carlo simulations are presented comprising the selection functions for the 17-filter as well as the 5-filter multi-color classification, and for a simulation where input parameters are varied. Moreover the false-discovery rate is determined for the 17-filter case.

5.2.1 Simulation setup

The luminosities for the two types of galaxies – ellipticals which represent the red-sequence population and spirals for the so-called blue-cloud – are calculated following a Schechter luminosity function (see Sect. 2.2). Faber et al. (2006) published the best-guess parameters for COMBO-17 and DEEP-2 in the rest-frame B band:

$$\alpha_{\mathrm{red}} = -0.5 \tag{5.3}$$

$$\alpha_{\mathrm{blue}} = -1.3 \tag{5.4}$$

$$\mathrm{M}^{\star}_{B,\mathrm{red}}(z) = -20.18 - 1.04z \tag{5.5}$$

$$\mathrm{M}^{\star}_{B,\mathrm{blue}}(z) = -20.09 - 1.28z \tag{5.6}$$

In the context of the cluster simulation, the normalization parameter $\phi^{\star}_{\mathrm{red}}/\phi^{\star}_{\mathrm{blue}}$ is used to control the richness. The faint-end slopes are determined for the field populations of the two galaxy types. Since the simulation shall be performed for high-density environments the slopes are adjusted for that similar to the HIROCS simulations. $\alpha_{\mathrm{red}} = -0.8$ and $\alpha_{\mathrm{blue}} = -1.6$ are plugged into the simulation procedure (Popesso et al., 2006).

For the calculation of magnitudes in the observed frame for the two populations rest-frame color-magnitude relations are needed. These relations have been presented as a function of M_V and redshift in Bell et al. (2004) and Faber et al. (2006) following the COMBO-17 analysis of red-sequence galaxies as well as the galaxies of the blue cloud, see equations 2.1 and 5.1. After the calculation of the B band magnitude at a given redshift a suitable galaxy template spectrum with the correct color given by these two relations has to be selected. At this point the COMBO-17 template library comes into play in order to find the color connecting the B band with the foreseen filter used in the cluster finding procedure. Here it is the R band because it is the deepest exposure of the survey. To summarize the apparent R band magnitudes are calculated using the definition of the magnitudes:

$$\mathrm{f}_{\mathrm{z=0}} = \frac{\mathrm{f}_{B,\mathrm{vega}}}{1 \cdot 10^{10}\,{\mathrm{D_L}}^2\,10^{-0.4\,\mathrm{M}^{\star}_B}} \tag{5.7}$$

$$R = -2.5\log\frac{\mathrm{f}_{\mathrm{z=0}}}{\mathrm{f}_{R,\mathrm{vega}}} - (B-R)_{\mathrm{kcorr}} \tag{5.8}$$

with the luminosity distance $\mathrm{D_L}$ (equation 2.4) and $\mathrm{f}_{B,\mathrm{vega}}/\mathrm{f}_{R,\mathrm{vega}}$ denotes the Vega flux in the B/R band. The color index $(B-R)_{\mathrm{kcorr}}$ incorporates the K correction.

The input photometric redshifts of the cluster galaxies are assigned with a redshift scatter following the analysis published in Wolf et al. (2004). In the 17-filter case it can be modelled as:

$$\frac{\sigma_{z,17}}{1+\mathrm{z}} \approx\; 0.007 \times \sqrt{1 + 10^{0.8(R-21.6)}} \tag{5.9}$$

Restricting the filter set to the five broad-band filters ($U\,B\,V\,R\,I$) the analysis yields:

$$\frac{\sigma_{\mathrm{z},5}}{1+\mathrm{z}} \approx\; 0.035 \times \sqrt{1 + 10^{0.8(R-23.0)}} \tag{5.10}$$

For R band magnitudes fainter than 24 these approximations are not tested and should not be used for simulation purposes. The redshift scatter is magnitude-dependent and increases for faint objects. When the magnitudes become fainter and fainter the multi-color classification also becomes more insecure so that a rising number of objects will be classified with larger errors or even no classification can be carried out. This fact is taken into account by a completeness function c_R. The following fitting results as a function of the R band magnitude for the 17-filter and the 5-filter classification are used (again Wolf et al. 2004):

$$c_{17}(R) \approx\ 1 - 10^{1.2(R-24.75)} \tag{5.11}$$

$$c_5(R) \approx\ 1 - 10^{0.6(R-24.75)} \tag{5.12}$$

These completeness estimations should not be applied for $R > 24.75$ because a negative completeness is not defined.

5.2.2 Selection function for the CDFS

Since the data in the two other COMBO-17 fields are of comparable depth and sky coverage, the simulations are only carried out for the Chandra-Deep-Field-South (CDFS). The results are analogously applicable to the A901/902 and S11 fields.

17-filter classification

For a statistically significant statement about the ability of finding a certain class of galaxy clusters, large numbers of clusters have to be simulated. Thereby the simulations should cover the relevant parameter space with a sufficiently dense grid of input parameters. In the main simulation, termed #1, the population mix is fixed to 60% elliptical and 40% spiral galaxies (van Dokkum et al., 2000). Additionally both galaxy types are distributed according to a circular King profile for simplicity. Later on a parameter-variation study is carried out to test the possible influence of these two assumptions on the recovery rate. Redshift and richness are the parameters which shall be varied within the simulation grid. The redshift range $0.3 < \mathrm{z} < 0.9$ is covered in steps of 0.1. At lower redshifts than 0.3 the foreground clusters are rather easy to find and there the extension on the sky is so large that a huge part of the whole observed field is covered by cluster galaxies which imposes a bias to the field density estimation in the cluster search procedure. The richness values $\mathrm{N_{gal}}$ are chosen such that the parameter regions are covered where the recovery rate deviates from being complete. Known real over-dense regions are avoided when the clusters are inserted to circumvent problems of alignments in redshift space and possible mixing of real and simulated cluster galaxies. The position and redshift determination of the simulated clusters in the real background is performed with the same parameter setup as for the detection of real structures.

For each parameter pair $[\mathrm{z}, \mathrm{N_{gal}}]$ a set of $\mathrm{N} = 100$ clusters is simulated, inserted into the object catalogue, and tried to be re-detected. Based on this number the application of count statistics yields errors of the recovery rate which are given by $\sqrt{\mathrm{N}}$.

The recovery rate is defined as the fraction of clusters (from the 100 input clusters) which were recovered by the search algorithm. Both their positions and their redshifts have to be recovered, the position within 200 kpc at the cluster's redshift and the redshift within $\pm 3\sigma_z$. Fig. 5.6 shows the recovery rate as a function of the richness number $\mathrm{N_{gal}}$ in the top panel and as a function of redshift in the bottom panel. The colored data points which are connected by lines are the results for the different redshift values (see the legend in this Figure). At redshifts below ∼0.5 the simulation shows that all clusters with richness $\mathrm{N_{gal}} < 20$ are expected to be found by the cluster search method. For this richness cut the recovery rate breaks more and more down towards higher redshifts with ∼80% recovery rate at redshift 0.6 and <20% at even higher redshifts. Very rich systems with $\mathrm{N_{gal}} \sim 50$ have almost complete recovery at all redshifts. The largest decrease of the recovery rate as a function of richness can be seen in the redshift range $0.5 < \mathrm{z} < 0.8$. More intuitive is the diagram where the recovery rate is plot versus the redshift. At a fixed richness the completeness can be quantified directly.

In the following a selection for recovery rates higher than 50% is deployed to focus the attention to systems which can be found reliably by the search algorithm. The pure detectability of a cluster expressed by the recovery rate is one issue but how well works the determination of the redshifts and the richness? The answer to the first question is illustrated in Fig. 5.7 which compares the original and the estimated redshifts for two richness values. Considering input redshifts below ∼0.7 the redshift estimation works very well. The error bars represent the average of the redshift scatter of the found simulated clusters and these increase towards higher redshifts. At higher redshifts there is an indication of a weak trend towards underestimating the redshifts which was already recognized in COMBO-17 before (Christian Wolf, private communication). For galaxies at these redshifts the determination of the photometric redshifts is hampered by a border effect. The template library used at that time is restricted to redshifts of 1.4 which leads to problems in the proper calculation of the redshift probability distributions. This feature may be solved when the template libraries are extended to higher redshifts and when infrared data are included in the classification. To summarize, the estimation of the redshifts for the cluster candidates is expected to work well.

The performance of the richness estimation shall be discussed by means of Fig. 5.8. For two different redshifts the plots compare the input richness $\mathrm{N_{gal,in}}$ with the estimated richness $\mathrm{N_{gal,est}}$. Error bars are calculated like this: Since the input richness scatters (see the explanation in 5.1) the contribution of this scatter to the errors of the estimated richness values has to be taken into account. To do so $\mathrm{q} = \mathrm{N_{gal,est}}/\mathrm{N_{gal,in}}$ and its standard deviation is calculated. With this the scatter of the estimated $\mathrm{N_{gal,est}}$ is determined and used for the error bars. In general, the $\mathrm{N_{gal,in}}$ errors increase with rising redshift on the one hand (from the left to the right panel) and decrease with rising richness at a given redshift.

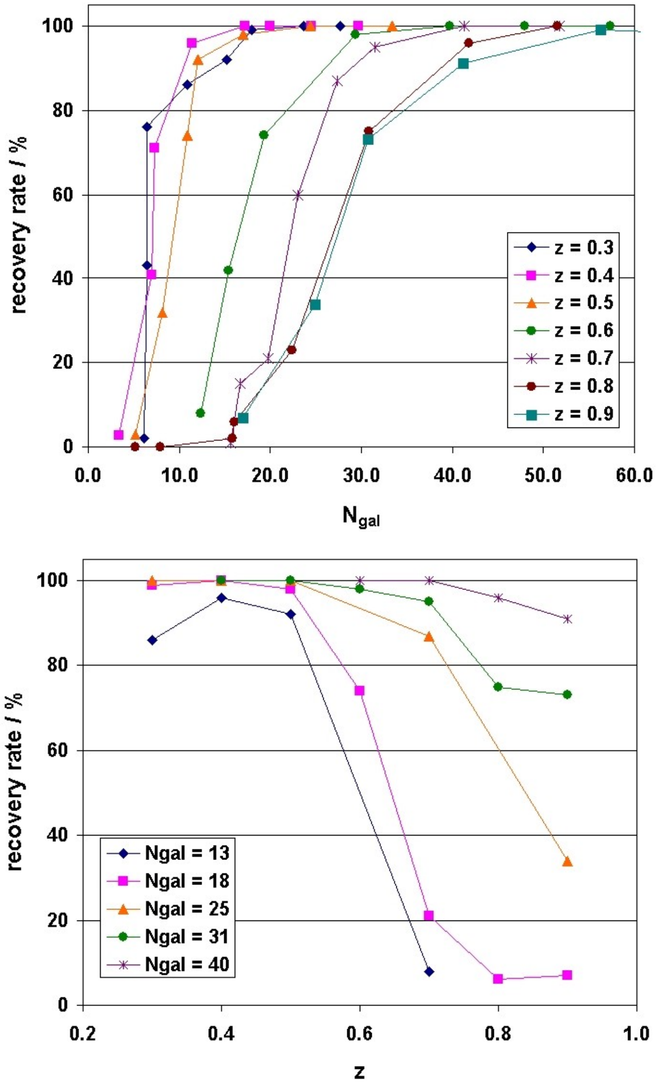

Figure 5.6: Top: Recovery rate in % versus richness $\mathrm{N_{gal}}$ for different redshifts for simulation #1. 100 clusters were simulated per richness which is given as the number of galaxies in the magnitude range $[\mathrm{M}_R^\star{-}1, \mathrm{M}_R^\star{+}2]$ ($\mathrm{M}_R^\star$ = characteristic magnitude at inspected redshift). The lines connect the data points for better visibility. Bottom: Recovery rate versus redshift for different richness values $\mathrm{N_{gal}}$.

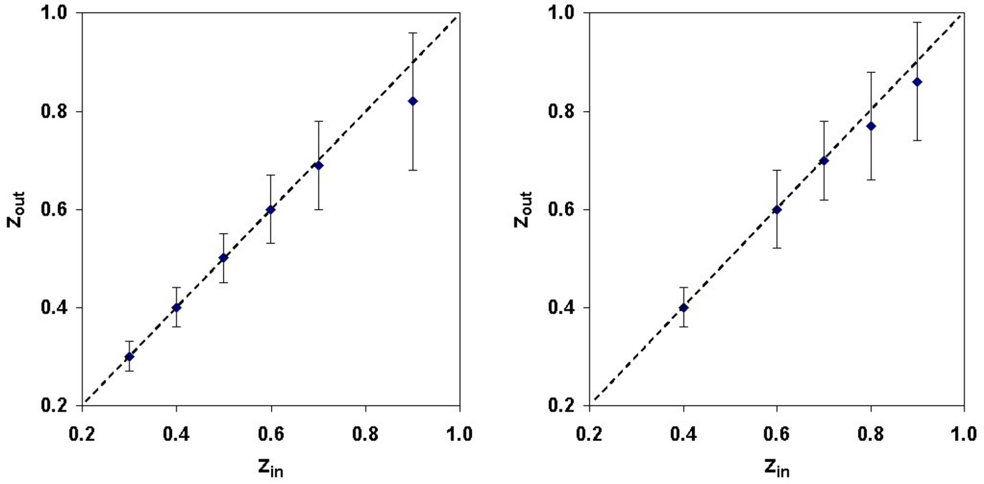

Figure 5.7: Estimated versus input redshift for two different richness values (simulation #1). Left: $N_{gal} = 18$, right: $N_{gal} = 31$. The error bars are the average values of the estimated redshift scatter for the artificial clusters found by the cluster search.

Note that the error bars are often smaller than the symbol sizes. As can be seen the estimation of the richness works very well for both redshifts. No significant systematic trend due to a possible contamination is expected based on these calculations.

False-discovery rate

The false-discovery rate gives the number of cluster detections which are not real physically associated galaxy systems in 3D space (so-called spurious clusters). This quantity is examined here to find out whether the cluster selection according to a 3σ significance level in the local galaxy density estimator is appropriate to minimize the number of false detections. Such investigations were already carried out by Kim et al. (2002) and also Goto et al. (2002).

A suitable method to quantify the false-discovery rate is to randomize the object distribution in a given object catalogue and leave the redshifts as well as the R band magnitudes unaltered. On this modified catalogue the cluster search is run and the number of identified clusters counted after selecting again $>3\sigma$ over-densities. The random positions are created with the MIDAS command CREA/RANDOM using a uniform distribution function. This first case yields no detected cluster candidate at the $>3\sigma$ significance level in local galaxy density. Another test comprises the randomization of the redshifts while

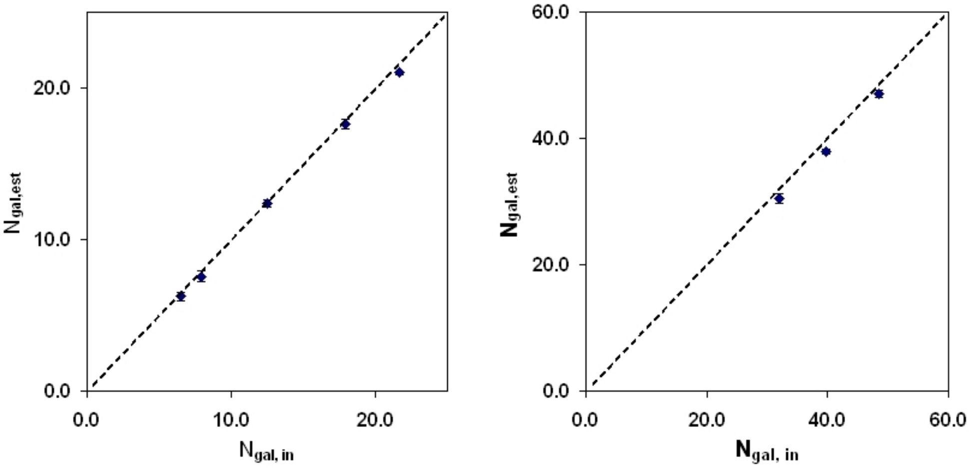

Figure 5.8: Estimated versus input richness at two different redshifts (simulation #1). Left: z = 0.4, right: z = 0.8. The error bars are the standard deviations of the estimated richness values of the artificial clusters found by the cluster search. The dashed line is the bisector where input and estimated richness are equal.

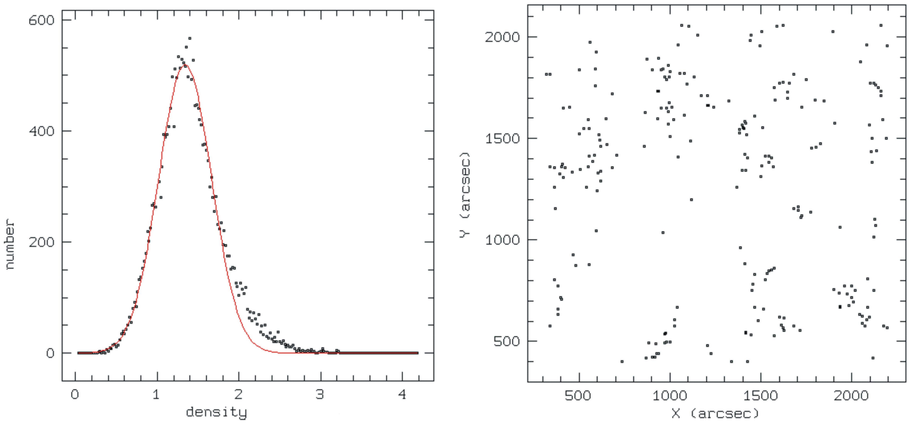

Figure 5.9: Left: Gaussian fit (red curve) to the rising flank of the density distribution. Right: [x, y] object distribution after applying the 3σ over-density selection.

the sky positions and R are not changed. All apparent clustering on the sky due to the large-scale structure maintains but redshift peaks are eliminated so that the 3D density enhancements are washed out. Again CREA/RANDOM is applied to create random redshifts in the range $0 < z < 1.2$ and their errors as a function of the R band magnitude are calculated according to equation 5.9. Fig. 5.9 illustrates the Gaussian fit to the density distribution (left panel) and the object distribution after the $>3\sigma$ over-density selection is shown in the right panel. Although there seem to be excess densities in the 2D distribution, the procedure to determine the candidates' positions as well as redshifts does not yield any galaxy enhancements in 3D space.

In conclusion, both methods to quantify the false-discovery rate described here clearly show that no spurious cluster candidates are found under the simplest assumptions of uniform distributions of either positions or redshifts. The reality cannot, of course, be described by such uniform distributions. However, this test indicates that the number of false detections is very low and the strict choice of the over-density cut is appropriate to select significant cluster candidates while minimizing the number of spurious clusters.

Comparison with 5-filter classification

The restriction of the multi-color classification to the five broad-band filters ($U\,B\,V\,R\,I$) and the comparison to the 17-filter case shall give important clues about the advantage of incorporating inter-mediate band filters like in COMBO-17 (see the more detailed discussion in Sect. 6.2). Fundamental differences can be derived for a subset of redshifts as well. Thus only $z = 0.4$ and 0.8 are considered. All other parameters are kept the same as in the main simulation #1. Concerning the photometric properties the 5-filter approximations introduced in Sect. 5.2.1 are applied.

In both redshift cases the restriction to five filters leads to a loss of sensitivity for less rich galaxy concentrations. At the lowest redshift the candidates with richness $\mathrm{N_{gal}} \sim 20$ can be recovered fully with the large and the restricted filter set. Only with lower richness values the ability to detect structures starts to differ significantly. Examining the higher redshift bin shows the same qualitative result. All clusters with $\mathrm{N_{gal}} > 70$ are identified with both filter sets, below that cut the completeness in the 5-filter case drops while in the 17-filter case it drops below $\mathrm{N_{gal}} = 48$. The 50% recovery rate is reached at $\mathrm{N_{gal}} \sim 25$ for the 17-filter classification and at $\mathrm{N_{gal}} \sim 30$ for the 5-filter classification.

When the redshift estimation is compared (see top panels in Fig. 5.11 for $\mathrm{N_{gal}} = 18$ and 31), no significant systematic trend is visible, only the redshift scatter of the estimated redshifts increases. This means that if a cluster is detected with the 5-filter classification the estimation of its redshift works well.

Fig. 5.12 shows the comparison of the input $\mathrm{N_{gal,in}}$ and the estimated richness $\mathrm{N_{gal,est}}$ for the two cases. Like in the 17-filter classification the error for $\mathrm{N_{gal}}$ decreases with rising richness. The significant difference for the 5-filter case is a systematic under-estimation

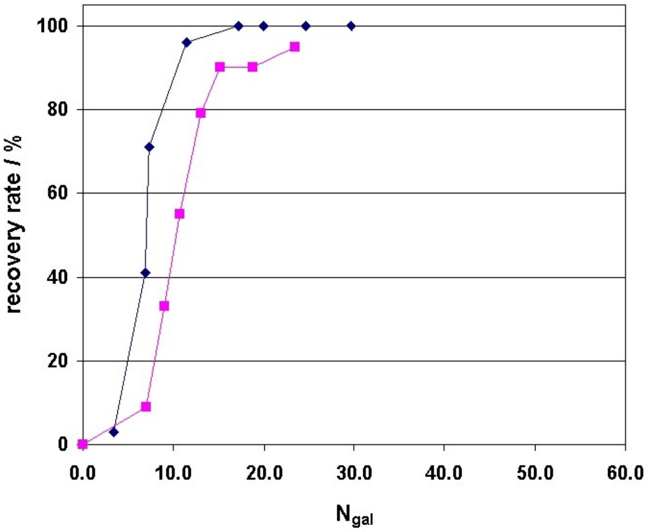

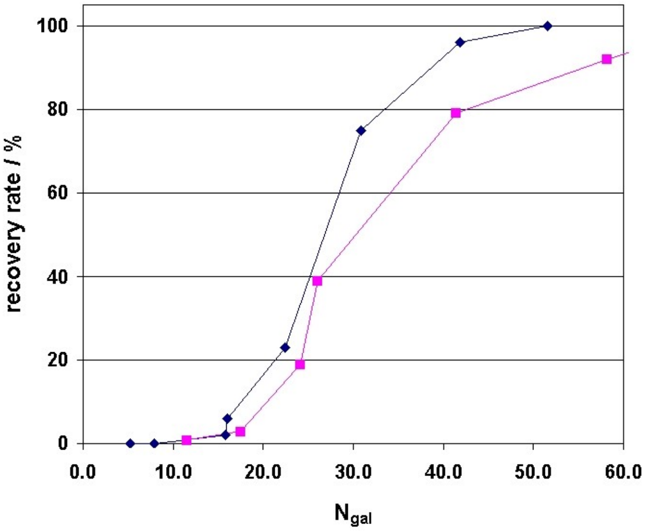

Figure 5.10: Recovery rate in % for different redshifts as a function of N_{gal} for the 17-filter (dark blue diamonds) and the 5-filter (magenta squares) classification. Top: $z = 0.4$, bottom: $z = 0.8$.

of the richness seen for both respected redshifts.
To summarize, for the classification with the five broad-band filters ($U\,B\,V\,R\,I$) the completeness of a galaxy cluster sample expressed by the recovery rate significantly decreases

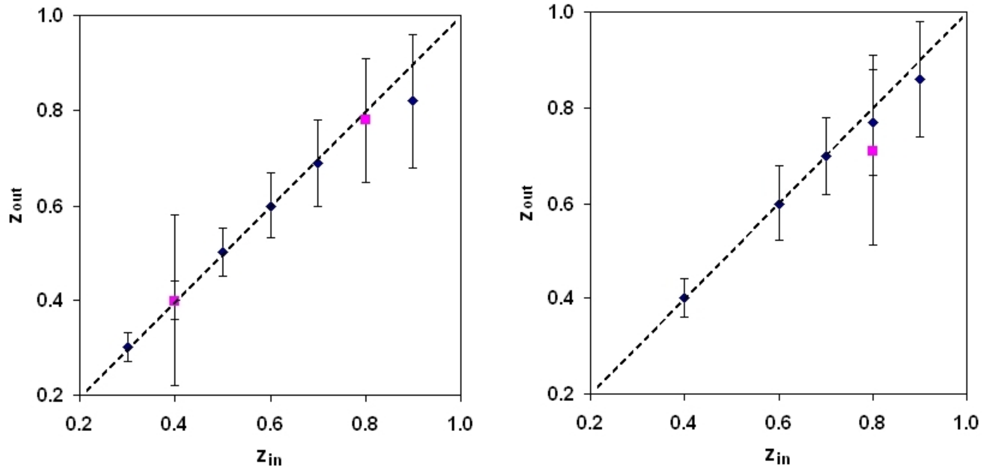

Figure 5.11: Comparison of input and estimated redshift for $N_{gal} = 18$ (left) and $N_{gal} = 31$ (right). Dark blue diamonds are for the 17-filter and magenta squares for the 5-filter classification.

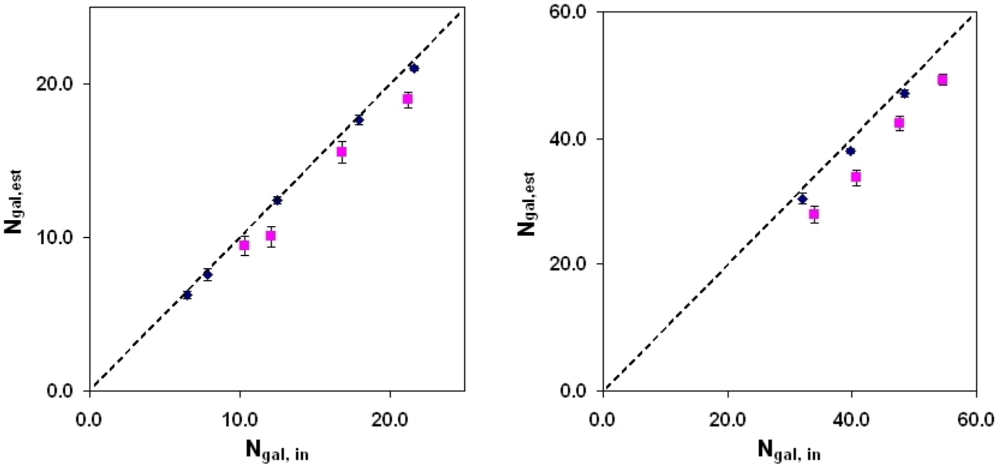

Figure 5.12: Comparison of input and estimated richness at $z = 0.4$ (left) and at $z = 0.8$ (right). Dark blue diamonds are for the 17-filter and magenta squares for the 5-filter classification.

for low richness values. Moreover the estimation of the cluster richness is systematically lower which means that the actual richness is higher. Thus the recovery rates are even worse when the richness under-estimation is taken into account.

Parameter study

Two assumptions made in the main simulation #1 were too simplifying. First, spiral galaxies show the same projected distribution as the ellipticals on the sky. Normally, the number density of the blue population increases with radial distance from the cluster center. This is part of the morphology-density relation first found by Dressler (1980). Second, the population mix is the same for all clusters.

Here a parameter study (termed simulation #2) shall examine the effects of releasing these two assumptions. For a limited range in the parameter space – redshifts 0.4 and 0.8 – two rather extreme variations were simulated at the same time. The population mix is changed to 35% elliptical and 65% spiral galaxies. Additionally, the spiral galaxies are not distributed according to a King profile anymore but are evenly distributed over 2 Mpc across the cluster. This is expected to cause a decreasing contrast compared to the background because the clusters do not show an equally large concentration towards the center as in simulation #1. The top panel in Fig. 5.13 is the comparison of the recovery rates at redshift 0.4 for the simulations #1 and #2. The change in the cluster parameters is reflected in a decrease of the recovery rate at $N_{gal} \sim 22$. At $N_{gal} \sim 18$ the recovery rate decreases by about 10% and at $N_{gal} \sim 10$ by approximately 20%. The deviation from a full recovery sets in at $N_{gal} \sim 18$ for the simulation #1 and at $N_{gal} \sim 25$ for #2. This effect is even more pronounced at $z = 0.8$: the breakdown of the recovery rate for #1 sets in at $N_{gal} \sim 50$ and at $N_{gal} \sim 60$ for #2. But at the higher redshift the decrease is even faster than at redshift 0.4. As expected the lower contrast due to the non-peaked distribution of spirals leads to decreasing recovery rates compared to the clusters of simulation #1. The overall effect is not dramatic at low redshifts although the choice of the parameters was rather radical. Thus the influences of the projected distribution of the spiral galaxies and the population mix on the cluster finding procedure are judged to be low. At the high redshift end the larger deviations are caused by increasing loss of contrast to the field galaxy distribution. Still the peak in the distribution of the ellipticals offers an important feature for the detection of galaxy over-densities. To account for the more realistic projected distribution of the spiral galaxies, the simulations for HIROCS will not assume a centrally concentrated profile for this galaxy type.

The effects on the determination of the clusters' redshifts are marginal (see Fig. 5.14). This is also valid for the redshift scatter as can be seen from this plot. In the low richness case the trend towards under-estimating redshifts can be seen again for high redshifts. The possible explanation was already discussed in the description of the results for simulation #1.

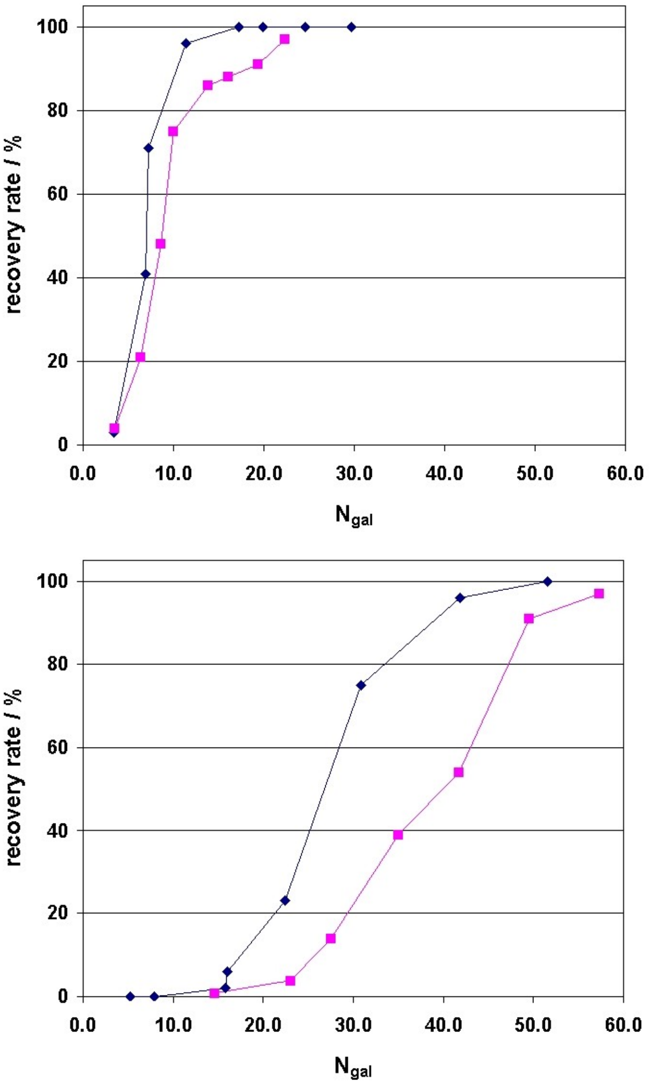

Figure 5.13: Comparison of recovery rates in % between simulation #1 (dark blue diamonds) and #2 (magenta squares) at redshift 0.4 (top) and 0.8 (bottom). The lines connect the data points for better visibility.

Similar conclusions can be drawn for the richness estimation for which two examples are displayed in Fig. 5.15 (redshifts 0.4, 0.8). At both redshifts the ability to estimate the richness is not affected by changing the properties of the simulated clusters. Only the

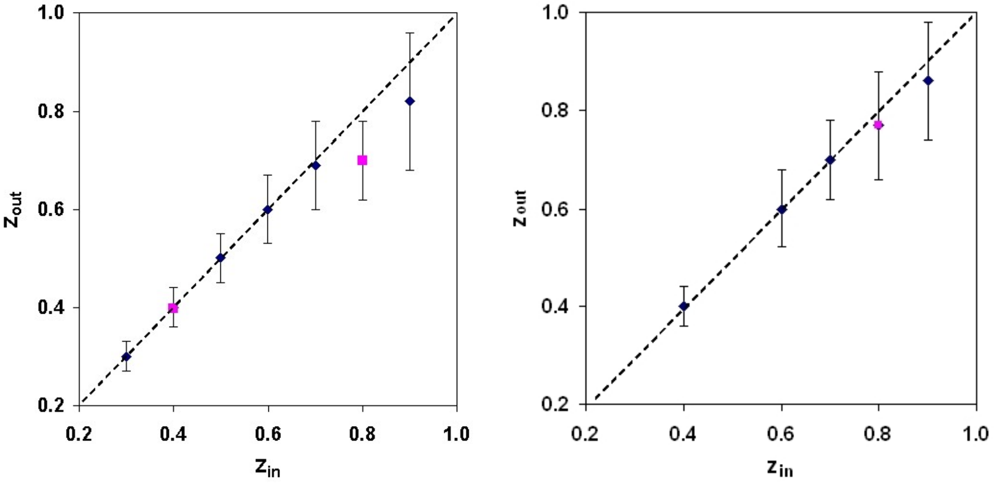

Figure 5.14: Comparison of input and estimated redshifts for the simulation #1 (dark blue diamonds) and #2 (magenta squares), left: $N_{gal} = 18$, right: $N_{gal} = 31$.

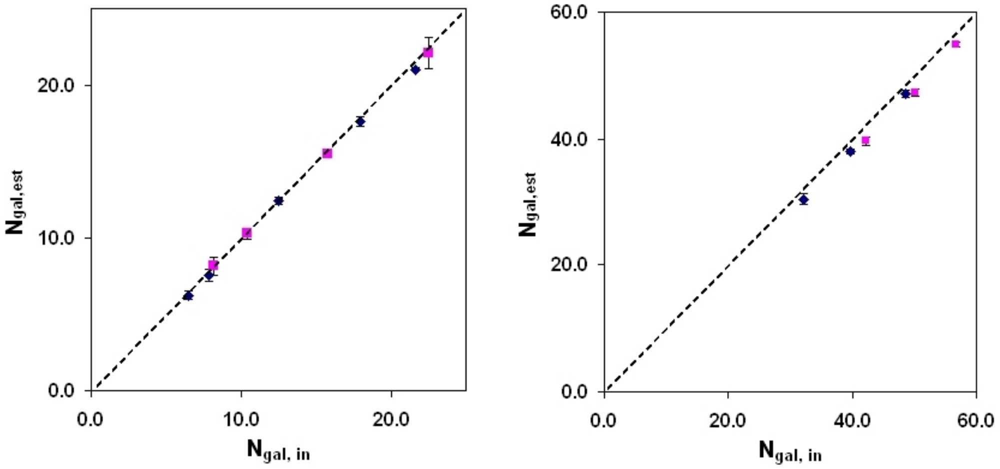

Figure 5.15: Comparison of input and estimated richness N_{gal} for the simulation #1 (dark blue diamonds) and #2 (magenta squares), left: $z = 0.4$, right: $z = 0.8$.

error bars increase slightly.

Chapter 6

Cluster finding – Results for COMBO-17

The status of HIROCS (see Sect. 3.10) did not allow to perform the cluster search for this survey. Since the basic techniques for the cluster finding along the lines described in 4.2 have been set up, a full cluster search including the determination of the selection function was done on three COMBO-17 fields. No systematic cluster search has been carried out before in this data set. Consequently, these intensively analyzed fields serve as a test ground for the search procedure. The main characteristics of the COMBO-17 survey were explained in the Introduction.

In two of the COMBO-17 fields foreground Abell galaxy clusters at redshifts below 0.2 are found. These can be clearly identified on the images by eye. Additionally, a less rich system is identified in the Chandra Deep Field South (CDFS) at the field border. The search results presented in this section focus on redshifts beyond 0.2 since there has been no systematic search carried out so far. The upper redshift limit of ∼1.1 is dictated by the filter set because the 4000 Å break is shifted into the infrared wavelength range. Due to this fact redshift determinations above ∼0.9 are increasingly inaccurate.

Using the data from the CDFS, the difference between a search using the redshifts from the full 17-filter and a 5 broadband filter ($UBVRI$) multi-color classification shall be worked out. After that the cluster candidates in the A901/A902 field are presented. For the S11 field already infrared data for the COMBO-17+4 survey extension exist. Zoltán Kovács has incorporated data in 2 filters (J, H) into the classification and analyzed these as part of his PhD thesis (Kovács, 2005). With this new classification the effects of including infrared data on the cluster search can be examined.

The cluster search is conducted like described in Sect. 4.2 with the following search parameter values: velocity limit $\beta_{\rm lim} = 6\,000\,{\rm km/s}$, circular search radius $r_{\rm lim} = 300\,{\rm kpc}$.

6.1 Chandra Deep Field South – 17 filter classification

For this search the basis is the COMBO-17 object catalogue of the CDFS for which the multi-color classification with 17 filters was carried out. After the application of the cluster finding procedure the Gaussian fit to the rising flank of the density distribution yields a 3σ over-density cut of 2.01. Fig. 6.1 illustrates the fit result. Excess counts at density values of approximately 1.7 and higher can be clearly identified.

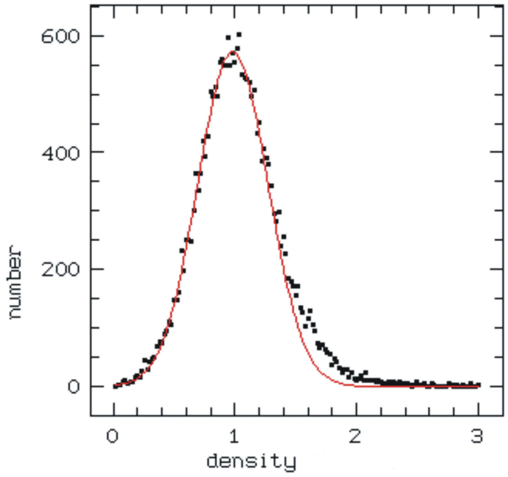

Figure 6.1: Distribution of the density estimator values (black dots) in the CDFS. The red line is the Gaussian fit to the rising flank of this distribution.

Selecting the object catalogue according to the before mentioned over-density cut enhances the contrast of the clustered structures compared to the background galaxy density (Fig. 6.2). Several agglomerations in $[\mathrm{x}, \mathrm{y}]$ are obvious and the corresponding redshift histogram reveals peaks at $\mathrm{z} \sim 0.15, 0.5$ and 0.7. The structure at the lowest redshift is a foreground cluster centered at the eastern border of the field which was missed by the Abell cluster survey. It is also not listed in the NASA/IPAC Extragalactic Database (NED[1]). Fig. 6.3 shows the possible cluster members in the deep R band stacked image of the CDFS which are marked by green squares (selected box size: $250 \times 250\,\mathrm{kpc}$ at the cluster's redshift). Note the two bright elliptical galaxies which dominate in the cluster center.

---

[1] see http://nedwww.ipac.caltech.edu/

Table 6.1: Cluster candidates at >3σ over-density in the CDFS with the position on the field in arc seconds (columns x and y), the estimated redshift z as well as its redshift scatter δz, the sky positions [RA, DEC] (columns #6, 7, 8, and 9), the estimated richness N_{gal}, and the recovery rate R_{rec} in % from the simulations at the redshift and richness of the respected cluster.

Nr	x	y	z	δz	RA	DEC	RA			DEC				N_{gal}	R_{rec}
	arcsec	arcsec			°	°	h	m	s		°	′	″		%
1	2085.5	669.2	0.54	0.05	52.8448	-27.9706	3	31	22.75	-	27	58	14	15	70
2	539.2	1556.1	0.47	0.15	53.3306	-27.7250	3	33	19.34	-	27	43	30	31	100
3	457.2	1551.9	0.43	0.07	53.3534	-27.7264	3	33	24.82	-	27	43	35	15	100
4	1703.6	1131.8	0.68	0.07	52.9652	-27.8422	3	31	51.65	-	27	50	32	27	95
5	1604.3	897.7	0.75	0.07	52.9959	-27.9074	3	31	59.02	-	27	54	27	22	40
6	991.2	1689.8	0.75	0.05	53.1890	-27.6891	3	32	45.36	-	27	41	21	27	70
7	594.4	453.7	0.36	0.05	53.3139	-28.0308	3	33	15.34	-	28	1	51	5	0

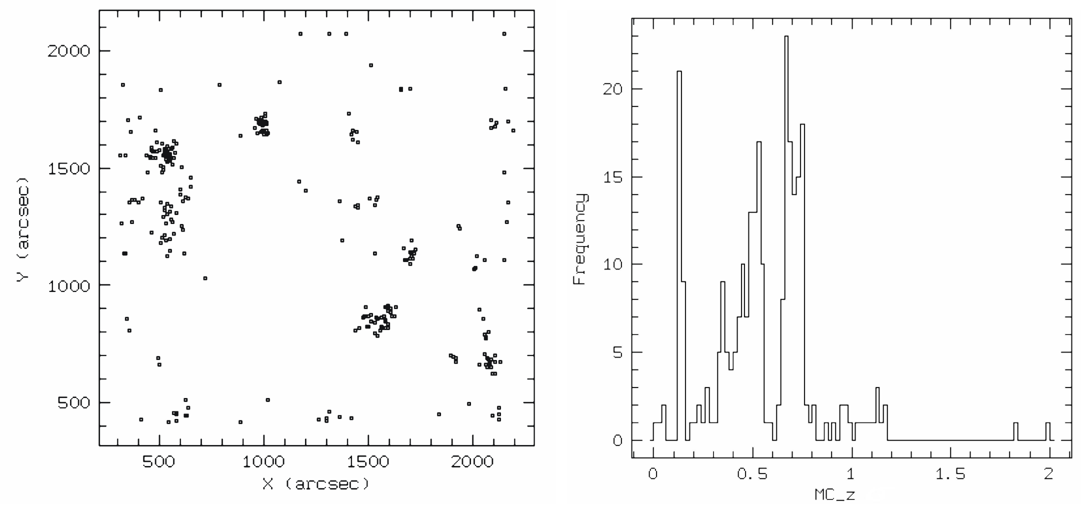

Figure 6.2: CDFS with full 17-filter classification. Left: Object distribution (Pixel coordinates [x, y] in arc seconds) after selecting for >3σ over-densities. Right: Corresponding photometric redshift (MC_z) histogram.

The automatic position – with a 40″ Gaussian smoothing which is the optimized width to find structures at redshifts beyond 0.5 – and redshift determination (see Sect. 4.2.3) gives the following results: In total seven candidates could be identified which are listed in Table 6.1. Besides the positions on the images in arc seconds as well as on the sky the estimated redshifts in concert with their scatter, and the estimated richness N_{gal} is given.

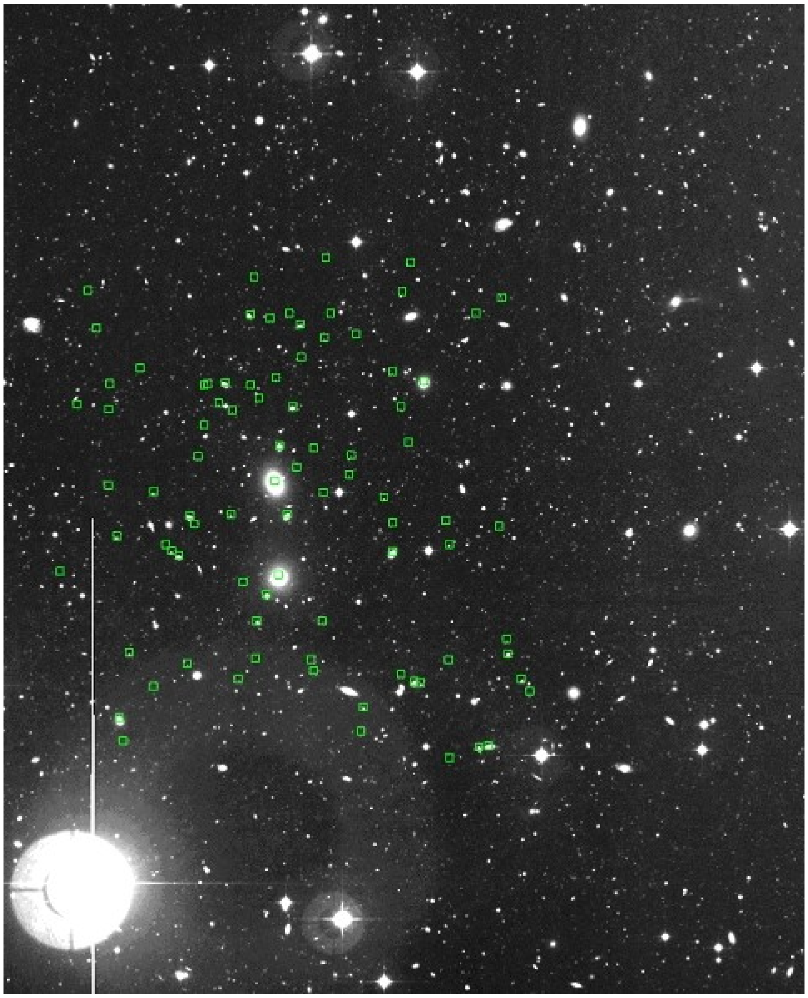

Figure 6.3: *R* band image of the foreground cluster at $\mathrm{z} \sim 0.14$. Possible cluster member galaxies are marked with small green squares. Selection: $0.125 < \mathrm{z} < 0.145$ and $[\mathrm{x}, \mathrm{y}]$ box with $\sim$250 kpc around the cluster center.

Additionally, the recovery rate $\mathrm{R}_{\mathrm{rec}}$ is listed which was estimated from the simulations for the redshift and the richness of the respected candidate. For the stacking analysis, presented in Sect. 8.2, only candidates should be considered which are judged to be significant on the basis of the recovery rates. Therefore candidates are selected for which the recovery rate at $[\mathrm{z}, \mathrm{N}_{\mathrm{gal}}]$ in the simulations is higher than 50%. From the table five clusters fulfil this selection criterion, namely candidates #1, 2, 3, 4, and 6.

6.2 CDFS – Comparison with 5 filter classification

Here the over-density cut is found to be 2.13 and applied to select the object catalogue. The galaxy distribution and the redshift histogram are displayed in Fig. 6.4. Comparing the [x, y] distributions from this Figure with that from the 17-filter classification (Fig. 6.2) some differences become apparent. Some new seemingly dense regions come up, e.g. at [x, y] ∼ [550, 1950]. The comparison of both redshift histograms reveals the main problem for the finding, when only the five broad filters are used, more clearly. The three main redshift peaks which are visible in Fig. 6.2 smear out and are shifted to higher redshifts. From this first impression the expectation that less filters lead to less accurate photometric redshifts and thus to the loss of detectability of groups/clusters is confirmed. To quantify this more in more detail, Table 6.2 shows the results from the determination of the candidates' positions as well as redshifts. Three candidates could be identified with the 5-filter multi-color classification. Only the richest and most-peaked candidates #1, 2, and 6 are found, too. The two candidates #4 and #5 which are also rather rich were missed because their object distribution is too loose and the redshift peak is washed out. For the cluster search it is essential to have accurate photometric redshift determinations which are possible by the inclusion of medium-band filters for the COMBO-17 survey. This effect can be seen when the redshift distribution after the 3σ over-density cut of the

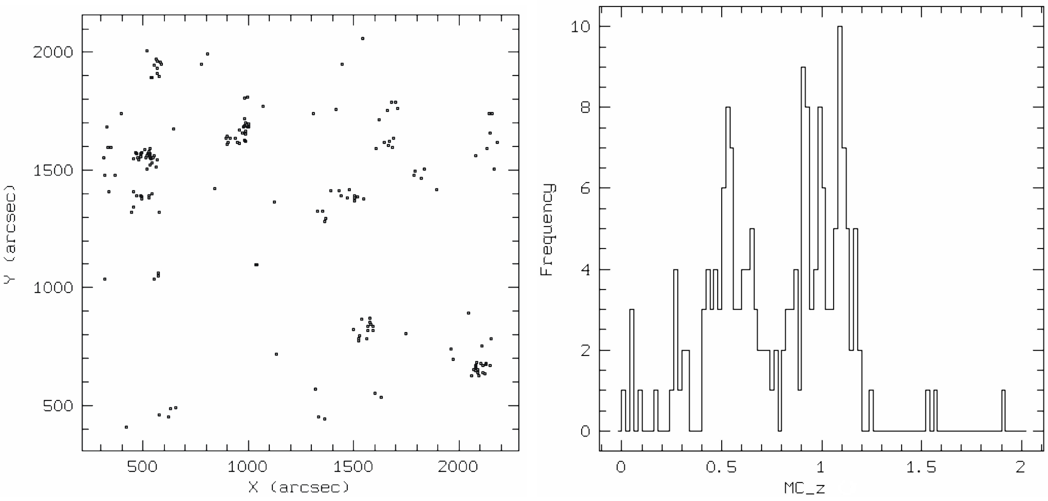

Figure 6.4: CDFS with 5-filter classification. Left: Object distribution (Pixel coordinates [x, y] in arc seconds) after selecting for $>3\sigma$ over-densities. Right: Corresponding photometric redshift (MC_z) histogram.

Table 6.2: Comparison of cluster candidates at $>3\sigma$ over-density in the field CDFS from the 17-filter and the 5-filter multi-color classification. Shown are the $[\mathrm{x}, \mathrm{y}]$ positions, the estimated redshift z as well as its redshift scatter δz, the estimated richness $\mathrm{N}_{\mathrm{gal}}$, and the recovery rate $\mathrm{R}_{\mathrm{rec}}$ in % (only for 17-filter case) from the simulations at the redshift and richness of the respected cluster. The empty spaces indicate that no candidate could be found for the 5-filter case.

17 filter							**5 filter**				
Nr	**x**	**y**	**z**	**δz**	**N_{gal}**	**R_{rec}**	**x**	**y**	**z**	**δz**	**N_{gal}**
	arcsec	arcsec				%	arcsec	arcsec			
1	2085.5	669.2	0.54	0.05	15	70	2092.6	656.0	0.53	0.07	25
2	539.2	1556.1	0.47	0.15	31	100	522.1	1560.4	0.55	0.29	50
3	457.2	1551.9	0.43	0.07	15	100					
4	1703.6	1131.8	0.68	0.07	27	95					
5	1604.3	897.7	0.75	0.07	22	40					
6	991.2	1689.8	0.75	0.05	27	70	989.7	1686.7	0.69	0.17	44
7	594.4	453.7	0.36	0.05	5	0					

5-filter case is compared with that of the 17-filter case. Clearly the peaks found in the latter cannot be found in the former. But even worse the redshift distribution is focussed at redshift ∼0.5 and ∼1.0. Consequently, wrong redshift estimations for cluster candidates caused by these focussing effects could deteriorate the quality of a cluster catalogue produced on the basis of such a filter set. The depth of the broadband data was not set up for the cluster finding purpose. Such an effect is not expected for the HIROCS filter set because the observational setup is specialized to the cluster finding.

6.3 A901/A902

The cluster finding procedure has been carried out with the same parameters as for the CDFS. Fitting the rising flank of the density distribution with a Gaussian yields a 3σ over-density cut of 1.85. Fig. 6.5 to the left shows the distribution of galaxies and the redshift histogram after selecting the object catalogue following this cut. The large agglomeration of objects at $[\mathrm{x}, \mathrm{y}] \sim [1100, 1500]/[1350, 1450]$ is the cluster system A901a/A901b at a redshift of $\mathrm{z} = 0.165 \pm 0.005$. Below that region at $[\mathrm{x}, \mathrm{y}] \sim [1050, 800]$ the cluster A902 is found at the same redshift and builds together with A901 the super-cluster A901/A902. This system of galaxy clusters is clearly apparent in the redshift distribution (Fig. 6.5, right) as the dominant peak at the lowest redshifts. A fourth neighboring less rich cluster can be seen at $[\mathrm{x}, \mathrm{y}] \sim [1900, 700]$. Although the cluster search parameters were not tuned to find the foreground clusters at low redshift, the algorithm is still able to identify the

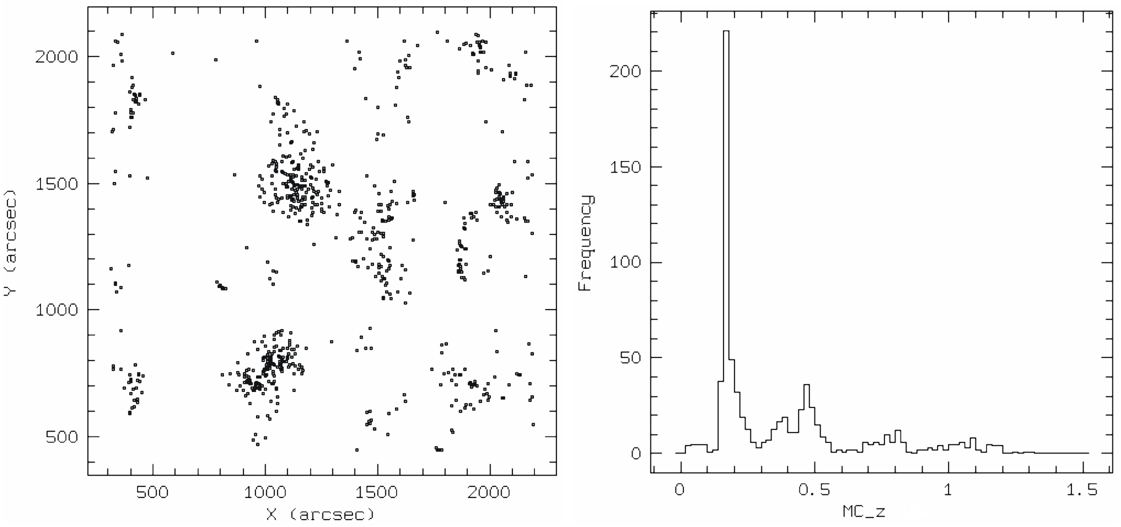

Figure 6.5: Left: Object distribution (Pixel coordinates [x, y] in arc seconds) in the field A901/A902 after selecting for $>3\sigma$ over-densities. Right: Corresponding photometric redshift (MC_z) histogram.

cores of these clusters.

The background galaxy groups and clusters at higher redshifts can not be found as easy by eye. One rather rich system has been identified in the background of the A902 cluster almost at the same [x, y] position south-east of the two dominant elliptical galaxies in a weak lensing analysis by Taylor et al. (2004) (see Sect. 8.4). It has a redshift of ∼0.48 which is clearly visible as a peak in the redshift histogram (Fig. 6.5, right). Furthermore, this cluster shows an elongated galaxy distribution and it contains a central cD galaxy.

These are the known structures in this field. The automatic finding yields the following new group/cluster candidates. For this the position determination is carried out with a FWHM of 40″ for the Gaussian smoothing. In total twelve candidates could be identified which are listed in Table 6.3 (same columns as in Table 6.1). In terms of its high redshift of ∼0.8 and its high estimated richness $N_{gal} \sim 37$ candidate Nr 1 is the most interesting cluster found in this field. Additionally, the recovery rate from the simulations for $[z, N_{gal}]$ indicates this cluster to be significant. More details are examined in the following analysis in Sect. 8.1. Selecting all clusters with associated recovery rates of larger than 50% and leaving the candidate at redshift 0.34 seven candidates can be kept as significant detections for the stacking study in Sect. 8.2. Three additional structures in the neighborhood of the cluster found in the weak lensing study of Taylor et al. at redshift 0.48 (here cluster Nr 4)

Table 6.3: Cluster candidates at >3σ over-density in the field A901/A902 with the position on the field in arc seconds (columns x and y), the estimated redshift z as well as its redshift scatter δz, the sky positions [RA, DEC] (columns #6, 7, 8, and 9), the estimated richness $\mathrm{N_{gal}}$, and the recovery rate $\mathrm{R_{rec}}$ in % from the simulations at the redshift and richness of the respected cluster.

Nr	x	y	z	δz	RA	DEC	RA			DEC				$\mathrm{N_{gal}}$	$\mathrm{R_{rec}}$
	arcsec	arcsec			°	°	h	m	s		°	′	″		%
1	2045.6	1438.8	0.80	0.05	148.850	-9.973	9	55	24.00	-	9	58	24	37	85
2	1122.0	1497.3	0.26	0.19	149.109	-9.959	9	56	26.16	-	9	57	32	3	-
3	1870.5	1161.1	0.71	0.03	148.899	-10.051	9	55	35.76	-	10	3	2	23	50
4	942.7	708.6	0.47	0.01	149.160	-10.176	9	56	38.40	-	10	10	34	17	100
5	1923.7	708.2	0.47	0.05	148.884	-10.176	9	55	32.16	-	10	10	35	13	95
6	1875.8	1249.0	0.42	0.03	148.897	-10.026	9	55	35.28	-	10	1	34	12	95
7	412.0	704.3	0.40	0.01	149.311	-10.177	9	57	14.64	-	10	10	38	8	75
8	1944.8	2031.5	0.46	0.09	148.878	-9.809	9	55	30.72	-	9	48	31	27	100
9	2098.0	1926.1	0.50	0.01	148.835	-9.838	9	55	20.40	-	9	50	17	5	0
10	803.1	1093.0	0.48	0.01	149.200	-10.070	9	56	48.00	-	10	4	10	5	0
11	414.9	1819.7	0.34	0.09	149.309	-9.867	9	57	14.16	-	9	52	3	23	100
12	1063.7	1802.0	1.03	0.13	149.126	-9.873	9	56	30.24	-	9	52	23	52	-

may form a large-scale structure feature at this redshift. One of the three structures, candidates Nr 8 and 9, is found close to a bright star in the field and could belong to one and the same system. The bright star has a large straylight halo which could eventually disturb the photometric measurements and thus objects in the background may not be measured. Consequently this candidate could be split into two components, namely Nr 8 and 9. Another high redshift candidate is Nr 3 at redshift 0.71. From this analysis the A901/A902 field is the richest field of the three COMBO-17 fields analyzed in this study.

6.4 S11 with 17 filters

For the S11 field the 3σ over-density is determined to be 1.91. Selecting the object catalogue according to such over-densities yields the object distribution and redshift histogram shown in Fig. 6.6. The top left panel is the [x, y] distribution for all redshifts in the catalogue. At [x, y] $\sim$ [750, 1150] a rich extended agglomeration of galaxies with high estimated local densities dominates the plot. This is the foreground galaxy cluster A1364 at [RA, DEC] = [$11^h43^m39.6^s$, $-01°45'39''$] at a redshift of 0.1058 (Struble & Rood, 1999). It is a rich cluster with Abell richness class 1 (more than 50 cluster members according to the definition given in Sect. 4.2.4) and has a sky extension of about 50′. Due to this

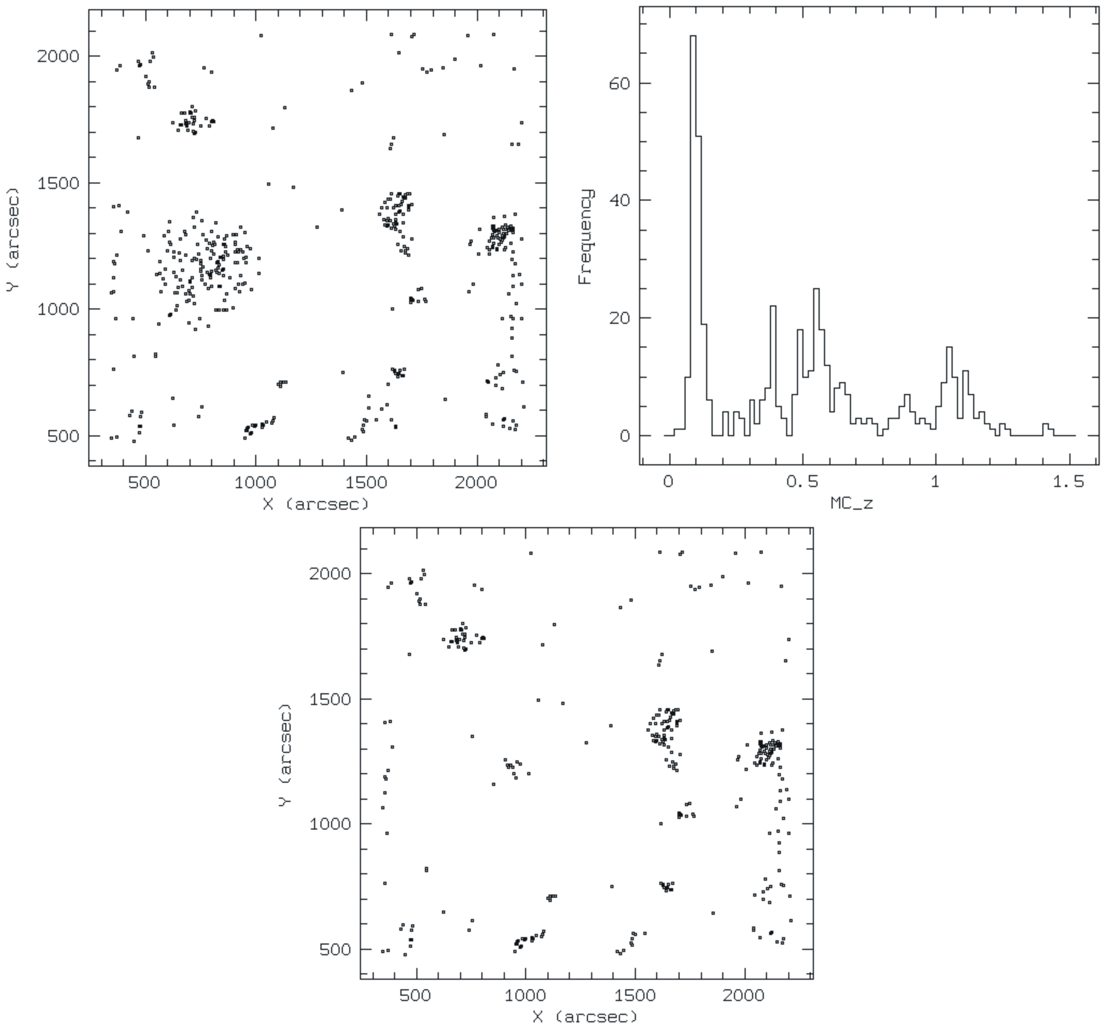

Figure 6.6: Top left: Object distribution (Pixel coordinates [x, y] in arc seconds) in the field S11 after selecting for >3σ over-densities. Top right: Corresponding photometric redshift (MC_z) histogram. Bottom: Object distribution after selecting >3σ over-densities and redshifts larger than 0.2 to remove foreground cluster.

large extension the search algorithm which was tuned for a search at higher redshifts assigns high density values only for the galaxies in the central region of the cluster. The top right panel in Fig. 6.6 illustrates the redshift distribution with the most prominent peak belonging to the Abell cluster. Several other peaks at higher redshifts already indi-

Table 6.4: Cluster candidates at >3σ over-density in the field S11 with the position on the field in arc seconds (columns x and y), the estimated redshift z as well as its redshift scatter δz, the sky positions [RA, DEC] (columns #6, 7, 8, and 9), the estimated richness N_{gal}, and the recovery rate R_{rec} in % from the simulations at the redshift and richness of the respected cluster.

Nr	x	y	z	δz	RA	DEC	RA			DEC				N_{gal}	R_{rec}
	arcsec	arcsec			°	°	h	m	s		°	′	″		%
1	694.2	1742.7	0.65	0.01	175.9020	-1.5732	11	43	36.48	-	1	34	24	7	0
2	1613.5	1334.1	0.57	0.07	175.6460	-1.6871	11	42	35.04	-	1	41	13	40	100
3	2096.6	1299.7	0.49	0.01	175.5180	-1.6935	11	42	4.32	-	1	41	36	8	20
4	1670.4	1445.8	0.57	0.03	175.6310	-1.6561	11	42	31.44	-	1	39	22	27	100
5	1642.7	749.7	0.88	0.07	175.6380	-1.8492	11	42	33.12	-	1	50	57	36	85
6	1723.3	1043.9	0.50	0.01	175.6160	-1.7676	11	42	27.84	-	1	46	3	6	5
7	1115.4	706.7	1.04	0.11	175.7860	-1.8608	11	43	8.64	-	1	51	39	30	-
8	994.6	532.6	1.05	0.17	175.8180	-1.9093	11	43	16.32	-	1	54	33	47	-

cate the presence of additional structures. If redshifts below 0.2 are excluded, the object distribution of the possible background candidates becomes clearer (bottom panel in the Fig. 6.6).

Table 6.4 lists all the cluster candidates (same columns as for the other fields) for which a 3D over-density was identified by the position and redshift estimation procedure. The recovery rate R_{rec} for the parameter pair [z, N_{gal}] from the simulations shown in the rightmost column cannot be estimated for the foreground cluster and the structures at redshifts larger than unity because no simulations were carried out there. Selecting candidates with associated R_{rec} larger than 50% three structures remain. One very interesting object due to its high redshift is the one at redshift 0.88 which appears to have a rather high richness. Interestingly, another significant candidate at redshift 0.57 is detected as a double structure. Both have high estimated richness values which may be an over-estimation. If two candidates are so close the procedure to estimate the richness will count members of the single candidates twice which leads to the over-estimation. Detections Nr 6, 7, and 8 were obtained with a Gaussian smoothing width of 68 arc seconds which is tuned for low redshifts around 0.4 where the apparent size is larger. The possible cluster candidates Nr 7 and 8 have high redshift and richness estimations. These were not found with the 40 arc second FWHM. For this high redshift 68 arc seconds is possibly too large and thus the detection is questionable. Since the simulations were carried out at lower redshifts the recovery rate cannot be given for these. The comparison with the 17+2 filter search will yield more information about these two candidates.

6.5 S11 with 17+2 filters

In the following the effect of including infrared data in the J and the H band shall be examined. These additional data have been added to the COMBO-17 data set by Zoltán Kovács (Kovács, 2005) as part of the COMBO-17+4 survey. Thereby three quadrants of the S11 field were covered with OMEGA2000 while the data in the individual quadrants have slightly different depths. Photometric redshifts were determined by a multi-color classification using 17+2 filters where a modified galaxy template library extending to redshifts of 2.0 was used. For the following analysis the object catalogue was selected for objects brighter than the 5σ limiting magnitudes in the R and the H band, which are $R < 25.8$ mag and $H < 21.5$ mag, respectively. The H band limit is shallower relative to the very deep R band exposure. Resulting from this the combined R and H band selection yields only about one fourth of the number of objects than with a pure R band selection. Thus the number counts for the cluster search are much lower and the over-densities do not appear as prominent. Because of the different H band depths of the quadrants and due to the geometry, the cluster search as well as the determination of the 3σ over-density level was done on each quadrant separately. The 3σ confidence level is calculated to be 2.92.

Table 6.5 shows the results of the comparison. Listed are the coordinates, redshifts with scatters, and the estimated richness values. The column "quad" indicates the quadrant where the candidate was found. Candidate Nr 1 was found in the quadrant which was not covered yet by OMEGA 2000. The other cluster candidates Nr 2 to 8 are discussed in the following:

- Candidates Nr 2 and 4:
  Both neighboring structures at redshift 0.57 are also identified in the 17+2 filter case. The redshifts are confirmed within the redshift scatter δz and there are some small positional offsets. As stated before the richness estimation for such neighboring objects is difficult. Therefore the given values have a large uncertainty.

- Candidate Nr 3:
  The redshift is confirmed for this candidate, the same is true for the richness.

- Candidate Nr 5:
  This structure at redshift 0.88 is also confirmed within the redshift scatter found in the 17 filter case.

- Candidate Nr 6:
  This candidate is not found at the $>3\sigma$ over-density level in the 17+2 case. The

Table 6.5: Comparison of cluster candidates at $>3\sigma$ over-density in the field S11 from the 17-filter and the 17+2-filter multi-color classification. Shown are the $[\mathrm{x}, \mathrm{y}]$ positions, the estimated redshift z as well as its redshift scatter δz, and the estimated richness $\mathrm{N}_{\mathrm{gal}}$. The empty spaces indicate that no candidate could be found.

17 filter						**17+2 filter**					
Nr	**x**	**y**	**z**	**δz**	**$\mathrm{N}_{\mathrm{gal}}$**	**x**	**y**	**z**	**δz**	**$\mathrm{N}_{\mathrm{gal}}$**	**Quad**
	arcsec	arcsec				arcsec	arcsec				
1	694.2	1742.7	0.65	0.01	7						1
2	1613.5	1334.1	0.57	0.07	40	1631.7	1328.7	0.56	0.07	36	2
3	2096.6	1299.7	0.49	0.01	8	2079.3	1315.7	0.49	0.01	7	2
4	1670.4	1445.8	0.57	0.03	27	1653.0	1422.6	0.56	0.01	10	2
5	1642.7	749.7	0.88	0.07	36	1649.7	749.5	0.87	0.05	22	4
6	1723.3	1043.9	0.50	0.01	6						4
7	1115.4	706.7	1.04	0.11	30						3
8	994.6	532.6	1.05	0.17	47	979.9	522.8	1.09	0.07	10	3
9						765.5	583.9	0.72	0.01	3	3
10						1569.8	1700.3	0.40	0.05	13	2
11						1622.5	1667.1	0.39	0.03	10	2
12						553.7	747.7	1.34	0.19	9	3

reason is that the search is done on the three quadrants separately. Structures with low richness at the border between two quadrants like this one cannot be recognized.

- Candidate Nr 7:
  Found at a redshift of 1.04 this structure is not detected at the $>3\sigma$ level. It was detected with the 17 filter classification using a large Gaussian width of 68 arc seconds. Therefore and due to its redshift which is close to the survey boundary at $\sim$1.1 its detection was endued with a question mark. The non-detection with 17+2 filters confirms this candidate to be spurious.

- Candidate Nr 8:
  In contrast to the high-redshift candidate Nr 7 this one at redshift 1.05 is detected on the basis of the 17+2 multi-color classification. With a small positional offset the redshift is confirmed within the redshift scatter δz. The high richness estimated in the 17 filter case was due to the large δz. With the additional infrared filters the redshift estimation is improved such that the scatter is significantly lower in this case.

In addition to the eight cluster candidates found with the 17 filter classification four more structures were detected with the inclusion of infrared data. The following list discusses these identifications:

- Candidate Nr 9:
  At an estimated redshift of 0.72 the richness of this candidate is very low. In the 17 filter case it could not even be detected at lower over-density levels. The low estimated richness and the non-detection in the 17 filter classification indicates that this candidate may be a spurious detection.

- Candidates Nr 10 and 11:
  These are two neighboring candidates at redshift ∼0.4 which were not found using the 17 filter classification, even for lower over-density levels these were not detected. The reason for that is unclear and a more detailed investigation of the 17-filter multi-color classification is needed which is beyond the scope of this thesis.

- Candidate Nr 12:
  This candidate is the most interesting detection considering the very high estimated redshift of 1.34. With the depth of the data in the COMBO-17 filters and the fact that these are covering only wavelengths below 10 000 Å the classification without infrared filters does not work for such high redshifts. The distribution of the over-dense galaxies is not concentrated, see Fig. 6.7 at $[x, y] \sim [550, 750]$. Furthermore, the redshift scatter δz of the galaxies is rather high. These two facts in combination with the low estimated richness of $N_{gal} = 9$ do not indicate the presence of a rich galaxy cluster. It could even be that this is a spurious detection. A simulation to determine the selection function would help to clarify the situation, but this is beyond the scope of this thesis. Taking into account the selection of the object catalogue according to the H band limit which lead to a decrease of ∼75% in the object number the low number density at these high redshifts could also be a problem. Within a redshift range of $1.28 < z < 1.40$ the total number of galaxies in the quadrant is 70. At over-density $> 3\sigma$ there are 7 galaxies within a small area of $2.3' \times 0.8'$ which corresponds to $\sim 1100 \times 390$ kpc at redshift 1.34. This estimate illustrates the approximate significance of this candidate. The infrared data collection for COMBO-17+4 in this field is not yet complete. The incorporation of these infrared data will help decide on this candidate.

To visualize the findings listed before Fig. 6.7 shows the object distribution after selecting for $>3\sigma$ over-densities from the 17+2 filter search (small black dots). Also marked are the candidates found on the basis of the 17 filter (reds crosses), and the candidates when the infrared data are included (large blue and green rings).
The sizes of the COMBO-17 fields are small and thus no large numbers of clusters up

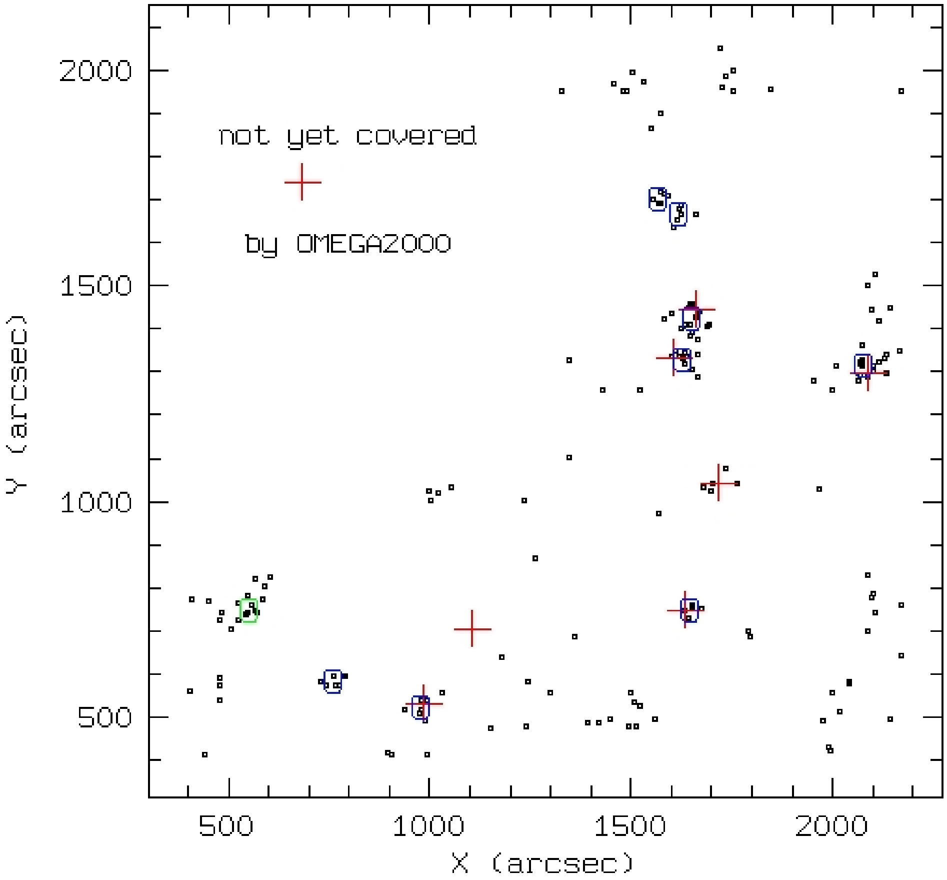

Figure 6.7: Object distribution in the field S11 for the 17+2 multi-color classification after selecting for $>3\sigma$ over-densities (black dots). The red crosses mark the positions of the cluster candidates found in the 17 filter case. Dark blue rings are those from the 17+2 cluster candidates at redshifts below 1.0 while the green ring is the one at redshift 1.34. The upper left quadrant is not yet covered with OMEGA2000 infrared observations.

to redshifts of 1.0 are found therein. At even higher redshifts, near infrared data are necessary which is available only for the S11 field yet. As the candidate Nr 12 in this field which – if it is confirmed – is not a rich cluster based on the available data set shows, there are no rich galaxy clusters detected at redshifts beyond unity. Therefore larger areas have to be covered to yield more high redshift clusters (see Sect. 2.1). HIROCS is designed to provide a suitable data set with its deep observations in five filters on 11 square degrees.

Chapter 7

Cluster finding – Comparison with Voronoi tessellation

Various cluster finding techniques in optical extra-galactic surveys were deployed in the past. The most important methods were shortly explained in the Introduction. All of these have their advantages and also disadvantages. For HIROCS a new search algorithm (see Sect. 4.2) was developed which takes advantage of the photometric redshifts derived by the multi-color classification. In general, the comparison of the search results from different finding techniques can give valuable information about strengths and weaknesses of the underlying method. As a first step, a comparison with the so-called Voronoi tessellation technique has been carried out. The search was done on the CDFS observed by COMBO-17. Ramella et al. (2001) applied the Voronoi tessellation to search for galaxy clusters and provide the code to the public. It is based on the 2D galaxy distribution and was chosen for the comparison study.

In the first section the finding scheme is described. For the selection of the cluster candidates suitable cut-off values for the search parameters have to be fixed. This is explained in the second part. The third section presents the cluster candidates in the CDFS found by this technique. After that the effect of including redshifts is discussed. At the end of this Chapter the comparison of the search results from the original as well as modified Voronoi tessellation and the search algorithm developed for HIROCS (abbreviated 3D search or method throughout this Chapter) are presented.

7.1 Finding scheme

A more detailed description of the principles can be found in Christine Botzler's PhD thesis (2004). Here only a short outline of the scheme shall be given. The Voronoi tessellation of a given set of nuclei in 2D or 3D space – for the purpose of cluster finding each nucleus corresponds to a galaxy – is a unique partition into convex cells where these cells harbor only one nucleus. An example for such a partition can be seen in Fig. 7.1 which illustrates the characteristic that the closer the nuclei (or galaxies) are the smaller the area of the surrounding convex cells is. This fact gives the procedure its power when the inverse of the cell area is used as a local galaxy density estimator. In other words, strongly clustered objects have very small Voronoi cells. The selection of over-dense structures by using the Voronoi tessellation has the advantage of being completely non-parametric in determining local densities. Other search methods like the matched-filter approach (Postman et al.,

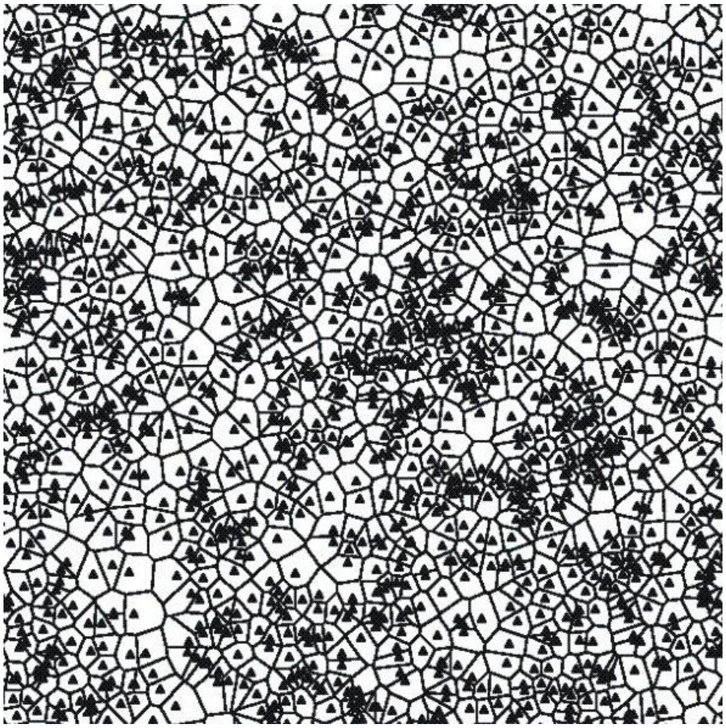

Figure 7.1: Illustration of the Voronoi tessellation on a sub-image of the CDFS: the black triangles are the nuclei corresponding to the galaxies and the lines delimit the convex Voronoi cells. In this case the boundary of the field where the cells are not closed cannot be seen.

1996) often rely on the assumption of one or several parameters to estimate the galaxy density. This of course leads to a bias towards finding clusters with certain characteristics which are similar to the model assumptions. The Voronoi technique is sensitive to any asymmetric structures not only to circular/spherical systems. Moreover the code is fast in terms of CPU time. The determination of key parameters can be carried out afterwards which is explained in the following part.
Anyway disadvantages of this technique are the following: It suffers from edge effects which means that at the field borders the tessellation fails and no closed Voronoi cells can be assigned there. Consequently, area for the search is lost at the border. Additionally the data sets have to be continuous in terms of photometric depth and sufficiently dense. These prerequisites, however, are met by the COMBO-17 data.

7.2 Parameter setup

The selection of cluster candidates is based on the calculation of densities with the help of the Voronoi cell area. Two different criteria serve to separate significant cluster candidates. The first follows the assumption that the galaxies are randomly distributed according to a Poissonian distribution function. Kiang (1966) found a description for the distribution function of the cell area:

$$\mathrm{dp} = \frac{4^4}{\Gamma(4)} \mathrm{a}^3 \mathrm{e}^{-4\mathrm{a}} \mathrm{da} \tag{7.1}$$

with $\mathrm{a} = \mathrm{A}/\bar{\mathrm{A}}$ being the cell area in units of the average cell area $\bar{\mathrm{A}}$. The density then is $\rho = 1/\mathrm{a}$ and the Kiang distribution is fitted to the background distribution in regions with low galaxy density. With the average density $\bar{\mathrm{f}}$ the first criterium is $\mathrm{F} = \mathrm{f}/\bar{\mathrm{f}} \leq 0.8$ after Ramella et al. (2001). Over-dense regions have thus $\mathrm{F} > 0.8$ meaning that background regions are separated from the clustered regions on the 80% confidence level. Nevertheless these over-densities can still be random fluctuations. A second criterium quantifies thus the probability that an over-density is caused by a background fluctuation. Ramella et al. in their paper reject over-dense structures with a 5% probability of being a random background fluctuation. These two criteria are adopted for the cluster search.
Ramella et al. included a magnitude binning into their procedure because they performed the cluster search on part of the Palomar Deep Cluster Survey (PDCS, Postman et al., 1996). Over a certain magnitude range this bin is shifted with a given step size. Cluster candidates which are detected in a minimum number (see next subsection) of successive bins are selected. The depth of these data is such that the galaxy density is extremely high. Consequently the Voronoi tessellation technique could probably filter out only the regions with the highest contrast compared to the fore- and background. Furthermore this

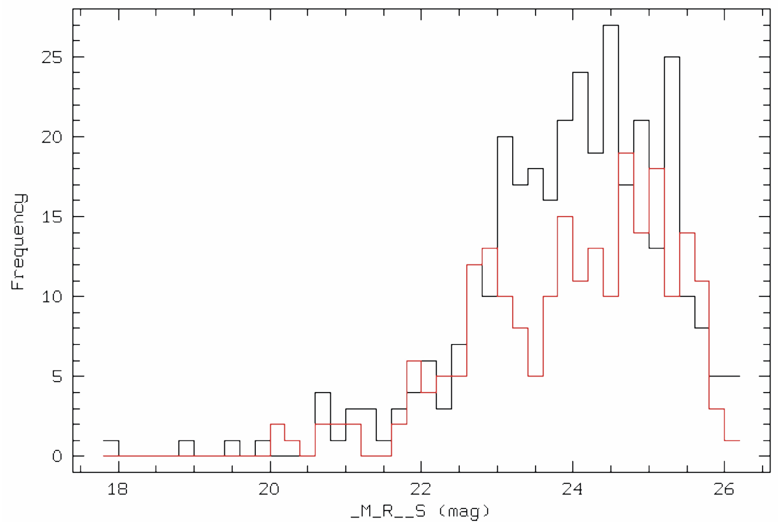

Figure 7.2: Histogram of R (_M_R__S) band magnitudes. The black histogram shows the number of objects per magnitude in the candidate's neighborhood at z$\sim$0.47 while the red histogram is plotted for a control background field.

feature of imposing a magnitude binning should help minimizing the number of spurious clusters. The necessary bin width was found out by inspecting a known cluster candidate from COMBO-17. Fig. 7.2 shows the histogram of the R band magnitudes for this candidate at z$\sim$0.47 in the CDFS. The black magnitude histogram is created in the immediate cluster surroundings ($\sim 3' \times 3'$). Comparing this histogram with the red one derived from a reference background field of similar size reveals an excess of objects in the magnitude range $R \sim [23.0, 25.0]$. Guided by this the width of the R band bins is chosen to be 2 mag. For the run of the Voronoi search the selection at the faint end of the R band magnitudes is 25.2 mag (10σ limiting magnitude). The lower limit is 19.0 mag because there the number density of galaxies is low. Taken together the R band magnitude window of 2 mag is shifted with a step size of 0.1 mag over the R band range [19.0, 25.2] mag.

Two output tables per R band bin are generated by the code: one lists the candidate clusters together with their estimated positions, radius, area, uncorrected as well as corrected cluster and background object numbers, density, confidence level, and S/N (= contrast, explained in the following paragraph). Since for each magnitude bin a separate group catalogue is created the corresponding bin number is also indicated. The other table lists all the galaxies in the R band bin with their coordinates and magnitudes. Again each bin has its own galaxy table. All group tables are merged in the end to yield a big group table

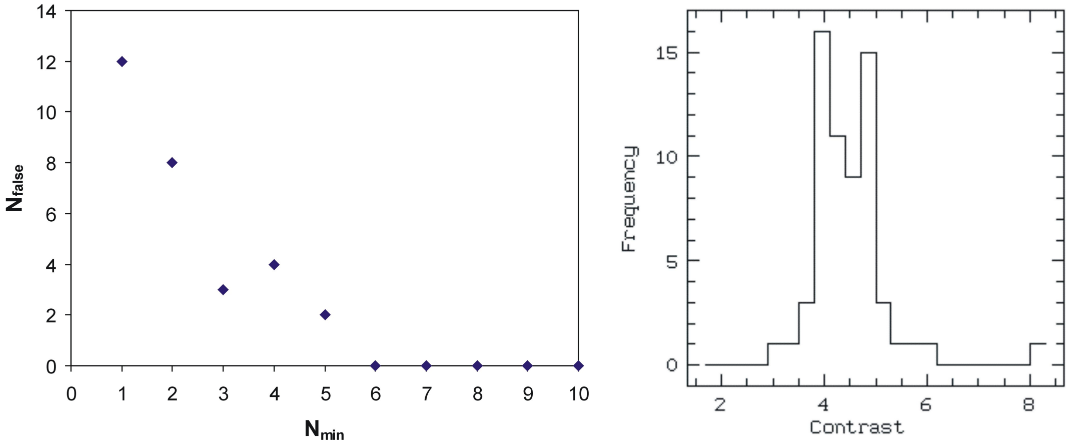

Figure 7.3: Left: Number of false detections N_{false} as a function of the minimum number N_{min} of successive *R* band bins. Right: Histogram of the S/N or contrast values for the spurious cluster detections found in the random distribution.

with all possible cluster candidates. In total 43 catalogues for each step are the result.

Significant cluster candidates are accepted for the final cluster catalogue when two selection criteria are fulfilled. Candidates have to be detected in five successive *R* band bins and to exceed a S/N ratio (or contrast). Ramella et al. defined the contrast as $S/N = N_{gal}/N_{bkg}^{1/2}$, where N_{gal} is the number of galaxies in the corresponding over-dense structure and $N_{bkg}^{1/2}$ is the number of expected background galaxies. Suitable cutoff values have to be determined for thsi study presented here because a data set of different depth and characteristics is examined.

To find the cutoff values for the number of successive *R* band bins N_{min} and the S/N, a randomized background distribution created with the MIDAS command CREA/RANDOM is used (see Sect. 5.2.2). This procedure fixes the false-discovery rate for the Voronoi search. The *R* magnitudes are adopted from the real measurement. On this object distribution the Voronoi tessellation is run and counting the number of detections in successive *R* magnitude bins serves to quantify the limits for N_{min} as well as S/N. Fig. 7.3 shows in the left panel a plot with the number of false detections N_{false} versus N_{min}. It is clearly evident that the number of spurious detections from the random $[x, y]$ distribution decreases strongly with the requirement of detecting the same over-density in N_{min} successive magnitude bins. From this graph the N_{min} cutoff is chosen to be 5. The right panel in Fig. 7.3 is the histogram of the S/N values defined by Ramella et al. for the detected spurious

clusters in the random [x, y] distribution. It peaks at S/N ∼ 4.5 and the cutoff for the cluster search is chosen to be 5.5.
Taken together, an over-dense structure at a certain position is accepted as candidate cluster if it is detected in at least 5 successive R bins and with a contrast value exceeding 5.5. At lower cutoffs the contamination with false detections which is called the false-discovery rate becomes increasingly high.

7.3 Cluster candidates

With the original setup of the search procedure no redshift information is included. It is purely based on geometrical information. A total of 43 R band magnitude bins has been analyzed with the parameter setup discussed above to yield the cluster candidates. Without imposing cuts in the number of detections in subsequent magnitude bins and in S/N the positions of possible cluster candidates is displayed in the left panel of Fig. 7.4. Note that these are not the positions of single galaxies but those of the clusters. There are several single detections which obviously appear only in one R bin and several detections appear to be at the same position which thus are found in more than one bin. After applying the selection criteria, only four cluster candidates remain (see right panel of Fig. 7.4). Table 7.1 lists the coordinates of these candidates in concert with their standard deviation and the number $N_{\rm bin}$ of R bins in which the corresponding candidate has been detected.
For a more quantitative discussion of the significance of the detections, a detailed determination of the selection function would be necessary along the lines presented in Chapter 5. The recovery rate from these calculations would enable to reject marginal cluster detections. However, these Monte-Carlo simulations are beyond the scope of this thesis and are planned to be done as future work.

Table 7.1: Cluster candidates from the Voronoi selection. candidate# denotes the numbering from the procedure, x and y are the coordinates in arc seconds on the field, STDV x and STDV y gives the standard deviation of the position from the detections in the R bins and $N_{\rm bin}$ is the number of detections in successive R bins.

candidate #	**x**	**y**	**STDV x**	**STDV y**	**N_{bin}**
V1	992.52	1697.39	3.42	3.96	15
V12	2103.89	639.07	10.52	17.65	12
V20	1151.29	2031.95	19.70	19.47	9
V23	515.51	1376.67	36.71	12.95	5

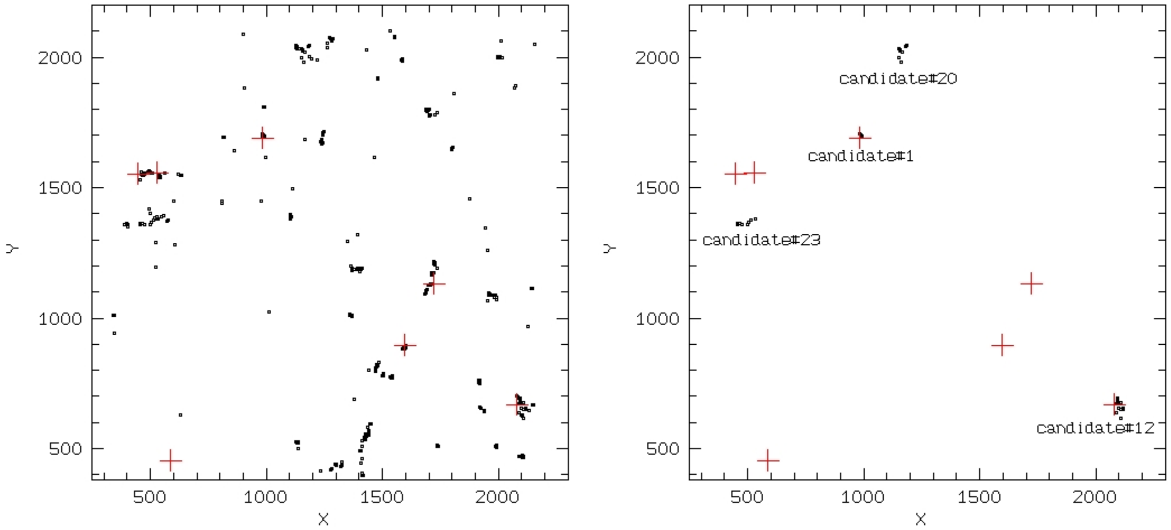

Figure 7.4: Left: Positions of the possible cluster candidates (not of the single galaxies!) in the CDFS (small black dots). No selection according to N_{min} and S/N has been imposed. The positions of the cluster candidates from the 3D search are marked with large red crosses for comparison. Right: These are the candidates' positions after the selection $N_{min} > 5$ and $S/N > 5.5$. Each candidate is flagged with its number from the Voronoi search.

7.4 Inclusion of redshifts

Up to now no redshift information has been included in the Voronoi tessellation. Guided by the idea of using magnitude binning like in the original Voronoi setup and due to the availability of accurate photometric redshifts from COMBO-17, the effect of imposing a redshift binning shall be tested in the following. No magnitude binning is included in this approach. The width of the redshift binning was chosen to be $\delta z = 0.2$ and the bin is shifted with a step size of 0.02 across the redshift range $0 < z < 1.2$. In COMBO-17, the typical redshift error of galaxies is on the order of a few hundredths. The average width of the redshift distribution of clusters is thus expected to be lower than the chosen bin width of $\delta z = 0.2$ when the cluster redshift is found in the center of such a bin. As a result, 51 steps are needed to cover the desired redshift range. Thus 51 group and galaxy tables were available for the analysis. Again all group tables from the Voronoi search including redshifts are merged to one master group catalogue.

The cutoff parameter values are determined along the lines discussed in Sect. 7.2 with a random $[x, y]$ distribution but this time with fixed photometric redshift values. Fig. 7.5

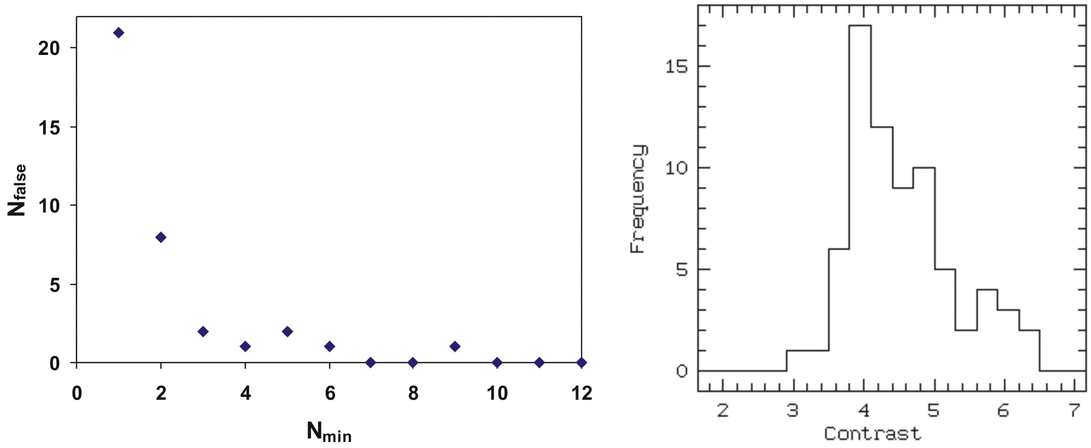

Figure 7.5: Left: Number of false detections $N_{\rm false}$ as a function of the minimum number $N_{\rm min}$ of successive redshift bins. Right: Histogram of the S/N or contrast values for the spurious cluster detections found in the random distribution.

shows the results for the evaluation of the false-discovery rate where the left panel is a plot of $N_{\rm false}$ versus $N_{\rm min}$. As $N_{\rm min}$ increases the number of false detections decreases, at $N_{\rm min} > 5$ the contamination is sufficiently low and so this cutoff value is applied for the search. The choice of the cutoff value for the contrast or S/N is deduced from the right panel in Fig. 7.5 showing the distribution of the contrast values. There is clearly a peak at $S/N \sim 4.0$ with a tail to higher values mostly at around 6.0. Therefore, $S/N > 6.5$ is chosen as the selection criterion.

The cluster candidates from the Voronoi search with redshift binning are listed in Table 7.2 with the numbering adopted from the original Voronoi candidates (see Table 7.1). Only one cluster with candidate#V1 is detected in both versions of the Voronoi tessellation when the corresponding cutoff values are applied. The other three (candidate#V12, V20, V23) could not be found as significant over-densities when the redshift binning is incorporated. But with redshift binning other structures which were not identified as significant before are now judged to be significant cluster candidates, namely candidates#V4+V5, V7, V8, V10+V11. The term V10+V11 means that two not significant candidates – found in the *R* band binning – are merged to one significant candidate. In addition to the positions, the redshifts of the candidates can be estimated by considering the redshift bins in which these were detected. $z_{\rm bin}$ is the median of the central redshift of the bins. This information will be used in the following comparison section.

Table 7.2: Cluster candidates from the Voronoi selection with redshift binning. candidate# denotes the numbering from the procedure, x and y are the coordinates in arc seconds on the field, STDV x and STDV y gives the standard deviation of the position from the detections in the redshift bins and N_{bin} is the number of detections in successive redshift bins. z_{bin} denotes the median redshift from the redshifts of the bins in which the candidate was detected.

candidate #	x	y	STDV x	STDV y	N_{bin}	z_{bin}
V1	988.51	1678.62	1.90	5.76	9	0.74
V4+5	1551.55	840.33	5.15	18.54	10	0.69
V7	1701.08	1149.99	11.79	12.58	8	0.67
V8	2126.31	435.24	4.34	3.96	6	0.77
V10+11	525.36	1548.98	1.58	14.33	7	0.44
V12	2090.18	654.37	22.19	25.54	-	0.58

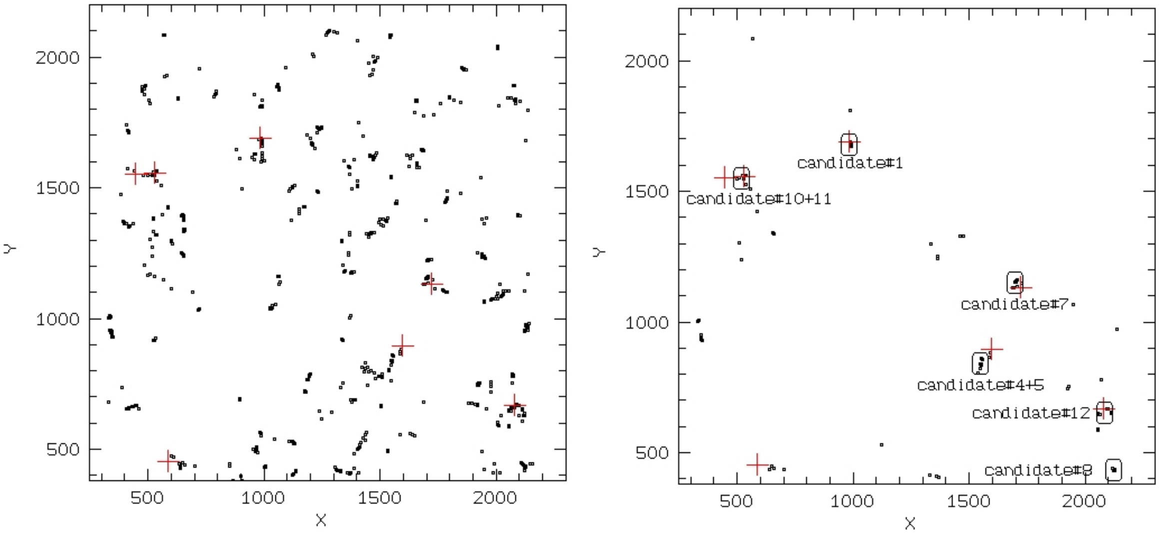

Figure 7.6: Left: Positions of the possible cluster candidates (not of the single galaxies!) on the CDFS (small black dots), inclusion of redshifts. No selection according to N_{min} and S/N has been imposed. The positions of the cluster candidates from the 3D search are marked with large red crosses for comparison. Right: These are the candidates' positions after the selection $S/N > 6.5$. The candidates' positions with the criterion $N_{\mathrm{min}} > 5$ are shown as large black rings while 3D search candidates are the large red crosses.

7.5 Comparison

After the presentation of the cluster candidates from the application of the Voronoi tessellation to the CDFS, the results are compared to the cluster detections of the search method presented in this thesis. Table 7.3 lists all the candidates from the 3D search (see Sect. 6.1), the original Voronoi setup with the magnitude binning, and the Voronoi search with redshift binning. The Voronoi candidates which can be associated with the 3D detections with some offset in the positions are found in the same row. Others were not detected by the Voronoi technique and so the corresponding rows are empty.

The original Voronoi search yields four significant cluster candidates after applying the cutoff parameters. Two of these (candidates#V12 and V1) are already found with the 3D method (Nr 1, 6). By decreasing the over-density cut of the 3D method it can be checked whether the two missed candidates are found below this threshold. Candidate#V23 is detected at the 1.5σ significance level with a redshift of $\sim$0.68 while the #V20 is not found as an over-density in 3D space. For the latter thus the detection with the Voronoi tessellation is solely due to a random 2D density fluctuation. The former could be a low richness group of galaxies but needs deeper data for its confirmation. Fig. 7.4 shows the positions of the candidates before and after applying a selection by the cutoff parameters. From this plot it can be easily seen that the missed candidates are detected at $\mathrm{S/N} < 5.5$ and are thus not significant candidates from this point of view. The inclusion of redshifts is thus essential to increase the contrast for the cluster candidates and to detect 3D structures in a very dense background galaxy distribution.

When the photometric redshift information is included in the Voronoi tessellation by using redshift binning the picture changes compared to the original application. Five candidates from the 3D search (Nr 1, 2, 4, 5, 6) are confirmed by the Voronoi finding with $\mathrm{S/N} > 6.5$ and $\mathrm{N}_{\mathrm{min}}$. For these five candidates the redshifts are consistent within the 1σ redshift scatter given by the redshift calculation of the 3D search. Positional offsets are marginal and can be explained by the different position determination. The other two (Nr 3 and 7) detections from the 3D search which were classified to be less rich systems were missed while an additional candidate (candidate#V8) was found by Voronoi with redshift binning. Three candidates were thus not detected by either the 3D search or the Voronoi with redshift binning.

The following explains the reasons for the discrepancy:

- Candidate Nr 3:
  By inspecting Fig. 7.6 candidate Nr 3 appears at the position determined by the 3D search before and after applying the selection for contrast values exceeding 6.5. But it fails to be selected for the catalogue because it is detected in less than

Table 7.3: Comparison of cluster candidates from the 3D, the Voronoi selection with R band binning (Voronoi simple search) and with redshift binning (Voronoi search z bin). candidate# denotes the numbering from the Voronoi procedure.

3D search					**Voronoi search simple**			**Voronoi search z bin**			
Nr	**x**	**y**	**z**	**δz**	**candidate#**	**x**	**y**	**candidate#**	**x**	**y**	**z_{bin}**
	arcsec	arcsec				arcsec	arcsec		arcsec	arcsec	
1	2085.5	669.2	0.54	0.05	V12	2103.9	639.1	V12	2090.2	654.4	0.58
2	539.2	1556.1	0.47	0.15				V10+11	525.4	1549.0	0.44
3	457.2	1551.9	0.43	0.07							
4	1703.6	1131.8	0.68	0.07				V7	1701.1	1150.0	0.67
5	1604.3	897.7	0.75	0.07				V4+5	1551.6	840.3	0.69
6	991.2	1689.8	0.75	0.05	V1	992.5	1697.4	V1	988.5	1678.6	0.74
7	594.4	453.7	0.36	0.05							
								V8	2126.3	435.2	0.77
					V20	1151.3	2032.0				
					V23	515.5	1376.7				

six consecutive redshift bins and so fails the requirement $N_{\min} > 5$. It has a high significance measured by the 3D search and is missed only marginally by Voronoi including redshifts.

- Candidate Nr 7:
  Candidate Nr 7 does not meet both selection criteria of the Voronoi procedure, so it is only found in the left panel of Fig. 7.6. This candidate was detected with very low significance by the 3D search so that it this either a spurious detection or a system with very low richness.

- Candidate#V8:
  The additional candidate found by the Voronoi tessellation with redshift binning was not found by the 3D method because it is too close to the field corner. At this position the determination of the local galaxy density does not work properly. Border effects can affect both search methods. Here the Voronoi tessellation worked better than the 3D method.

In summary, the inclusion of redshifts for the application of the Voronoi tessellation leads to a confirmation of 5 out of 7 detections from the 3D search method presented in this thesis. Even the redshifts are in good agreement within the 1σ scatter obtained by the histogram method (see Sect. 4.2.3). The agreement is not surprising since both methods proceed with the same input, namely the positions and the photometric redshifts. A more quantitative discussion would be possible if the selection function would be performed for the Voronoi tessellation including redshifts. Similar simulations like for COMBO-17 would yield the recovery rate for the Voronoi search candidates and could be compared with the ones for the 3D method. This is work planned for the future to enable a more profound comparison. The strength of the 3D search lies in the calculation of the local galaxy density for each galaxy. For these calculations, the photometric error distribution is fully incorporated which is not the case for the Voronoi technique. Here the object catalogue is simply divided into redshift bins without including the knowledge of the redshift errors. Consequently, the 3D method is preferred in the HIROCS studies due to the use of the additional redshift error information. However, if data sets on larger sky areas are available and if additional candidates are found by other search techniques (application in the future), the cluster catalogues can be merged. There will always be differences between cluster catalogues. The complementary application of different search methods will yield a more complete view of the galaxy cluster content in an imaging survey.

Chapter 8

Analysis of COMBO-17 structures

After the presentation of the detected cluster candidates in Chapter 6 the results of a first analysis are described in the following. The main aim is to show features that emphasize the significance of the cluster detections with the 3D search procedures developed in this thesis.

In the first Section, a single cluster candidate found in the A901/A902 field at a rather high redshift of 0.8 is examined. The analysis comprises a discussion of the color-magnitude relation and the projected distribution of the galaxies separated into red and blue objects. The color-magnitude relation of the red-sequence for stacked clusters in two redshift bins is presented in the second Section. The candidates in the three COMBO-17 fields are used to create the stacked cluster. There are known structures in the CDFS. A comparison with results from Gilli et al. (2003) and Adami et al. (2005) is described in the third part of this Chapter. Finally, galaxy density contour plots of the clusters found with the 3D technique are compared with the structure analysis of Taylor et al. (2004).

Rest-frame quantities are calculated using h=1 throughout this Chapter.

8.1 Candidate at redshift 0.8

In the super-cluster field A901/A902 an interesting cluster candidate was detected close to the western field border at a redshift 0.80 ± 0.05, see Table 6.3, candidate Nr 1. The richness estimation indicates a rather high richness of $N_{gal} = 37$ and from the simulations to determine the selection function a recovery rate of $R_{rec} = 85\%$ was found at the corresponding redshift and richness. For the following analysis possible member galaxies of this cluster were selected within 2 Mpc at redshift 0.8 around the cluster center. Additionally only galaxies having photometric redshifts within the above mentioned redshift bounds were included in the analysis. With these selection criteria 134 galaxies are left as possible cluster members.

On the basis of the 17-filter multi-color classification results rest-frame colors and luminosities were estimated for the COMBO-17 analysis (Bell et al., 2004). For each galaxy the nearest observed broadband flux was K corrected. A convolution of the best-fitting template spectrum with the filter transmission curves for the Johnson U and V passbands yielded the rest-frame color $(U-V)$ used for this analysis. The accuracy of these colors is on the order of 0.1 mag, absolute magnitudes have an additional error of $(0.1-0.2)$ mag depending on redshift due to distance uncertainties.

Fig. 8.1 shows the rest-frame color-magnitude diagram for the candidate. It exhibits the typical separation between the red-sequence and the blue cloud galaxies. The red-sequence is much tighter while the blue cloud has a larger spread in color. Moreover the red galaxies tend to be brighter and the red-sequence is less densely populated at the faint end than the blue galaxies. Bell et al. (2004) analyzed the red-sequence population from COMBO-17 and provided a color-magnitude relation (see equation 2.1). To separate the galaxies that populate the red-sequence a relation 0.25 mag blueward of the color-magnitude relation is chosen (magenta dashed line in the Fig.):

$$(U-V)_{\mathrm{red}} = 1.15 - 0.31\mathrm{z} - 0.08(\mathrm{M}_V - 5\log h + 20) \tag{8.1}$$

At high redshifts only the brightest galaxies are covered due to the limited depth of the data. To account for this an additional absolute brightness cut is applied. All galaxies with $\mathrm{M}_V < -19.5$ are selected (vertical dash-dotted line in the Fig.), this value is estimated also from the Bell et al. study for a redshift of 0.8. A linear regression to the color-magnitude relation yields the following result:

$$(U-V)_{\mathrm{red}} = -(0.10 \pm 0.04)\,\mathrm{M}_V - (0.96 \pm 0.86) \tag{8.2}$$

In contrast to the reference work where the slope of the relation was fixed to 0.08 the linear fit presented here is not restricted. The constraint of the slope was motivated by studies in the local Universe, e.g. van Dokkum & Franx (2001), and the slopes agreed well with those found in the color-magnitude relations. Considering the color accuracy of 0.1 mag mentioned before the linear fit shown in Fig. 8.1 (dark blue straight line) illustrates that the color-magnitude relation of the cluster candidate and of the COMBO-17 sample from Bell et al. at redshift 0.8 can not be distinguished. The slope from the fit of -0.10 agrees well within its standard error with the fixed value used in Bell et al.

The projected 2D distribution of the red and blue objects is studied in the following. Both populations are again split according to equation 8.1 and their distribution on the sky is shown in the left panel of Fig. 8.2. Red crosses are the red-sequence and dark blue

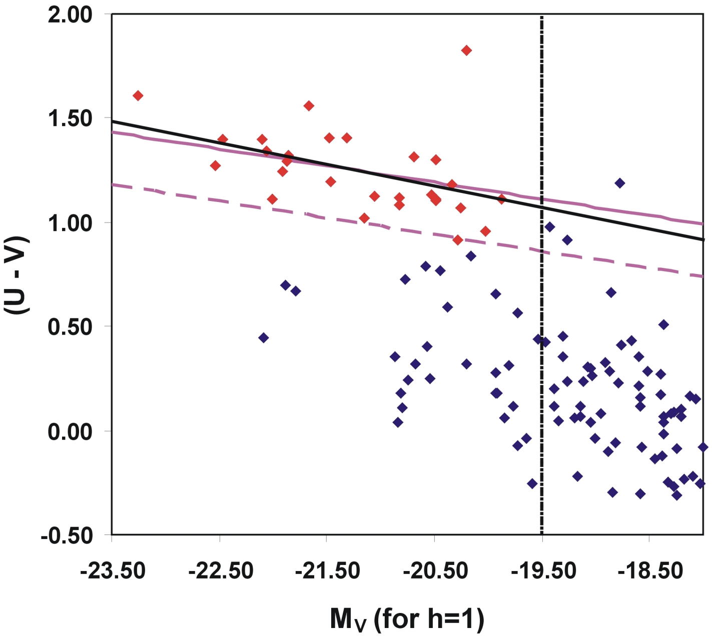

Figure 8.1: Color-magnitude diagram with the rest-frame $(U - V)$ color and the absolute V band magnitude M_V (for h =1) for the cluster candidate at redshift 0.8. The magenta solid line is the color-magnitude relation fit for the red-sequence at redshift 0.8 from Bell et al. (2004), the dashed magenta line is found 0.25 mag blueward of this relation. The black vertical dash-dotted line is a selection cut to separate bright galaxies. Red symbols denote the red-sequence galaxies above the imposed color and brightness cut used for the red-sequence fit which is shown as dark blue solid line. Blue symbols are the galaxies which do not meet the criteria.

dots represent the blue galaxies. Clearly the red galaxies are more concentrated to the center than the blue galaxies are. The position of the brightest cluster galaxy was chosen as the cluster center for this candidate. With this reference position the radial distance of all member galaxies in arc seconds was calculated. For the cluster redshift of 0.8 the corresponding physical size of 1 arc second is 7.3 kpc. Fig. 8.2 shows the histogram of the radial distances in kpc for red-sequence (red line) and for blue galaxies (black line) in the right panel. The red galaxies are concentrated to the cluster center while the distribution of the blue population peaks at approximately 750 kpc from the cluster center. Although the statistics are poor because of the low number of galaxies the distribution of the objects on the image supports the finding.

With the color criterion applied and with $\mathrm{M}_V < -19.5$, a total of 28 red and 29 blue

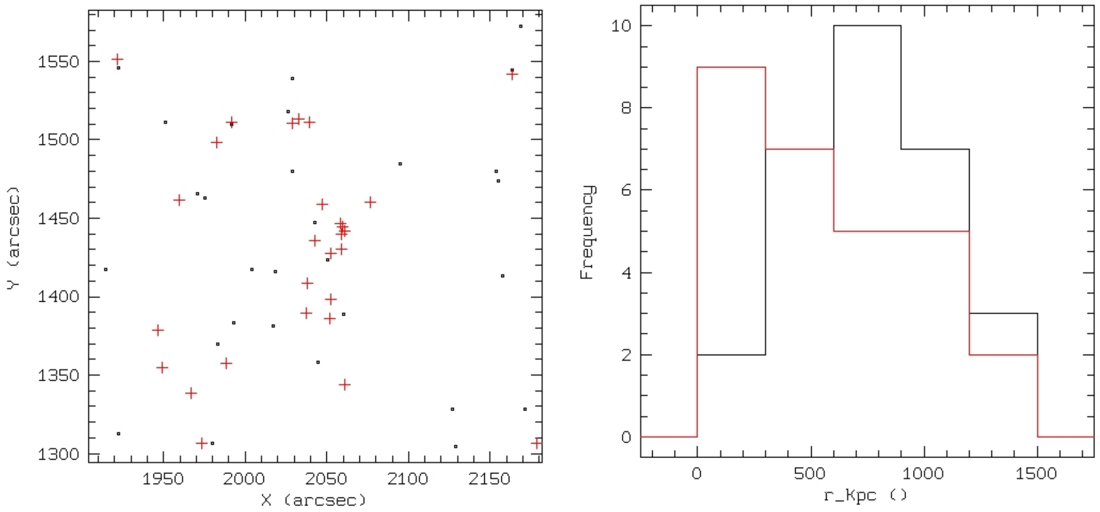

Figure 8.2: Left: Object distribution for red-sequence (red crosses) and for blue galaxies (black dots). See the text for the color and rest-frame magnitude selection criteria. Right: Histogram of the radial distance in kpc for red-sequence (red line) and for blue galaxies (black line). The position of the brightest cluster galaxy was taken as the center position for the distance calculation.

galaxies remain. These values have to be corrected for the contribution of field galaxies. Applying the color criterion the number of expected field galaxies in the cluster area can be determined and used to correct the number counts of the red and blue galaxies. These are 9 red and 19 blue expected field galaxies, respectively. After having corrected for the field contribution the population fraction is found to be $(65.5 \pm 18.5)\,\%$ for the red-sequence and $(34.5 \pm 18.5)\,\%$ for the blue galaxies (assuming Poissonian statistics). The errors are rather high which is due to the low number of cluster galaxies. Nevertheless, the following conclusion can be drawn: For the main COMBO-17 simulation a population mix of 60% elliptical/red and 40% spiral/blue in the whole redshift range was assumed following the collection of population fractions determined at different redshifts published in van Dokkum et al. (2000). Compared to the input for the simulations, the fraction of red galaxies found in this cluster candidate is comparable within the errors indicating that the assumption is reasonable at such high redshifts of 0.8.

8.2 Stacked clusters

A similar analysis of the color-magnitude relation as for the single cluster shown before is presented for stacked clusters at low and intermediate redshift in the following. The clusters are taken from the search results in the three COMBO-17 fields with a recovery rate $\mathrm{R_{rec}}$ exceeding 50%. Such an analysis is directed to compare the possible evolution of the red-sequence population as a function of redshift. Since the number of detected clusters is rather low only two samples are considered in the following redshift bins: $0.3 < \mathrm{z} < 0.6$ and $0.6 < \mathrm{z} < 0.9$. For each cluster, galaxies with a distance of 0.7 Mpc from the cluster center and a redshift within ±0.05 of the cluster redshift are selected. The redshift criterion of ±0.05 is the average of the redshift scatter $\delta \mathrm{z}$ of the cluster candidates. This selection yields 10 clusters in the low redshift sample (in total 455 galaxies) and 5 clusters in the intermediate redshift sample (314 galaxies). Equation 8.1 is applied here, too, to separate red-sequence and blue cloud galaxies. The linear regression results for the red galaxies are illustrated in Fig. 8.3. In the low redshift case the linear fit yields (dark blue line in this Figure):

$$(U-V)_{\mathrm{red}} = -(0.09 \pm 0.02)\,\mathrm{M}_V - (0.42 \pm 0.46) \tag{8.3}$$

The slope agrees within the fit error of 0.02 with the fixed value of 0.08 from Bell et al. (2004). Although there is a trend towards a redder color-magnitude relation the fit errors and the accuracy of the $(U-V)$ color of $\sim$0.1 mag are so large that this trend is considered to be not significant. A similar conclusion can be drawn in the intermediate redshift bin. The fit result is:

$$(U-V)_{\mathrm{red}} = -(0.11 \pm 0.02)\,\mathrm{M}_V - (1.05 \pm 0.41) \tag{8.4}$$

For this sample there is a difference in the slope of the linear fit which is marginally significant, the error is 0.02 and the slope is -0.11. To summarize, the color-magnitude relations for these cluster samples are in good agreement with the results from Bell et al. which are based on a larger data set. Within the uncertainties, the red-sequence does not differentiate between the dense environment and the field galaxies. The formation history of these red-sequence galaxies can be understood in the picture of the passive fading model (van Dokkum et al., 2003) where the galaxies are formed by an initial starburst at high redshifts ($\mathrm{z} \sim 2-4$) and simply dim passively – without forming new stars – to the redshifts, e.g. of the stacked clusters presented here. However, this seems to be a rather un-physical, too simplistic assumption and thus the hierarchical buildup (via mergers/interaction) is judged to play a role as well (White & Frenk, 1991).

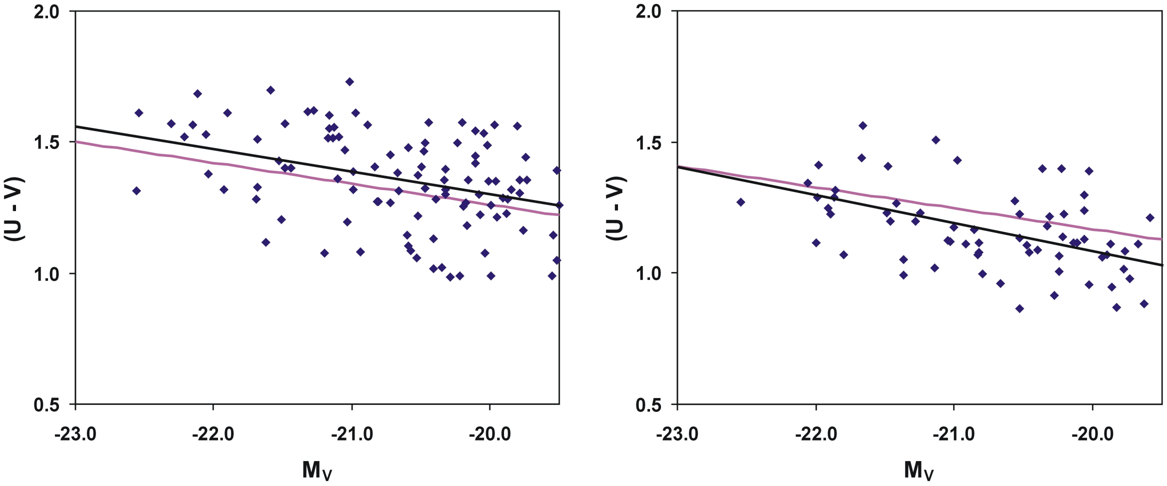

Figure 8.3: Color-magnitude diagrams of the red-sequence objects for the low (left) and high redshift sample (right). The magenta lines are the color-magnitude relations at redshift 0.45 (see equation 2.1) in the left and at redshift 0.75 in the right panel. The black lines are the linear fits to the data points.

8.3 CDFS – Comparison with other work

In a study of the large-scale structure of X-ray sources in the Chandra Deep Field South Gilli et al. (2003) reported two major structures at redshifts 0.67 and 0.73. The detected X-ray sources were identified as Active Galactic Nuclei (AGN). Using spectroscopic data from the K20 near-infrared survey (Cimatti et al., 2002) they found also galaxy over-densities as narrow redshift spikes ($\Delta z \sim 0.02$) at the same redshifts. The structure detected at redshift 0.73 is dominated by a galaxy cluster with a central cD galaxy. The galaxy over-density in redshift space at redshift 0.67 is much more loosely distributed in the field covered by K20. Note that this spectroscopic data set only covers a small area of $6.7' \times 4.8'$ in the center of the area covered by COMBO-17.

Here are the results from the 3D search used in this thesis: Both structures seen by Gilli et al. are not detected in the CDFS when the 3σ over-density cut is applied. The non-detection of the loose structure at redshift 0.67 is caused by the non-peaked distribution of the objects. To understand the reason for the non-detection of the cluster at redshift 0.73 Fig. 8.4 shows the object distribution at the 2σ over-density level in the CDFS in the left panel. The cluster is found at $[x, y] \sim [1350, 1350]$ with only 9 over-dense galaxies. A histogram of the COMBO-17 photometric redshifts is shown in the right panel of Fig. 8.4.

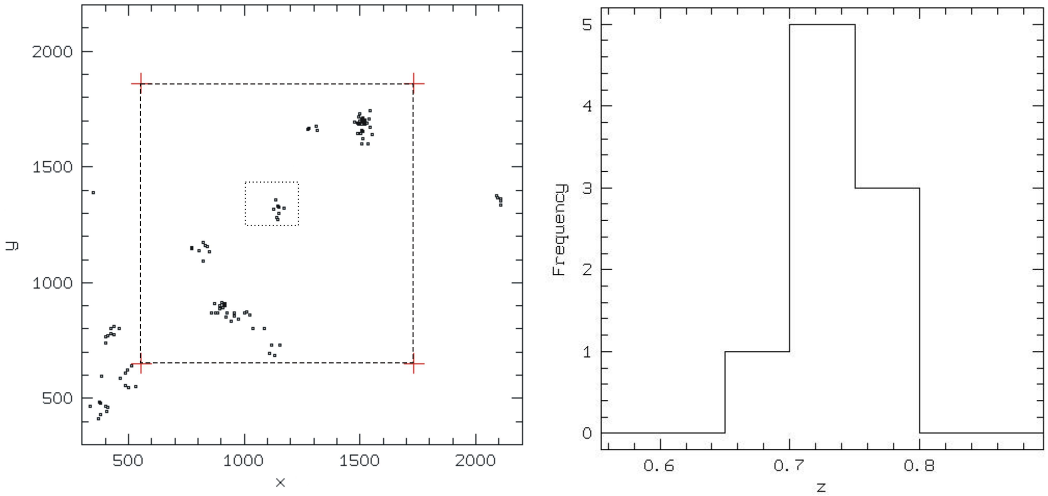

Figure 8.4: Left: Object distribution in the CDFS at 2σ over-density, the cluster at redshift 0.73 is found within the K20 field (dotted rectangle). The large green crosses with dashed line indicates the field covered by VVDS. Right: Redshift histogram for the nine candidate galaxies of the cluster.

For the 3σ case, which is the detection criterion applied throughout this thesis, no objects are found at this position. Even for the lower over-density cuts, the number of member galaxies is not sufficient that this cluster enters the cluster catalogue.

Adami et al. (2005) published a study of compact structures in the CDFS. Their work is based on spectroscopic data from the Vimos VLT Deep Survey (VVDS) which are combined with other spectroscopic, photometric, and X-ray data from different surveys. VVDS spectroscopy for 1599 objects was published by Le Fèvre et al. (2004) on a $21' \times 21.6'$ patch of the CDFS. The photometric data are taken from COMBO-17. While the photometry is adopted directly, these authors derived their own photometric redshifts. For both the spectroscopic and the photometric samples a magnitude limit of 24 mag in the I band is imposed. Structures in the spectroscopic data were detected with a friends-of-friends algorithm. For the detection of structures in the photometric data an adaptive kernel technique applied to color and density maps was used.

Unfortunately, the following comparison is complicated by the fact that diagrams in the Adami et al. paper have unclear scaling of the axes. Furthermore, contrary to the usual convention, East is to the right of the plots. Fig. 8.5 compares the detected structures on the basis of the photometry between Adami et al. and the 3D search. From both studies there is clear evidence for an extended, wall-like large-scale structure feature at

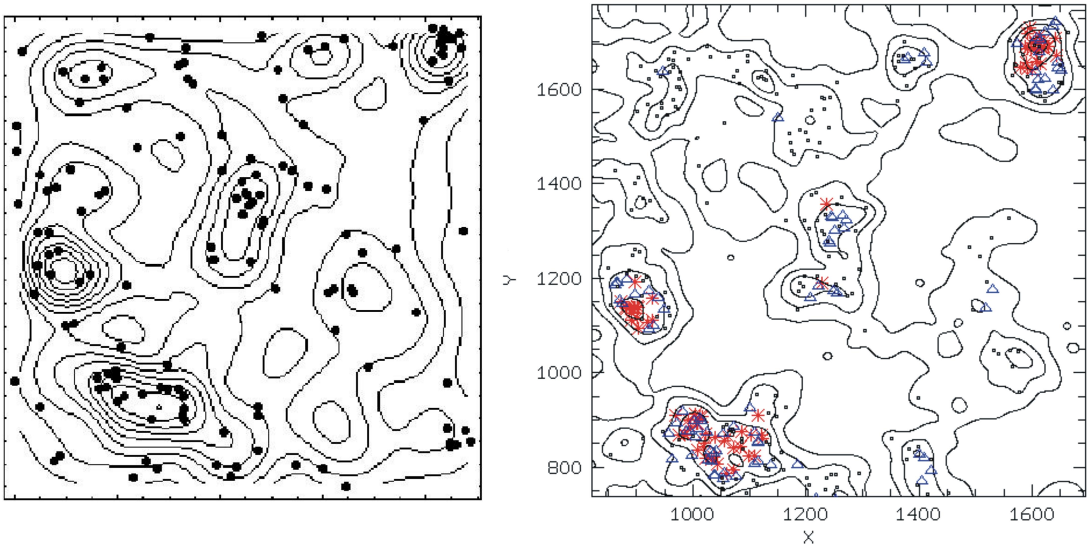

Figure 8.5: Left: Adaptive kernel density contours of the structures at redshift 0.74 (Adami et al., 2005). Red galaxies with $(B-R) > 2.0$ are shown as large black dots. Unfortunately, the axes are not labelled in their paper. Right: Galaxy density contours derived in the 3D search for a sample in the redshift range $0.60 < z < 0.85$ (positions in arc sec). Approximately the same area is shown as in the left panel. An exact match was not possible because the axes in the left panel were not labelled in the source paper. Galaxies are shown at the 1-2σ (small black dots), 2-3σ (blue triangles), and 3σ and higher (red asterisks) over-density level. East is to the right and North to the left in both plots.

redshift 0.74 which extends over a significant part of the CDFS. Several galaxy groups of different, mostly low, richness are members of this wall. A less prominent feature is found at redshift 0.68. The comparison is done only for the structure at redshift 0.74 in the following. The left panel in Fig. 8.5 shows the adaptive kernel galaxy density contours for the wall-like structure from Adami et al (2005). Only red galaxies with a selection $(B-R) > 2.0$ are plotted which highlight the highest density peaks in this area. With the Gaussian image smoothing procedure presented in Sect. 4.2.3 a density contour plot of the galaxy distribution in the redshift range $0.60 < z < 0.85$ is produced. For the comparison the right panel in Fig. 8.5 displays this contour plot. The over-density level for this field (see Sect. 6.1) is used to select objects according to 1-2σ, 2-3σ, and $> 3\sigma$ significance. The selected galaxies are shown as small black dots, blue triangles, and red asterisks, respectively. From this analysis the three structures to the top right, bottom

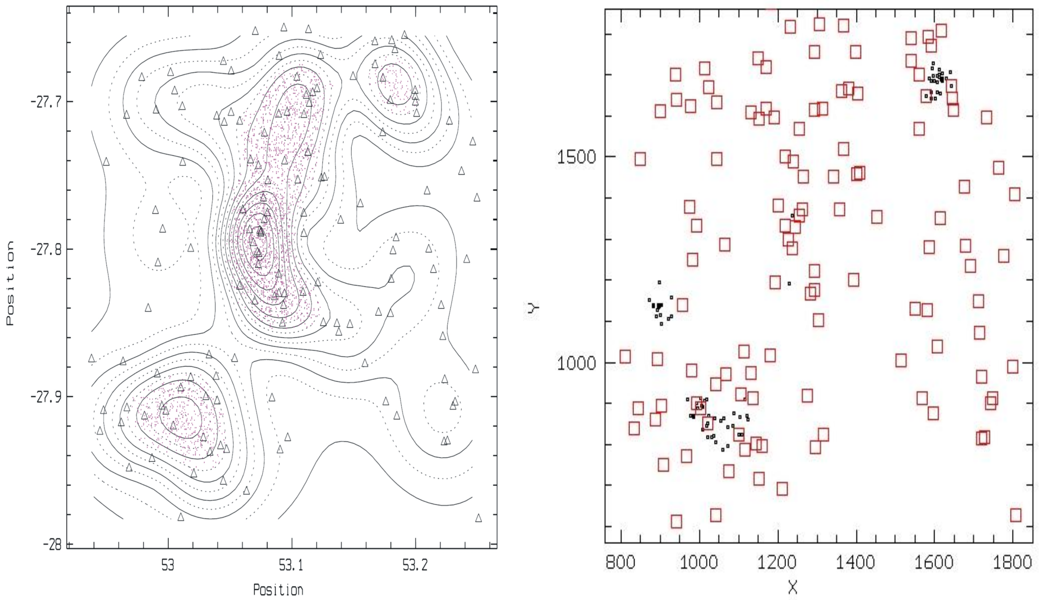

Figure 8.6: Left: Iso-contour plot of the galaxy density inside the wall at redshift 0.74 (Adami et al., 2005). Only galaxies (triangles) with a measured spectroscopic redshift are used. Shaded areas are significant at the 3σ level in galaxy density. Right: Galaxy distribution at the $>3\sigma$ level from the 3D search (small black dots). The red squares are the galaxies from the VVDS catalogue in the redshift range $0.72 < z < 0.75$ (spectroscopic redshifts). Positions are given in arcsec. Note that both plots are scaled in x direction to match the scaling of the y axis.

left, and the left are detected at the $>3\sigma$ level. The structure in the center was not identified with the 3D procedure, see discussion before, but appears in the smoothed galaxy distribution. According to the interpretation in Adami et al. (2005) these structures are poor clusters (e.g. the one in the center) or groups. For the VVDS spectroscopy the sampling rate for $I < 24\,\mathrm{mag}$ is 25% and is rather inhomogeneous over the field-of-view. As a consequence structures can be missed if such data are used on their own. To illustrate this, Fig. 8.6 displays the galaxy density iso-contour plot on the left for galaxies with spectroscopic redshifts inside the wall at redshift 0.74. The most prominent peak is located in the center while the other peaks appear less pronounced. On the basis of the photometry the peaks at the border are found to be more prominent compared to the peaks found with spectroscopic redshifts. In the right panel of this Figure is shown the distribution of galaxies with $>3\sigma$ over-density from the 3D search and the selected galaxies which were measured in the VVDS. It is obvious that the sampling of the highest density peaks is bad which explains the difference in the prominence of density peaks from the photometric and the spectroscopic analysis. This is caused by the selection of objects which should be observed spectroscopically. The advantage of the spectroscopic redshifts is their better accuracy compared to the photometric redshifts. The best method would be to obtain spectra for all objects on a large sky area. Unfortunately, it is extremely time consuming to obtain spectra for all galaxies in a large sky area and thus not feasible. An imaging survey, like HIROCS, can cover larger sky areas in less observing time with a good sampling rate compared to the spectroscopic method. The result is a large catalogue of galaxy cluster candidates which is homogeneously selected. However, the structures found in an photometric survey have to be confirmed by spectroscopy. On the basis of the first HIROCS cluster detection, Chapter 9 illustrates how the procedure of analysis and confirmation works after a galaxy cluster candidate has been identified.

8.4 A901/A902 – Comparison with weak lensing

The A901/A902 field is dominated by a super-cluster system composed of three rich clusters (A901a, A901b, and A902) in the foreground at redshift 0.16. Taylor et al. (2004) presented a weak lensing analysis which yielded a detailed insight into the light and mass distribution in and around these clusters. The gravitational potential of the foreground super-cluster bends the light from background sources and induces tiny deformations of the object shapes which is termed weak lensing. Weak lensing is a powerful tool to study directly the dark matter distribution of the lensing potential (here that of the super-cluster). Thereby the relation between light and mass distribution can be studied. In the background of A902 these authors found another galaxy cluster at redshift ∼0.48 as an excess in galaxy number density. Motivated by this they performed a two cluster lensing analysis for these two almost aligned systems. In the following the distribution of the over-dense structures presented in this PhD thesis are compared with the findings from Taylor et al.

Contour plots are created with the Gaussian smoothing scheme introduced in Sect. 4.2.3. Taylor et al. produced number and luminosity density plots by Gaussian smoothing. A similar width of the Gaussian is chosen ($90''$) here. The object selection was done at the 3σ over-density level. For two redshift slices, one around the super-cluster and the other around the background cluster redshift, Fig. 8.7 displays the cross-section of the 3D gravitational potential from the weak lensing study. In the left panel the dark grey to almost black regions in the center and the bottom outline the potential well of the three clusters, the fourth trough at $[\mathrm{x},\mathrm{y}] \sim [23.5', 6.0']$ is a neighboring cluster at the same redshift. Inspecting the right panel the $\mathrm{z} = 0.48$ cluster can be identified in the lower part

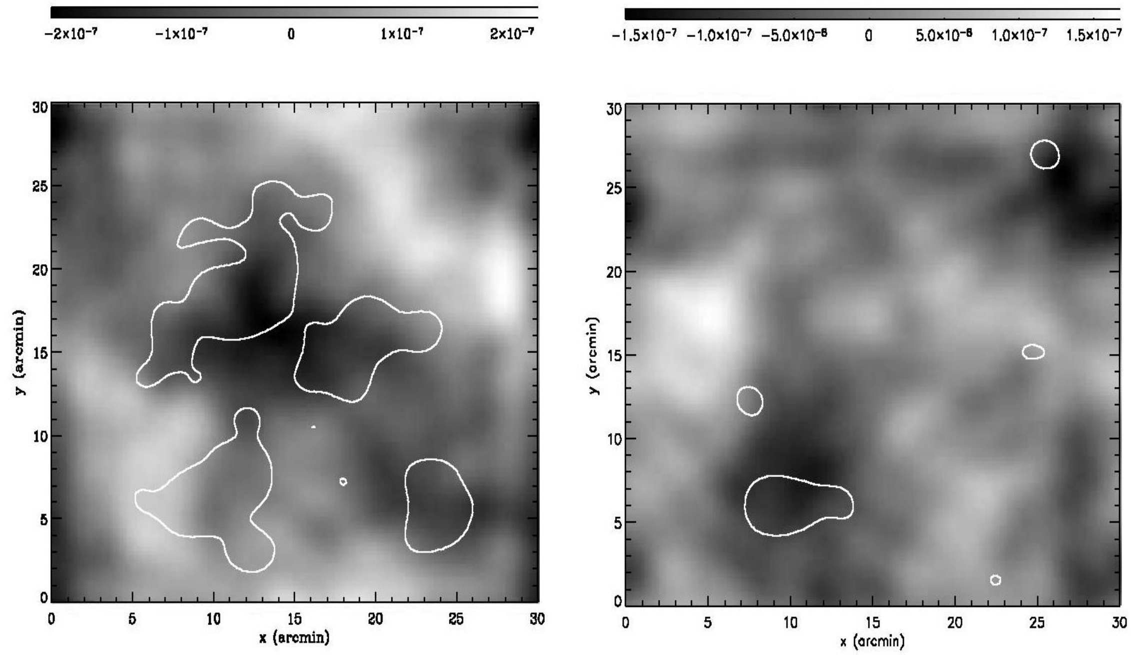

Figure 8.7: Cross-sections of the 3D gravitational potential for the A901/A902 field from Taylor et al. (2004). Left: [x, y] slice in the redshift range 0.15 to 0.20 (luminosity density contour at $L = 8 \times 10^{10}$ $L_\odot$ $[h^{-1}\mathrm{Mpc}]^{-3}$). Right: Slice in the redshift range from 0.45 to 0.5 (luminosity density contour at $L = 2 \times 10^{10}$ $L_\odot$ $[h^{-1}\mathrm{Mpc}]^{-3}$).

of the plot. The white contours in both panels are lines of constant luminosity density.

The super-cluster can be better identified in the plots with the cross-sections of the 3D luminosity density for both redshift displayed in Fig. 8.8 (Taylor et al., 2004). The left panel shows the four over-densities at redshift 0.16 while the right panel shows those at redshift 0.48.

For the comparison the galaxy density contour plots of the $>3\sigma$ over-densities from the 3D search at redshifts $z < 0.25$ and $0.43 < z < 0.53$ are displayed in Fig. 8.9 to the left and to right, respectively. Concerning the super-cluster there is a good correspondence between the peaks in the luminosity density from Taylor et al. and the peaks in the density contours from the 3D cluster search of this thesis. The main focus of this thesis is directed to higher redshifts than that of the super-cluster. Therefore the Gaussian width for the position estimation of the 3D search was tuned for finding clusters at higher redshifts and not for the redshift of the super-cluster system at redshift 0.16, a detailed comparison of

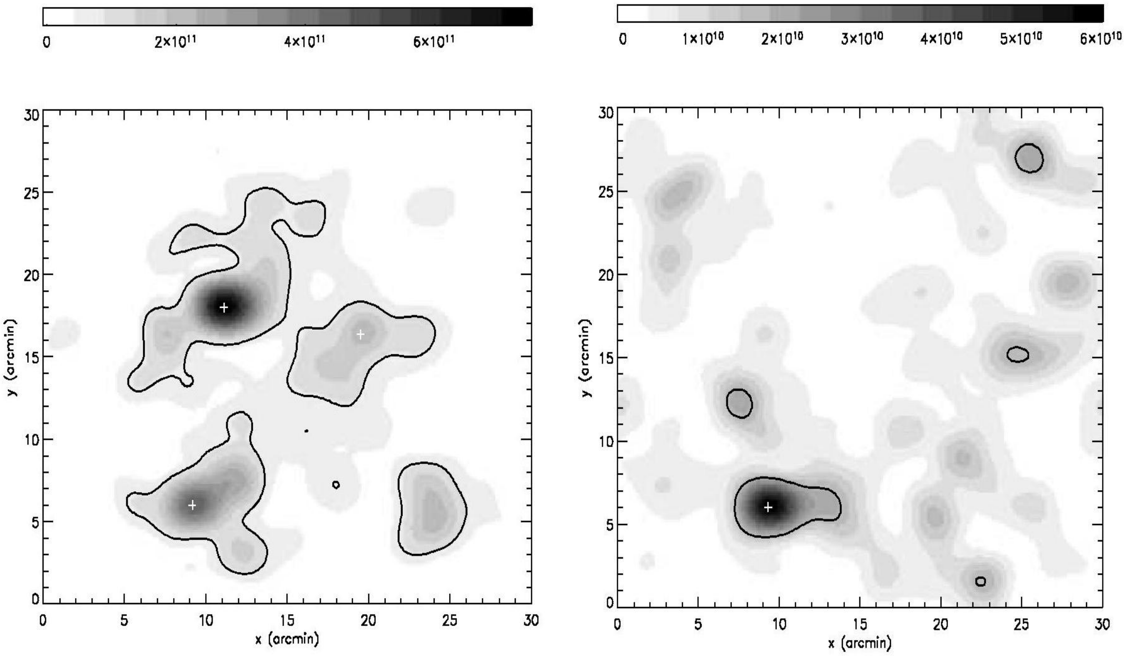

Figure 8.8: Luminosity density cross-sections for the A901/A902 field from Taylor et al. (2004). The same redshift slices and contours as in Fig. 8.7 are used in both panels.

the contours cannot be carried out.

More interesting is the comparison of the structures around redshift 0.48. The most prominent peak is the cluster in the lower part of the image. But there is also evidence for other significant structures in the Taylor et al. luminosity density plots which are detected at the $>3\sigma$ over-density level by the 3D search presented in this thesis: Three cluster candidates were found at $[\mathrm{x,y}] = [1924, 708]$, $[\mathrm{x,y}] = [1945, 2032]$, and $[\mathrm{x,y}] = [803, 1093]$ with redshifts around 0.47 (see Fig. 8.9). Note that not all over-densities in Fig. 8.9 are detected by the position and redshift estimation procedures because these do not meet the selection criteria (see Sect. 4.2.3). These three candidates appear in Fig. 8.8 where the contour lines are drawn.

The automatic detection can reach to even higher redshifts than 0.5. Lensing needs a background of galaxies at higher redshifts and this is not provided with the given data set. Fig. 8.10 shows all the structures at the $>3\sigma$ significance at redshifts beyond 0.6. In total three cluster candidates were found at these redshifts ($[\mathrm{x,y}] = [2046, 1439]$, $[\mathrm{x,y}] = [1871, 1161]$, and $[\mathrm{x,y}] = [1064, 1802]$). The most prominent is the cluster at red-

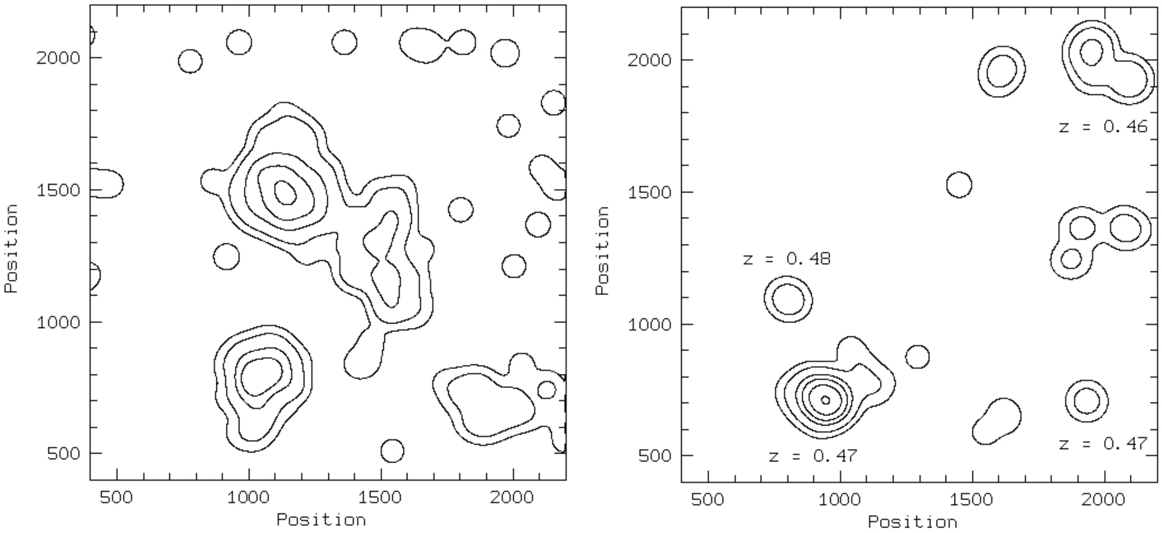

Figure 8.9: Galaxy density contours derived from galaxies with over-density $> 3\sigma$ after a Gaussian smoothing with 90″ FWHM (positions in arc seconds). Left: Redshifts $z < 0.25$. Right: Redshifts $0.43 < z < 0.53$.

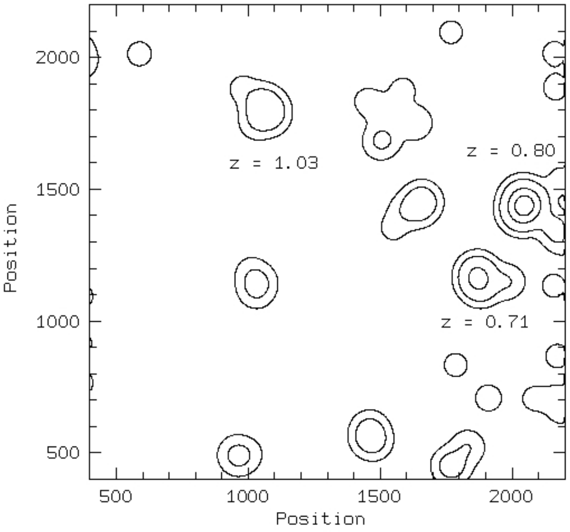

Figure 8.10: Galaxy density contours at redshifts $z > 0.6$, see details in Fig. 8.9.

shift 0.8 which is located to the western border of the field (see Sect. 8.1).
To summarize, the clusters at redshifts 0.16 and 0.48 are found easily in both studies. Whereas additional structures at redshift 0.48 was already evident in the work of Taylor et al., these candidates were recognized as possible cluster candidates finally from the 3D search procedure presented in this thesis. Cluster candidates at even higher redshifts cannot be detected by the weak lensing technique in this field. Lensing needs a background of high redshift galaxies. E.g. to be able to detect the cluster candidate at redshift 0.8, the object catalogue would have to be extended to redshifts of ∼1.5 at least. This poses a problem if one wants to apply the weak lensing technique for the search of galaxy clusters at redshifts beyond unity.

Chapter 9

First HIROCS galaxy cluster candidate

In the course of the data reduction of the OMEGA2000 exposures a possible rich, high-redshift galaxy cluster candidate has been visually identified in the HIROCS 03h field. The detection, data, and first analysis of this finding are described in this Chapter.

9.1 Detection and data

The discovery image obtained in the H band is shown in Fig. 9.1. In the lower mid part of the image the cluster candidate is evident as an over-density in $[\mathrm{x}, \mathrm{y}]$ of faint almost point-like objects. Motivated by this finding the other filter exposures were also reduced and flux calibrated provisionally to substantiate the existence of an object density excess. The peculiarities of the reduction in the different bands were described in Sect. 3.3. In this field the B and R exposures originate from the WFI while the i as well as the z band data were observed with LAICA. The single reduced exposures were summed to yield a deep image of the field for each filter. In a subsequent step, these sum images were used to detect all objects with the SExtractor source detection software (Bertin & Arnouts, 1996). During this procedure a 3σ detection threshold was applied to detect even the faintest sources. The preliminary catalogue produced in this way contained the magnitudes and an estimate of its statistical error. The photometric calibration was done using 10 bright stars with known magnitudes lifted from the SDSS (u, g, r, i, z) in the optical and the 2MASS (J, H, K) surveys in the near-infrared. Using the five images taken with the HIROCS filter set different combinations of 3-color images have been produced on which the cluster candidate appears more clearly. Fig. 9.2 shows one of these 3-color images

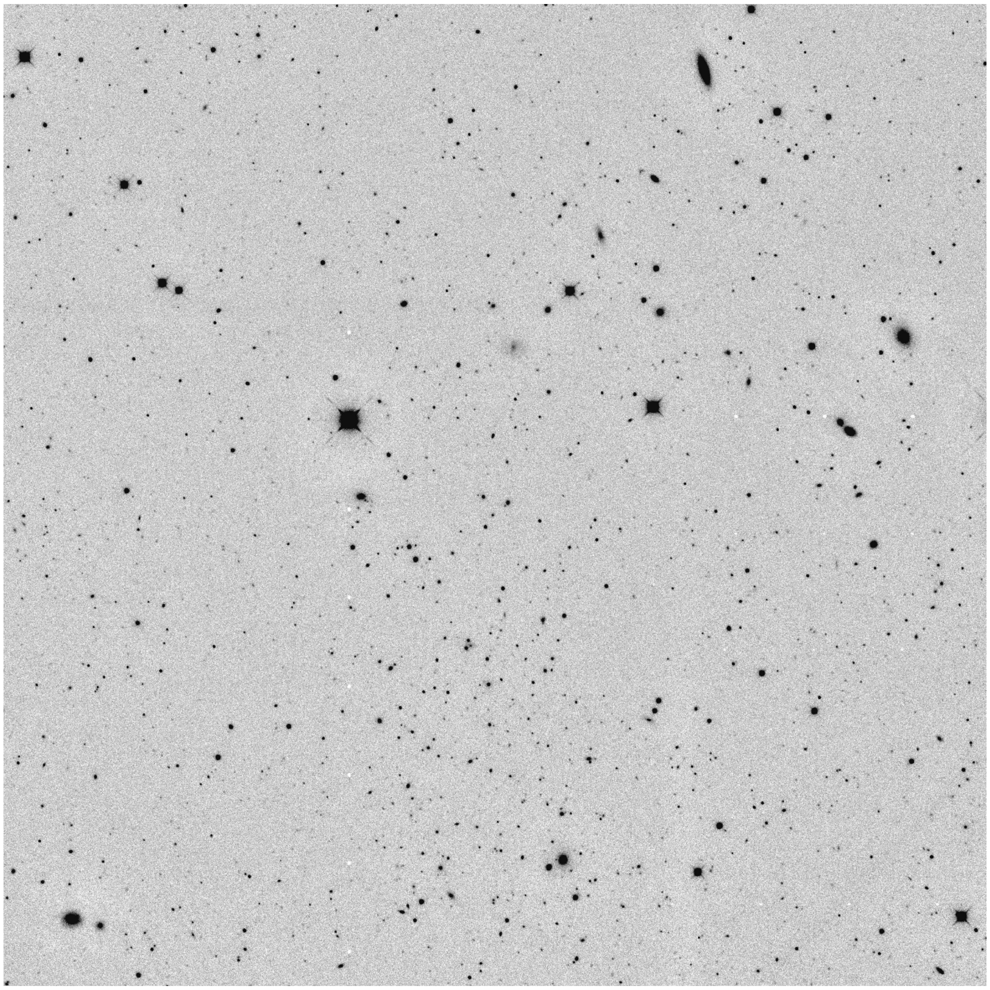

Figure 9.1: *H* band detection image (scale: $\sim 10' \times 10'$) of the cluster candidate. It is a pipeline reduced image. The candidate is evident in the lower-mid part of the image as an excess of faint objects.

produced from the *B* (blue), *R* (green) and *H* (red) exposures. The slightly elongated cloud of mostly red objects below the two bright stars in the image center indicates the high redshift of the candidate's galaxies. Red colors mean here that most of the flux is detected in the *H* band and, consequently, the spectra are considerably shifted into the near-infrared wavelength regime.

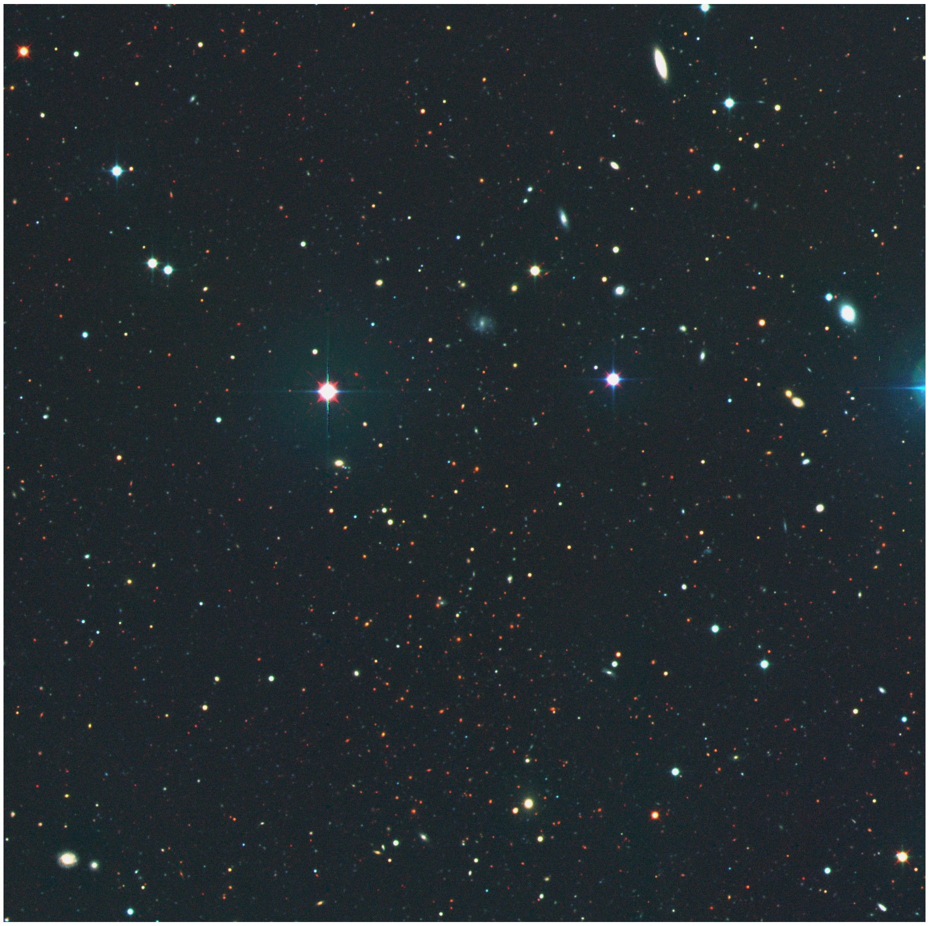

Figure 9.2: 3-color image (scale: $\sim 10' \times 10'$) of the cluster candidate produced from the reduced B (blue channel), R (green), and H (red) band exposures. The image shows the same sky region compared to the detection image shown before. With the color coding the candidate is more clearly seen as an over-density of red objects which is evidence for high redshift. Note that the red channel was chosen for the H band.

9.2 Analysis

After the provisional calibration a color-magnitude diagram with the R and z band magnitude was produced (Fig. 9.3). For comparison and for a first estimation of the candidate's redshift this Figure also shows the model $(R-z)$-z diagram produced for the Red-Sequence Cluster Survey (Gladders & Yee, 2000). Both plots were created on the

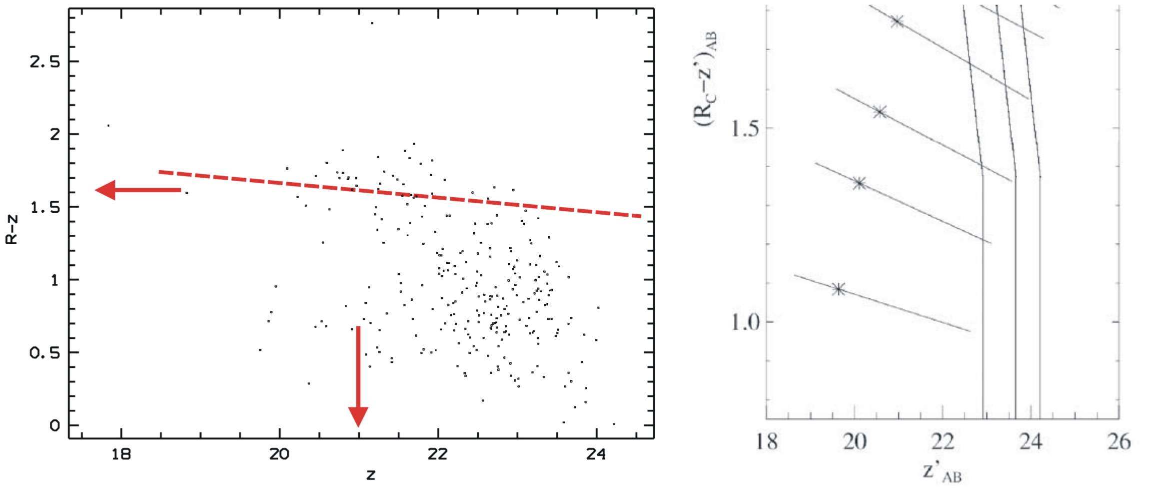

Figure 9.3: Left: $(R-z)$-z diagram of the HIROCS cluster candidate. A red-sequence (red dashed line) and the blue cloud typical for galaxy clusters are clearly visible. The red arrows indicate the approximate position of the knee of the luminosity function and the corresponding color. Right: The theoretical color-magnitude diagram produced for the RCS (Gladders & Yee, 2000). The inclined lines are red-sequences at different redshifts ranging from 0.5 (bottom line) to 0.8 (top line). The stars mark the position of the knee of the luminosity function. Both plots are produced in the AB magnitude system. The filters used in the two surveys are not identical but they are comparable in terms of effective wavelength.

AB magnitude system. The slightly inclined lines in the color-magnitude diagram of Gladders & Yee indicate red-sequences at different redshifts ranging from z = 0.5 (line at the bottom) to z = 0.8 (line at the top). The candidate's color-magnitude diagram clearly shows a red-sequence (red dashed line) with $(R-z) \sim 1.6$ at $z = 21$ mag (red arrows). Below that, towards fainter magnitudes, the blue cloud galaxies can be seen. Evaluating the RCS plot at the same z band magnitude and $(R-z)$ color, the cluster's redshift is estimated to be at z ∼ 0.7. This estimation is based on the comparison of the HIROCS and the RCS color-magnitude diagrams. The measurements in the five filters allow a multi-color classification which yields the object class and the redshifts of the galaxies. Up to now, magnitude error estimates were determined with the SExtractor source detection procedure which only provides statistical errors. The multi-color classification procedure ideally needs measurement errors computed from a series of exposures for the color indices. This was not possible at that stage due to the preliminary reduction. Thus the errors are calculated based on the assumption that the data meet the desired limiting

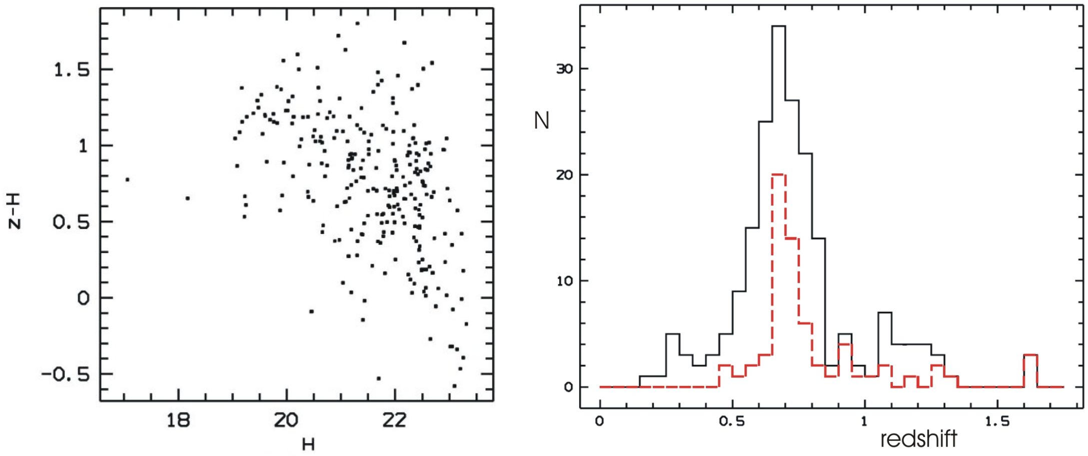

Figure 9.4: Left: $(z-H)$ color-magnitude diagram. Red-sequence galaxies are found at $(z-H)>1$. Right: photometric redshift histogram. The distribution for all galaxies shows a peak at z ∼ 0.7. With a selection for red-sequence galaxies the z peak becomes narrower (red dashed line) and the redshift is determined more accurately: $\mathrm{z}=0.708\pm0.037$.

magnitudes. The corresponding formula to determine the magnitude errors was shown in equation 4.1 and the errors of the color index (A – B) of the filters A and B are determined by:

$$\sigma_{(\mathrm{A}-\mathrm{B})} = \sqrt{\sigma^2_{\mathrm{m_A}} + \sigma^2_{\mathrm{m_B}}} \tag{9.1}$$

$\sigma_{\mathrm{m_A}}$ and $\sigma_{\mathrm{m_B}}$ denote the magnitude errors measured for the filters A and B. Note here that the multi-color classification relies on the CDmag system (see Appendix C).

The multi-color classification works very well with the 5-filter HIROCS photometric data. A histogram of the photometric redshifts is shown in the right panel of Fig. 9.4 and it is clearly dominated by a peak at redshift ∼0.7. The black line was drawn without any selection of the object catalogue. To determine a better redshift estimation a selection for red-sequence objects is applied to the object catalogue. The left plot in Fig. 9.4 shows a $(z-H)$-z color-magnitude diagram where the red-sequence is found at $(z-H)>1$. After selecting all objects with $(z-H)>1$ the redshift peak becomes narrower (red dashed line in the z histogram) and the redshift is much better defined: $\mathrm{z}=0.708\pm0.037$. This is calculated on the basis of 40 cluster members.

How accurate the multi-color classification works can be illustrated by inspecting the best-fitting galaxy templates which should match the measured flux values. Fig. 9.5 shows two examples of the best-fitting spectra for the galaxies which are supposed to belong to the

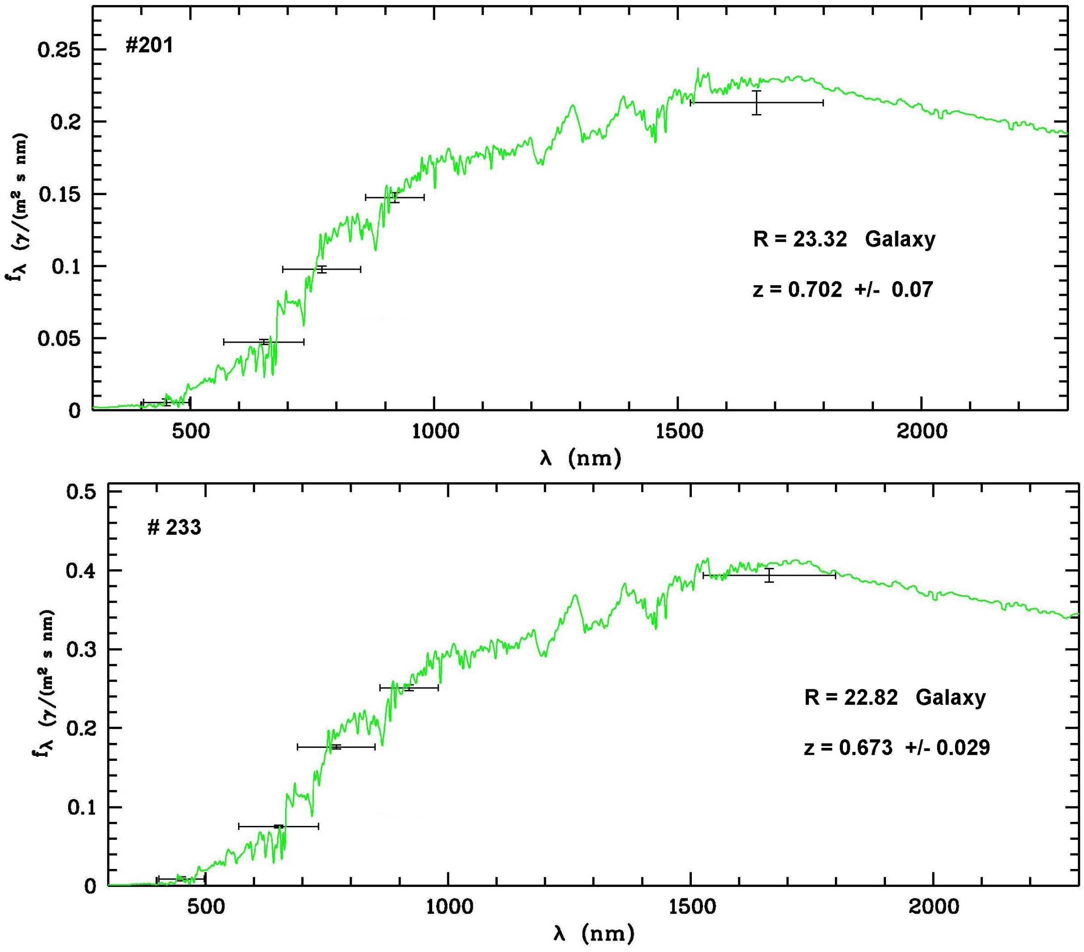

Figure 9.5: Best-fitting galaxy templates for two example galaxies. The black error bars show the measurements in the five HIROCS filters with 1σ errors for the flux and the error bars in λ-direction indicate the filter edges where the transmission decreases to 50%. The green line is the best-fitting template spectrum from the galaxy library (see Sect. 4.1.2). Also shown are the sequence number in the object catalogue, the object type, the R band magnitude, and the photometric redshift estimation.

candidate. As can be seen the measurements (black error bars) and the library spectrum (green line) fit very well and thus in general the classification based on only five filters works very well.

9.2.1 Spectroscopic confirmation

Up to this point the above analysis only presents a galaxy cluster candidate because usually the cluster has to be confirmed by spectroscopy. Therefore, the HIROCS team applied for director's discretionary time at the Calar Alto 3.5m telescope equipped with MOSCA. MOSCA is a multi-purpose instrument which also allows multi-object spectroscopy[1]. For the observation one slit mask was prepared and manufactured at the work shop of the MPIA.

Hermann-Josef Röser has provided a WINDOWS Excel software tool with which slit masks for several telescopes and multi-object spectrographs can be planned. With this program the positions and sizes of the long-slits which shall be drilled into the mask could be fixed. It automatically creates a control program for the CNC machine which is used to manufacture the slit mask. In the case of MOSCA, on the order of 20 objects fit onto a single mask. This depends of course on the object size but this estimate is valid for distant extra-galactic sources which are not much larger than a typical seeing disk. For each object the slit length has to be large enough for the accurate determination of the sky background. The object separation is thus approximately larger than $10''$.

The primary aim of the multi-object spectroscopy was the confirmation of the cluster candidate. This shall be achieved by the determination of the redshifts for as many as possible galaxies which have photometric redshifts close to the estimated cluster redshift. Therefore the photometric redshift range was limited to $0.60 < \mathrm{z} < 0.75$. Since the allocated time comprised only one half night, the effective possible exposure time was determined to be $2 \times 2\,500$ seconds. Because of this, only the brightest galaxies could be considered and the preliminary object catalogue was selected with $R < 22.9$ mag. At magnitudes brighter than $R = 21$ mag the contamination with stars rises and these objects were rejected, too. On the basis of this selection, the sky positions of the remaining 26 objects were determined. It turned out that only twelve possible cluster galaxies fitted on the slit mask because the separations between them were rather small. The angular size of the cluster candidate is about $3'$ leaving about $6''$ for each galaxy. From the multicolor classification the galaxy type was also known. A large fraction of the galaxies was classified as ellipticals but also a few blue late-type galaxies were present. No object type selection for only ellipticals which dominate cluster populations was applied. The redshift determination for star-forming blue galaxies is easier because the prominent O II 3727 emission line shows up in such spectra. Fig. 9.6 shows the final slit mask layout for the spectroscopic follow-up. To be able to exactly point the telescope two bright stars have been selected which are brought to the holes which are indicated by the two black dots. Besides the twelve possible cluster galaxies seven more slits have been drilled to observe

---

[1] see http://w3.caha.es/aguirre/mosca/mosca.html

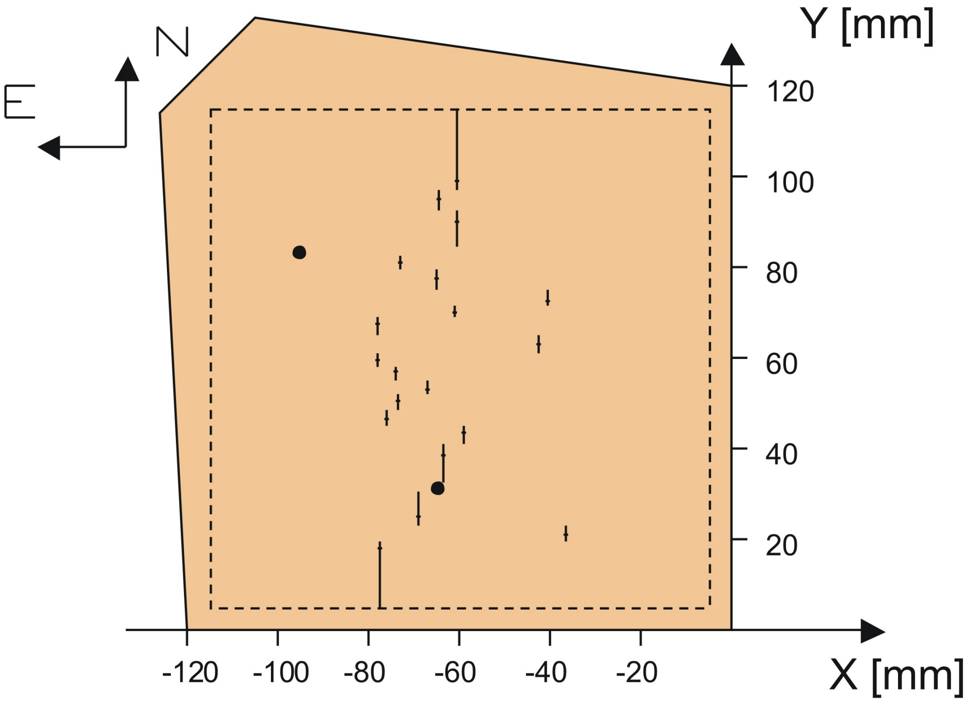

Figure 9.6: Slit mask layout for the spectroscopic follow-up with MOSCA: the positions of the slits in the focal plane $[x, y]$ in mm are indicated by the long lines. The object positions on the slits are marked by small perpendicular lines. The orange border is the edge of the mask while the dashed rectangle is the field-of-view of the instrument. For the sky orientation the N-E direction is marked, too. To be able to find the right pointing position two stars are brought to the position of the holes which are shown as two black dots.

galaxies in the foreground. These are found mainly outside the cluster candidate's area. One of the HIROCS team members, M. Zatloukal, carried out the reductions of the MOSCA data. The analysis of the spectra provided the first confirmation of a galaxy to be at the redshift of the cluster candidate ($z = 0.7$) derived from the photometry. In the raw spectrum an emission line was apparent in the spectrum of this galaxy. Fig. 9.7 shows the best-fitting template spectrum and the measured MOSCA spectrum as an insert. The emission line OII 3727 is indicated by the red arrow and the shift of this line away from the laboratory wavelength yields the redshift. It is 0.668 confirming the photometric redshift (z=0.689±0.023) derived with the 5-filter measurements within the 1σ error derived the classification. The multi-color classification scheme classified this galaxy as an early-type

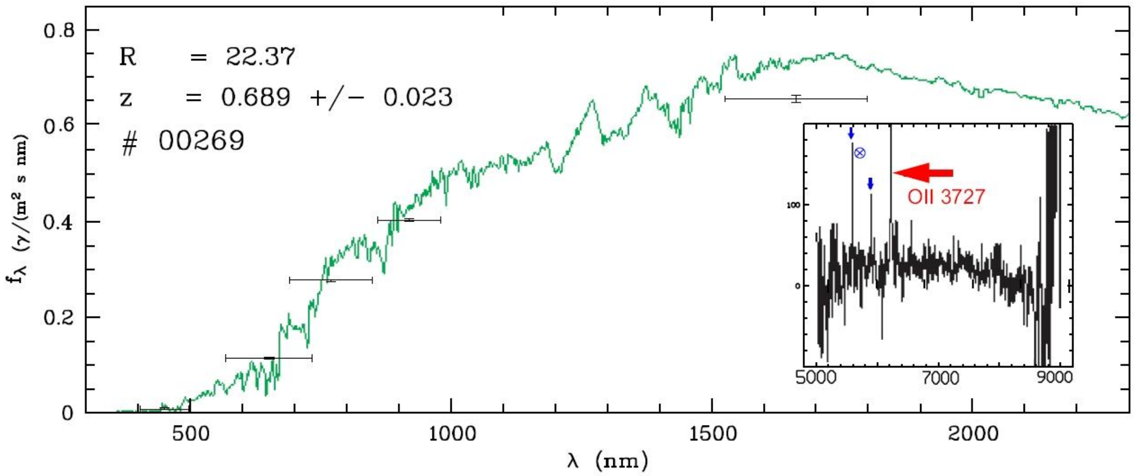

Figure 9.7: The best-fitting template spectrum for object #269 in the preliminary object catalogue. The insert shows the spectrum measured with MOSCA at the Calar Alto Observatory. The large red arrow points to the O II 3727 line which served to confirm the redshift of this galaxy to be at $z_{spec} = 0.668$ while the photometric redshift is 0.689. The other two small blue arrows indicate artifacts of the sky subtraction.

galaxy which means that no emission lines should be visible. Such a mismatch of the galaxy type can be explained by the preliminary photometry. With the full analysis a better match is expected. All other measured objects had low signal-to-noise spectra with pure continua showing no emission lines. Another colleague from the MPIA, C. Tapken, confirmed three of these continuum objects to be within a few thousand km/s of the above presented confirmed redshift. Thus this galaxy cluster cannot be confirmed yet with the available data set.

The HIROCS group has applied for observing time at the ESO Very Large Telescope (VLT) to obtain deeper imaging and imaging in additional filters on the one hand. On the other hand high-S/N multi-object spectroscopy with FORS at the VLT should help confirming ultimately the candidate's redshift with more redshifts for the galaxies. The spectroscopy is directed to measure a velocity dispersion which shall provide information about a possible cluster merger going on (see the following Section). While the imaging proposal was not successful the multi-object spectroscopy was ranked in the 3rd quartile (cat. C, 14h with FORS2).

9.2.2 Discussion

On the basis of the provisional calibration a preliminary analysis of the spatial distribution can be carried out. For this task a contour plot of the galaxy density distribution in the redshift range $0.55 < z < 0.80$ (see Fig. 9.8) was produced. The contours are derived by placing a Gaussian (FWHM: ∼300 kpc = 40 pixels at $z = 0.7$) at the galaxies positions first and after that a 2D smoothed image is created. The reduction software MIDAS provides a tool to plot contours (PLOT/CONT) using the smoothed image. As stated before the distribution of the galaxies has no marked peak as is usually seen in galaxy clusters. Often clusters are dominated by one or even two giant elliptical galaxies in their centers. In this example the brightest galaxies are not located in the center but more to the outskirts of the cluster (three red stars in Fig. 9.8). From this appearance it is evident that the cluster

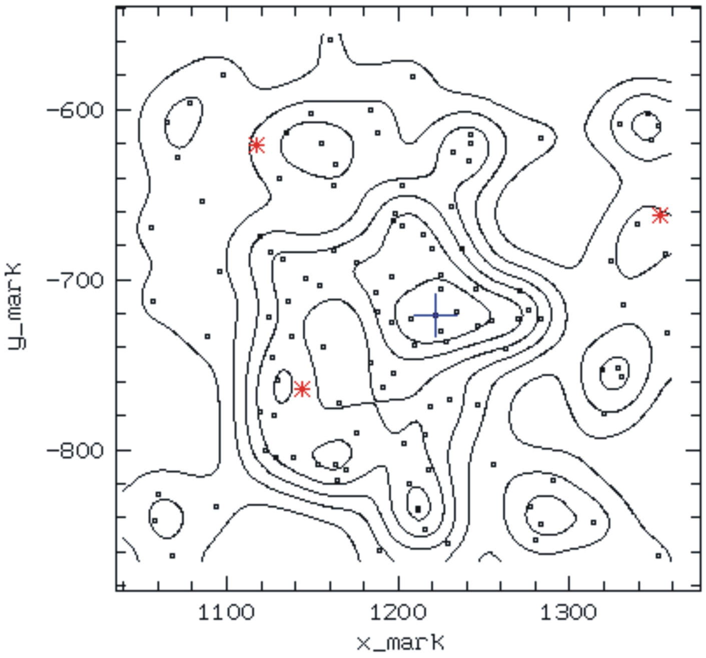

Figure 9.8: Object distribution drawn from a selection of likely cluster galaxies (little black squares). Selection: all galaxies with $0.55 < z < 0.80$ and no magnitude selection. The three brightest galaxies are marked with red star symbols ($m_H < 19.24$). The contours illustrate the galaxy density in the region of the cluster candidate. The cluster center is indicated by the large blue cross at $[\mathrm{x\_mark}, \mathrm{y\_mark}] \sim [1220'', -720'']$.

can not be in a relaxed state because the brightest galaxies are expected to populate the minimum of the gravitational potential well. Consequently this fact indicates that this cluster could be right before or in the state of a merging process of smaller constituents. However, to examine whether this is true or not more observations are needed. A deep pointing with XMM-Newton in the X-ray regime would have helped to get an insight in this respect. But also the proposal for these follow-up project was rejected by the time allocation committee.

Looking at the 3-color image the cluster candidate appears as a rather rich agglomerate of galaxies. On the basis of the preliminary object catalogue the Abell richness can be estimated roughly. The problem is that the scatter of the photometric redshifts is so large that the cluster membership is highly insecure. Nevertheless, if all objects classified as galaxies with redshifts between 0.55 and 0.80 as well as with H band magnitudes in the range $[\mathrm{m}_3, \mathrm{m}_3{+}2] = [19.14, 21.14]$ are selected, 41 objects remain in the resulting list. This number gives a hint that the possible cluster with more than 30 and less than 50 members is of richness class 0 according to the Abell richness definition. However, to draw a firm conclusion about the richness, the final reduction and calibration of the photometry has to be finished to perform a more robust analysis.

Analyzing galaxy clusters at a redshift of approximately 0.7 is important because this provides an understanding of cluster properties at an intermediate evolutionary epoch of the Universe. It is furthermore a link between the well-studied local samples to the very distant clusters at z beyond unity. In this context, the first HIROCS cluster will be part of an intermediate-redshift cluster sample at redshifts of $\sim$0.7 which will serve for comparison studies with a high-redshift cluster sample at redshifts of $\sim$1.3. These studies intend to examine the evolution of the red-sequence population and the luminosity function of galaxy clusters out to high redshifts on the basis of the HIROCS sample.

Chapter 10

Summary and outlook

Goals of the PhD project

The HIROCS survey was characterized in its main parts when the author started working for the PhD project. Three main aims guided the work presented in this doctoral thesis:

- optical observations in concert with data reduction and photometric calibration,
- refinement of the newly developed 3D galaxy cluster search method, and
- development of procedures for the evaluation of the cluster selection function

Main contributions

As part of the final survey preparations, two new large-area fields ($1^\circ \times 3^\circ$) were selected obeying the following criteria: equatorial position, absence of bright stars, and low foreground galactic extinction. One of these fields was replaced by the COSMOS field due to the public availability of Hubble Space Telescope imaging data and data in several other wavebands.
The performance of the multi-color classification scheme for the HIROCS filter set was examined with Monte-Carlo simulations. On the basis of the galaxy template library and an object catalogue from the COMBO-17 survey, the redshift accuracy δ_{z} was estimated. Resulting from these calculations, $\delta_{\mathrm{z}}/(1{+}\mathrm{z}) \sim 0.076$ at a R band magnitude of $R = 25\,\mathrm{mag}$. In addition to that, it was estimated that 51% of the early-type galaxies in the galaxy template library with R band magnitudes of $R = 25\,\mathrm{mag}$ can be re-classified with the HIROCS filter set and the depth of the exposures. These simulations showed the basic accuracies of the multi-color classification results on the basis of the HIROCS observational setup with five filters and the corresponding limiting magnitudes (R band

limit: 24.8 mag). To conclude, the aim of the project to detect distant galaxy clusters can be achieved with these specifications.

In the HIROCS 03h field, the first complete data set in all five filters is available for 1 square degree yet. Currently, the methods to handle mosaic frames are developed by H. Hippelein and H.-J. Röser. The author has carried out the data reduction of the WFI data in the B and R filters and provided the reduced frames for this data set. During the reductions of the infrared data in the H band, the first HIROCS galaxy cluster was detected on a sub-field. Guided by this discovery, H. Hippelein and the author have done the provisional photometry as well as the multi-color classification. The classification yielded an excess of galaxies at a redshift of $z \sim 0.7$. This cluster is rather rich with an approximate Abell richness class of 0. It shows no central concentration and the brightest galaxies are found towards the cluster periphery. All this is indication of a possible merging state of the system. Multi-object spectroscopy with MOSCA at the Calar Alto 3.5m telescope confirmed four galaxies to be within a few thousand km/s in velocity close to the estimated photometric redshift of the cluster (courtesy: M. Zatloukal, C. Tapken). A further multi-object spectroscopy proposal with FORS2 at the VLT to study the velocity dispersion of the cluster in detail was ranked category C and will be observed in autumn 2006.

For the detection of the galaxy clusters a new search algorithm was developed. The method comprises a 3D search using the positions in concert with the photometric redshifts and their errors from the multi-color classification. Based on this information, an estimate of the local galaxy density is determined around each object of a respected field. The 3D density estimation is done within a suitable fraction of an Abell radius on the sky and within a predefined velocity limit. Galaxy cluster candidates are identified by applying a 3σ over-density limit which is found by a Gaussian fit to the rising flank of the density distribution of all objects. The positions, redshifts, and richness of the candidates is determined in a separate procedure on the basis of the $>3\sigma$ over-densities.

The procedures to quantify the cluster selection function for HIROCS as well as COMBO-17 were developed. These comprise the simulation of artificial galaxy clusters with adequate photometric and redshift properties of the galaxies, the insertion of the clusters in the real object catalogue, and the application of the cluster search. Repeating these steps for a large number of clusters at different redshifts as well as with varying richness within a large Monte-Carlo simulation yields the selection function. The selection function characterizes the search method in terms of the ability to find clusters in a certain redshift range and within a range of richness values. Due to the lack of a calibrated HIROCS data set, the selection function could only be determined for COMBO-17. With this data set it was possible to demonstrate the capacity of the simulation procedures. The main result is the following: the recovery rate of rich clusters with $N_{gal} > 40$ exceeds 90% for the total redshift range $0.3 < z < 0.9$ examined. According to this, rich clusters should be detected, if present in the COMBO-17 fields, over the whole accessible redshift range. The sensitivity to clusters of low richness and to galaxy groups decreases with increasing redshift. Estimating redshifts and richness of the simulated clusters works well in the case these are recovered by the search algorithm. The Monte-Carlo simulation procedures for HIROCS, which include additionally the step of the multi-color classification for the simulated galaxies, are available. Once the real object catalogue from HIROCS is provided, the selection function can be determined for the redshift range $0.5 < z < 1.5$ in the same way as for COMBO-17. This will quantify the recovery rates of the HIROCS clusters at these high redshifts.

A detailed cluster search was carried out on the three fields from COMBO-17. On the basis of the COMBO-17 selection function, detected cluster candidates can be assigned with an estimated recovery rate which corresponds to the redshift and richness of the particular candidate. If the corresponding recovery rate exceeds 50%, the candidates are judged to be significant detections and can be kept for a further analysis. Applying this selection of candidates yields the following results: 11 clusters were found in the redshift range $0.3 < z < 0.6$ and 5 in the redshift range $0.6 < z < 0.9$. All cluster candidates are of low to intermediate richness. A great part of these are thus groups of galaxies rather than rich galaxy clusters. For a larger and more representative cluster sample a larger data set from a survey like HIROCS is needed. The search results presented in this thesis serve to illustrate the power of the new 3D search method.

Comparison studies between different cluster search methods provide insight into the strengths and weaknesses of the procedures. For such an investigation, the 2D Voronoi tessellation technique of Ramella et al. (2001) was applied to the CDFS to detect cluster candidates. On the basis of this 2D technique only two clusters were found which were also detected by the 3D method of this thesis. Two further Voronoi detections were either found at lower over-density (1.5σ) level of the 3D method or not found at all. This is interpreted in the first case such that the 3D method, which uses more information, is more efficient in detecting significant clusters. The second case is judged as a spurious detection by the Voronoi technique. Furthermore, the Voronoi search results do not include five clusters found by the 3D method because these do not fulfil the Voronoi detection criteria. A modified version of the Voronoi tessellation including redshift bins was tested and the results compared to those from the 3D method. Voronoi with redshift slices is, in principle, a similar technique than the 3D method because the density determination is done using the sky positions and the photometric redshifts. The inclusion of redshifts for Voronoi yields a better agreement of the search findings compared to original Voronoi approach. Five candidates from the 3D method were confirmed and this also with the same redshift. Two of the 3D candidates are not accepted for the Voronoi (with redshift

binning) cluster catalogue because these do not meet the selection criteria of this technique. Another candidate, exclusively detected by Voronoi with redshift binning, was not recognized by the 3D method because it was too close to the field border. Compared to the Voronoi tessellation with redshift binning, the 3D method presented in this thesis is slightly more efficient – it detects two more cluster candidates of low richness. The 3D method incorporates the redshift error information for all objects which is an advantage compared to the redshift binning imposed for the Voronoi approach. For a more comprehensive comparison between the Voronoi tessellation and the 3D method, a data set on a much larger sky area, like it will be provided by HIROCS, is needed. The number of clusters in the CDFS is rather low so that the statistics are poor.
To emphasize the search results in the COMBO-17 fields, a first analysis of the color-magnitude relation of an example cluster and of two stacked clusters in different redshift regimes was presented. It was shown, in both cases, that a significant fraction of the galaxy populations are made up by old, passively evolving elliptical galaxies, see van Dokkum et al. (2003). The results are consistent with the color-magnitude relations of Bell et al. (2004). For the stacked clusters, the rest-frame color of the red galaxies is bluer for the high redshift sample which can be understood also by the passive fading picture. Furthermore, the search results were compared to findings from other investigations like the structure detections of Adami et al. (2005) in the CDFS or the weak-lensing analysis of Taylor et al. (2004) in the A901/A902 field. From the former comparison study the main result was that an imaging survey yields a statistically complete view of the galaxy sample. A spectroscopic survey, in contrast, relies on object pre-selection which provides a biased view of the sample which shall be examined. The latter comparison study (weak lensing) illustrates that weak lensing is dependent on a sample of background galaxies for which photometric redshifts have to be known. This fact limits the use of the weak lensing technique for the galaxy cluster search.

Outlook

HIROCS is currently proceeding well. More than 50% of the H band data are available yet. A strategy, worked out for the observations in 2006, aims at the collection of the optical data in the fields where the infrared data are already taken. If this is successful, 6.6 square degrees will be covered until the end of 2006. The cluster search techniques are established as well as tested on the COMBO-17 data set and can be applied to the HIROCS data. However, there are future tasks which will improve the work presented in this thesis:

- Selection function determination for HIROCS:
  Blue galaxies in clusters are not distributed according to a King profile. This will

be taken into account. The assumption that clusters are circular objects is too simplifying. In future, clusters with elliptical projected galaxy distributions will be simulated to determine the selection function.

- Over-density selection:
  Up to now, a 3σ over-density limit is applied to select galaxy cluster candidates. This cut maybe very conservative and thus exclude some additional systems. As was shown by the determination of the false-discovery rate, the fraction of spurious cluster detections is close to 0 with the 3σ over-density limit. By means of the simulations for the false-discovery rate, it can be checked whether the over-density criterium can be set at lower significance. At lower significance than 3σ the number of detected clusters and also the number of spurious clusters increases. At the same time the fraction of spurious detections has to be kept below a suitable threshold. This approach has to be tested for the HIROCS detection procedure and could eventually yield another over-density cutoff criterium.

- Comparison with other cluster search techniques:
  The importance was discussed in this thesis and the comparison with the Voronoi tessellation approach was carried out. Other search techniques like the red-sequence search (2000) or the extended friends-of-friends algorithm of Botzler et al. (2004) are planned to be used for the comparison study and even beyond the comparison. The different techniques will provide different cluster samples which can be combined to yield a more comprehensive catalogue of clusters. This shall be the ultimate goal of the application of different search methods.

- Selection function for other search methods:
  To be able to judge the reliability of the search results, yielded from the application of other techniques, Monte-Carlo simulations to determine the selection function are necessary.

Concluding from the project status and the results presented in this doctoral thesis, HIROCS is facing the first application of the cluster search methods. Data on 1 square degree will be soon available for the analysis.
The following main science topics are foreseen for the galaxy evolution studies using the HIROCS cluster sample:

- study of the color-magnitude relation of stacked clusters at intermediate (z∼0.7) and high redshifts (z∼1.3),

- evolution of the red-sequence population in the redshift and local density range covered by HIROCS,

- evolution of the population mix as a function of redshift,
- follow-up observations of single clusters to study the velocity structure of clusters and cluster merging processes at high redshifts beyond unity, and
- additional filters and deeper imaging as follow-up project to probe deeper into the luminosity function of single clusters.

Appendix A

HIROCS field layout

In total four fields (see Fig. A.1 to A.4) at different positions in right ascension are the targets of HIROCS. The fields' names, positions, galactic latitude, size, and galactic extinction were listed in Table 3.1. Sect. 3.1 explains the selection procedure of the fields. To supplement this, the detailed field layout is shown in the following.

All fields are arranged from 1 square degree patches of which two or three overlap. The 1 square degree patches (termed A, B, C, respectively) consist of 16 sub-fields. The size of these sub-fields is dictated by the field-of-view of the LAICA detectors ($15.4' \times 15.4'$). See Sect. 3.2 for the instrumentation details. The numbering of the sub-fields is related to the pointings of the LAICA instrument. Pointings number 1 to 4 cover the 1 square degree patch A, 5 to 8 patch B, and 9 to 12 patch C, respectively. "a" to "d" denote the four LAICA detectors. The four LAICA pointings to cover 1 square degree are indicated as a showcase by the colored crosses in the sub-fields [4a, 3b, 2c, 1d], [8a, 7b, 6c, 5d], and [12a, 11b, 10c, 9d] shown in Fig.A.1.

In the case of the MUNICS and newly selected HIROCS 22h fields the 1 square degree patches are not aligned. This is caused by the selection criterion to avoid bright stars. Such bright stars are flagged with their visual brightness in the Figures.

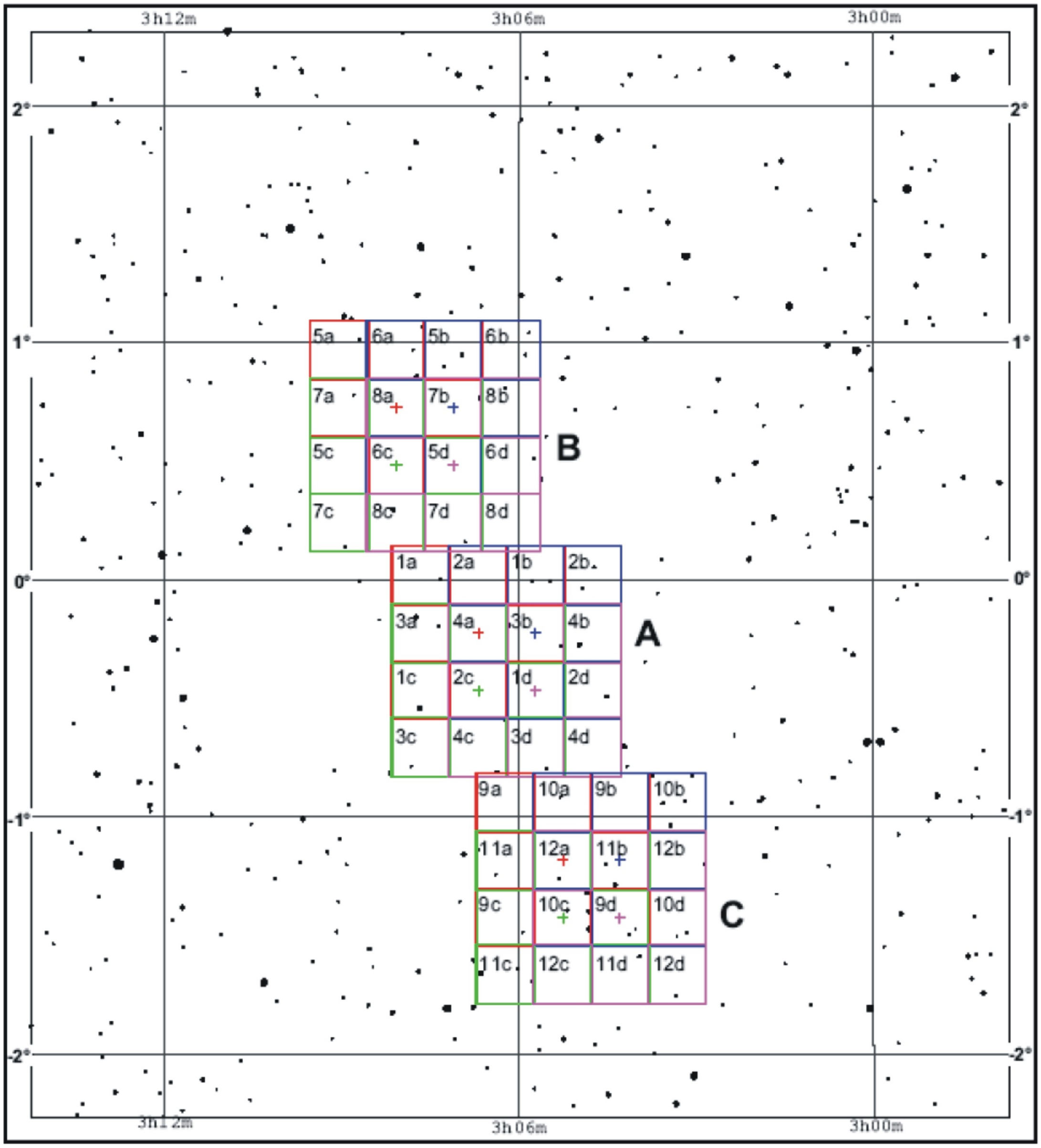

Figure A.1: HIROCS 03h field or the "MUNICS" field: The "MUNICS-S2F1" field is found in patch A, sub-field 2a. The first HIROCS cluster was found in patch A, sub-field 2d.

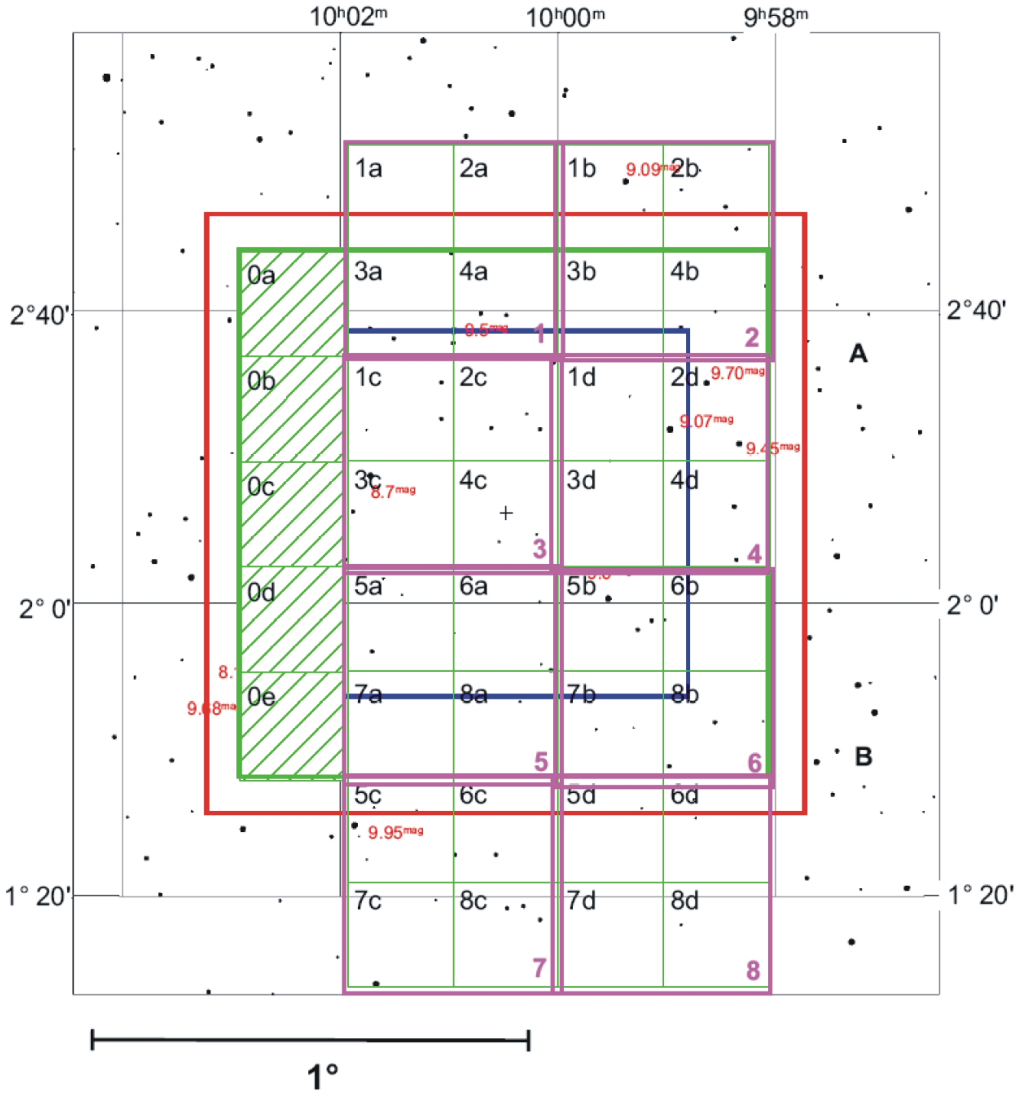

Figure A.2: HIROCS 10h field or the "COSMOS" field: The field covered by the COSMOS survey is marked by the red square (2 square degrees) and the blue square is covered with the VIMOS instrument at the VLT. The HIROCS coverage with LAICA (filters i and z) is shown as the green square (hashed) and with the WFI (filters B and R) is shown as the magenta pattern of squares.

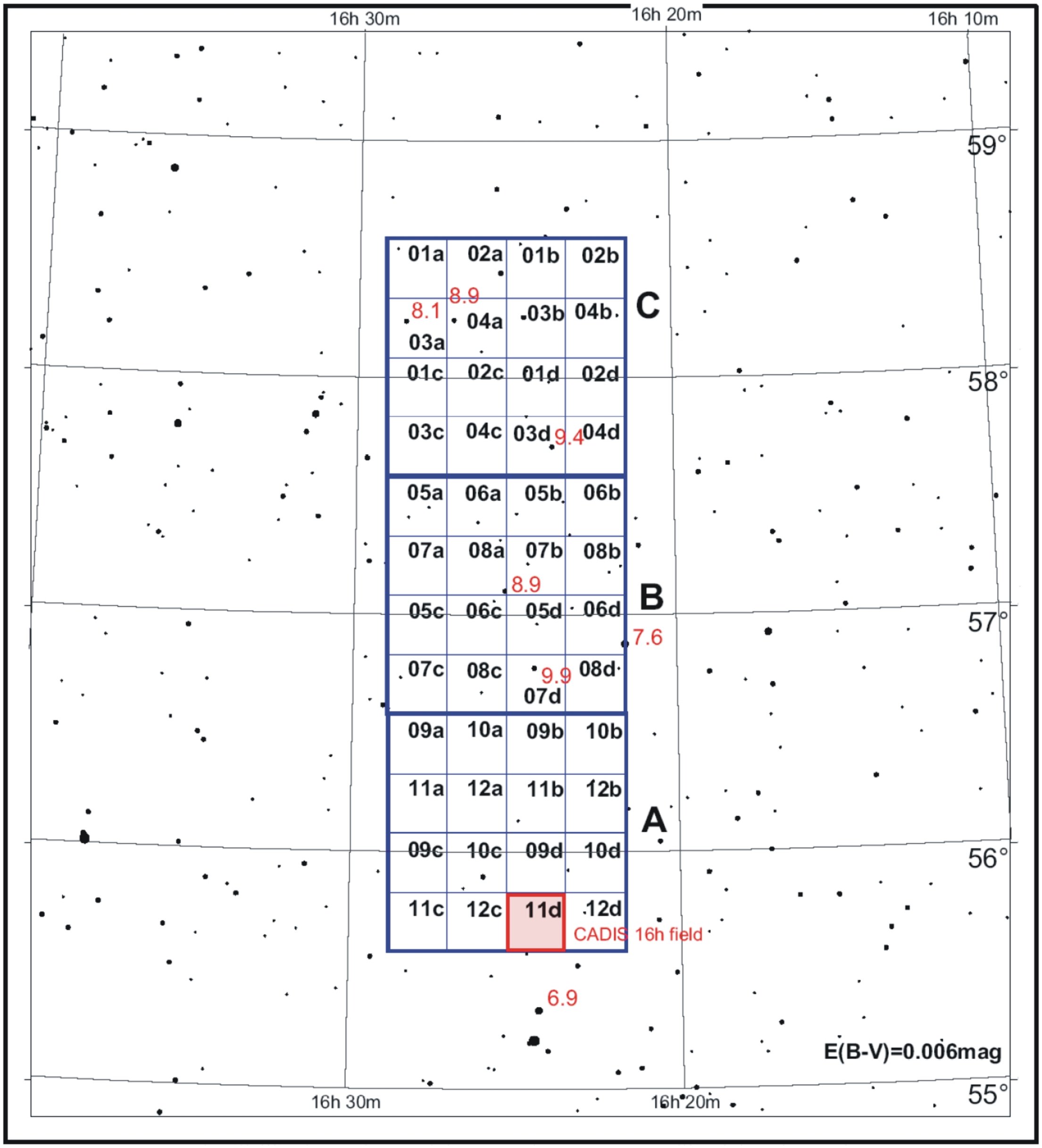

Figure A.3: HIROCS 16h field or "CADIS" field: The "CADIS-16h" field is located in the sub-field 11d (shaded).

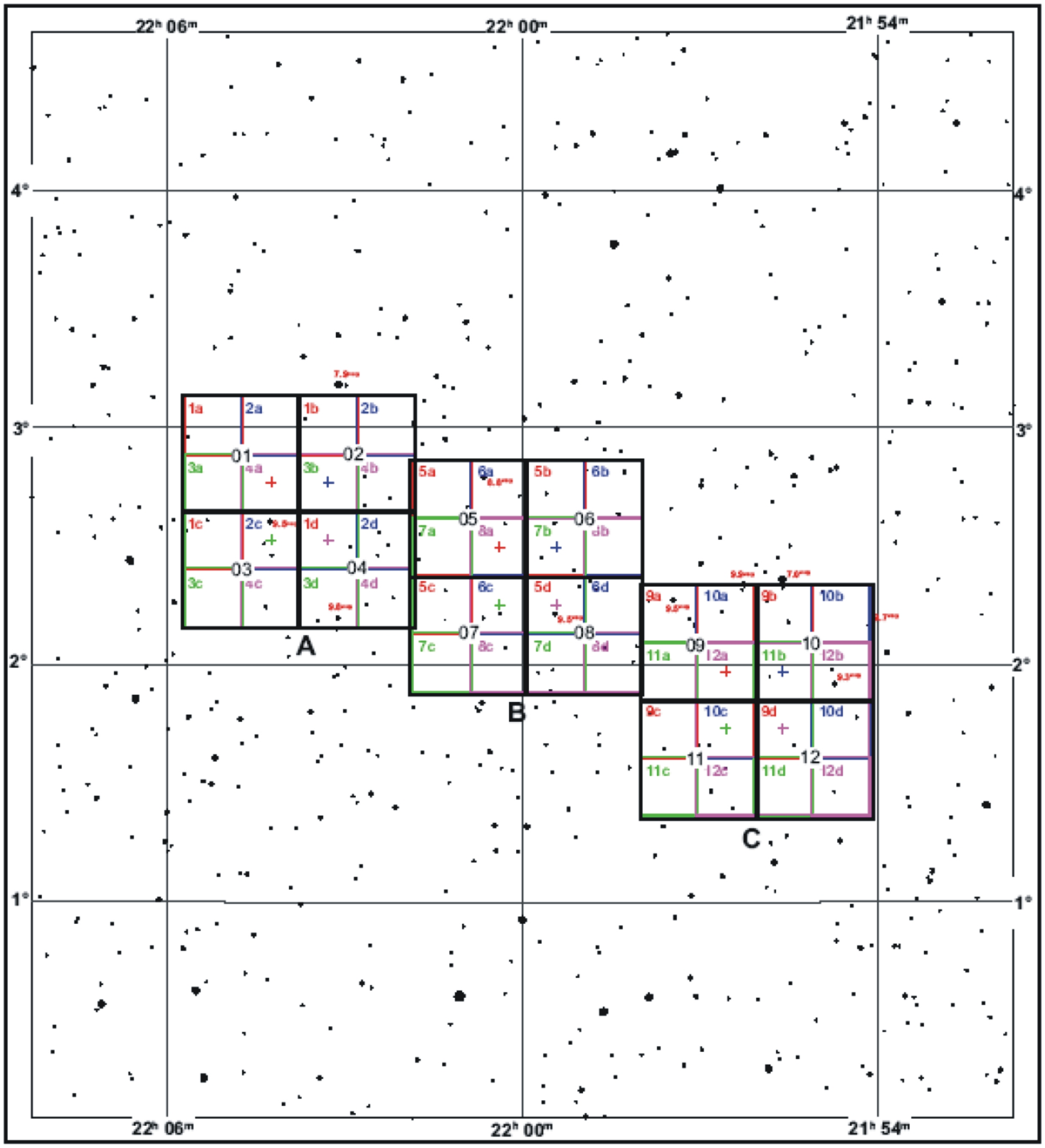

Figure A.4: HIROCS 22h field: this field was newly selected by the author.

Appendix B

HIROCS spectrophotometric standard stars

On the following pages are shown the results for the first seven calibrated tertiary standard stars in the 03h field. Details about how the calibration was done can be found in Chapter 3. The plots show the instrumental magnitudes derived by convolving the best-matching Pickles (1998) spectrum with the transmission curves of the SDSS and 2MASS filters. These are compared with the measured values from the SDSS (u, g, r, i, z) and the 2MASS (J, H, K) surveys. There are some offsets in u, J, and K. The matching was done to yield a good agreement in the optical bands (except u) and the H band because the corresponding wavelength ranges are covered by the HIROCS filters.

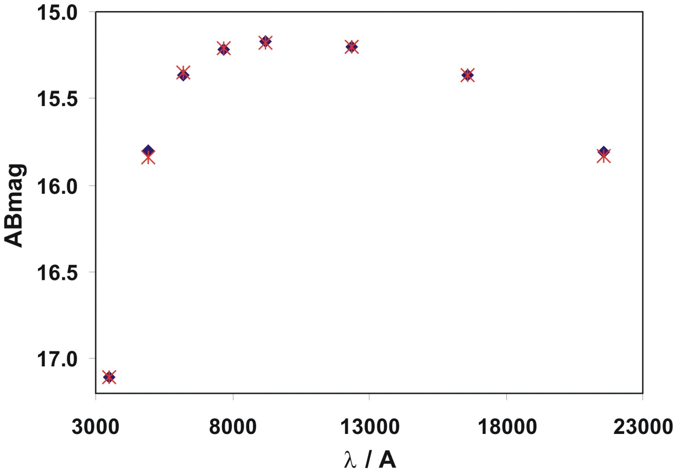

Figure B.1: Absolute calibration for standard star #1 in the HIROCS 03h field. Spectral type: G2V. Dark blue diamonds: AB magnitudes resulting from the spectral matching to the Pickles (1998) library and the convolution with the filter transmission curves for the SDSS (u, g, r, i, z) as well as 2MASS (J, H, K) filters. Red star symbols: measured ABmag for this star in the SDSS and the 2MASS filters.

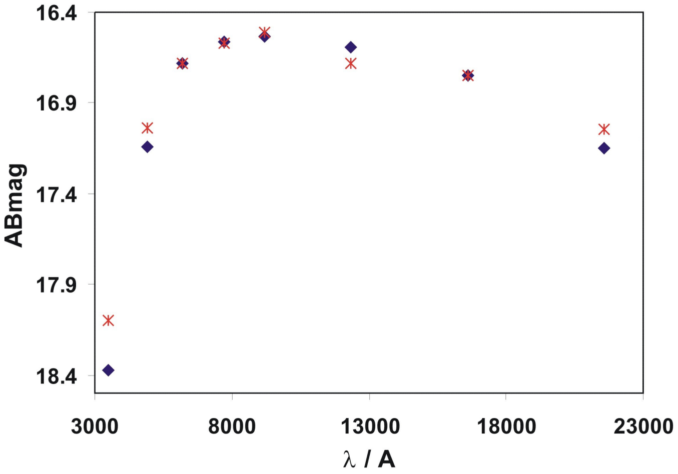

Figure B.2: Absolute calibration for standard star #2 in the HIROCS 03h field. Spectral type: G0V. Details see B.1.

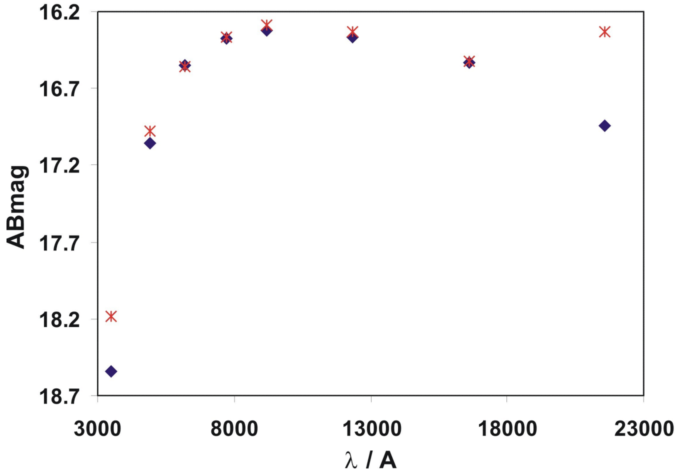

Figure B.3: Absolute calibration for standard star #3 in the HIROCS 03h field. Spectral type: G6.5V. Details see B.1.

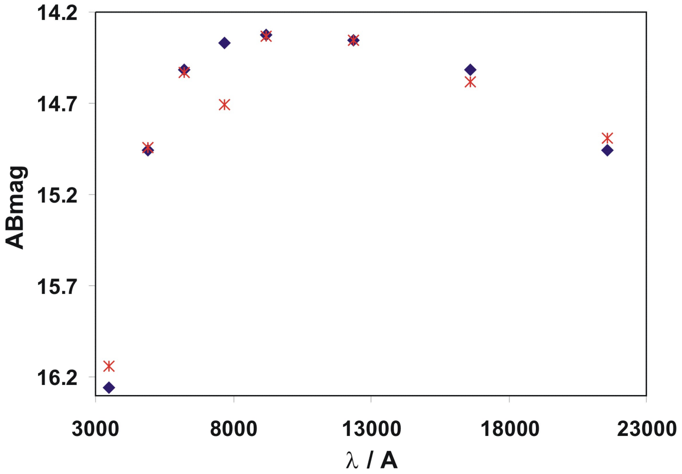

Figure B.4: Absolute calibration for standard star #4 in the HIROCS 03h field. Spectral type: G2V. Details see B.1. Note: Object is saturated in *i* of the SDSS measurements.

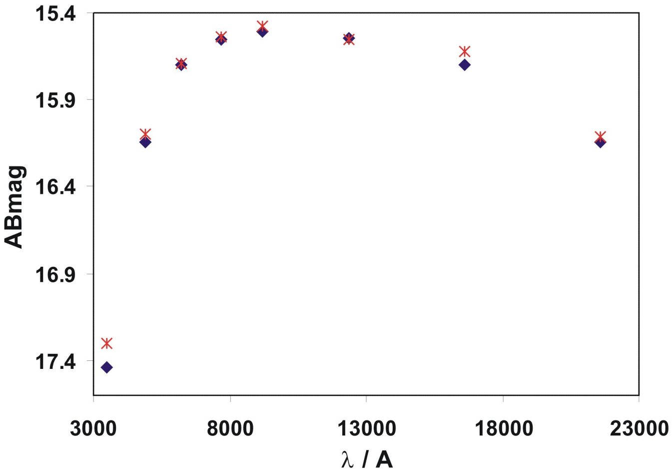

Figure B.5: Absolute calibration for standard star #5 in the HIROCS 03h field. Spectral type: G2V. Details see B.1.

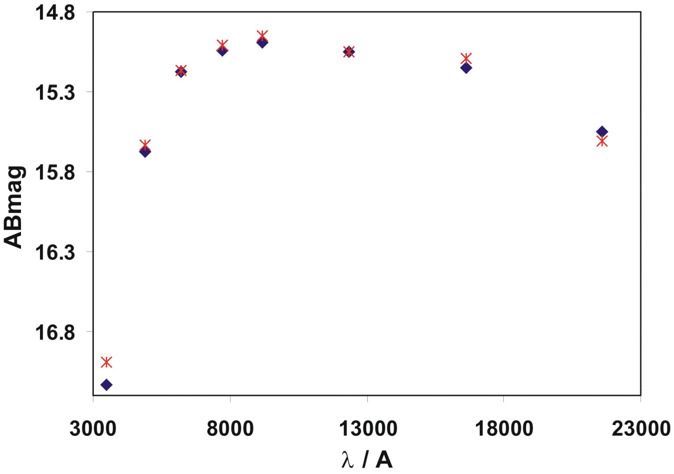

Figure B.6: Absolute calibration for standard star #6 in the HIROCS 03h field. Spectral type: G5V. Details see B.1.

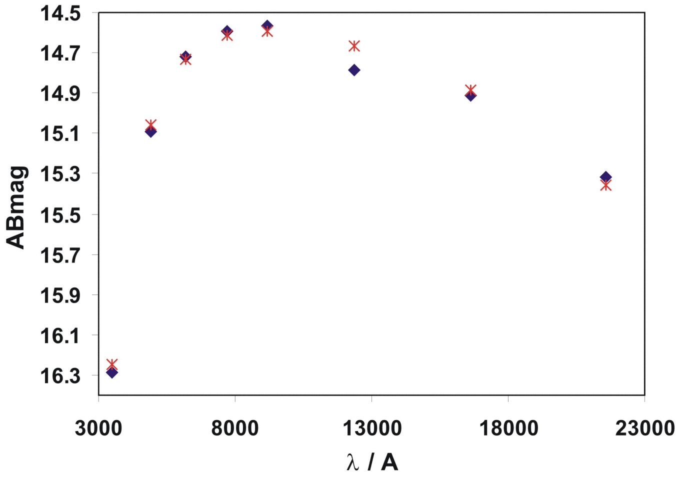

Figure B.7: Absolute calibration for standard star #7 in the HIROCS 03h field. Spectral type: F6V. Details see B.1.

Appendix C

Photometric systems

The following is taken from the PhD thesis of C. Wolf (Wolf, 1998):
In observational astronomy the definition of brightness is based on a logarithmic scale of radiation flux F in units of magnitudes. An object which is 1 mag fainter than another object emits accordingly a factor of 2.5 less flux, 5 mag correspond to a factor 100 in flux. Besides the historical definition of the zero-points of the magnitude scale, today several other physically motivated definitions are in use. To clarify the differences this section lists all definitions.
The A0 star Vega with brightness 0 serves as the reference object for the calculation of the magnitude zero-point:

$$m = -2.5 \log \frac{F_{object}}{F_{Vega}} \tag{C.1}$$

But Vega's spectrum viewed as flux versus wavelength has a complicated shape and has been arbitrarily chosen as the reference object.
In the 60's the first physical magnitude system was introduced by J.B. Oke, see Oke (1964), Oke (1965), and Oke (1974):

$$AB\mathrm{mag} = -2.5 \log F_\nu - 48.60 \qquad \text{with } F_\nu \text{ in erg cm}^{-2}\text{ s}^{-1}\text{ Hz}^{-1}. \tag{C.2}$$

Later on the ST magnitude scale was invented (Walsh, 1995):

$$ST\mathrm{mag} = -2.5 \log F_\lambda - 21.10 \qquad \text{with } F_\lambda \text{ in erg cm}^{-2}\text{ s}^{-1}\text{ Å}^{-1}. \tag{C.3}$$

ST stands for Space Telescope.
Based on the survey work at the MPIA with CADIS and COMBO-17, the flux values of HIROCS are given always as photon count rates F_{phot} in units of γ m^{-2} s^{-1} nm^{-1}:

$$CD\mathrm{mag} = -2.5 \log F_{phot} + 20.01 \qquad \text{with } F_{phot} \text{ in } \gamma \text{ m}^{-2}\text{ s}^{-1}\text{ nm}^{-1}. \tag{C.4}$$

CD stems from CADIS. The CDmag is the average of the AB and the STmag:

$$\nu^2 \, F_\nu \propto \nu \, F_{phot} \propto F_\lambda \tag{C.5}$$

$$\nu \, F_\nu = hc \, F_{phot} = \lambda \, F_\lambda . \tag{C.6}$$

The definition is chosen such that the zero-points of all systems intersect at 548 nm. Oke's choice of the zero-point gave rise to the common reference point. The motivation from CADIS to use the CDmag system was the following: at 548 nm Vega has a flux of $1.01\,10^8\,\gamma\,\mathrm{m}^{-2}\,\mathrm{s}^{-1}\,\mathrm{nm}^{-1}$ meaning that a flux of $1\,\gamma\,\mathrm{m}^{-2}\,\mathrm{s}^{-1}\,\mathrm{nm}^{-1}$ corresponds to a brightness of 20.01 mag.

Appendix D

Redshift and velocity

For the counting of physically associated close galaxies in 3D space, a relation for the velocity difference between either two objects is needed. Perry & O'Dell (1978) provided a formula that describes the velocity difference of two physically bound objects at cosmological distances which is adopted for the search algorithm:

$$\beta = \left|\frac{\mathrm{v}}{\mathrm{c}}\right| = \left|\frac{(1+\mathrm{z}_1)^2 - (1+\mathrm{z}_0)^2}{(1+\mathrm{z}_1)^2 + (1+\mathrm{z}_0)^2}\right| \leq \left|\left(\frac{\mathrm{v}}{\mathrm{c}}\right)_{\mathrm{lim}}\right| \tag{D.1}$$

z_0 is the photometric redshift of the object around which the search aperture is drawn and for z_1 the redshifts of all other objects are inserted. $\frac{\mathrm{v}}{\mathrm{c}}_{\mathrm{lim}}$ is the velocity limit.
It is important to take into account the photometric redshift errors. Objects with redshifts and a corresponding velocity outside the velocity limit can still be associated with a given object when the redshift/velocity errors are large. Thus the error margin for the velocity limit $\left(\frac{\mathrm{v}}{\mathrm{c}}\right)_{\mathrm{lim}}$ corresponding to the redshift errors of two given objects is calculated in the following:

$$\sigma_\beta = \sqrt{\left(\frac{\partial\beta}{\partial\mathrm{z}_1}\right)^2 \sigma_{\mathrm{z}_1}^2 + \left(\frac{\partial\beta}{\partial\mathrm{z}_0}\right)^2 \sigma_{\mathrm{z}_0}^2} \tag{D.2}$$

After determining the partial derivatives this error is:

$$\sigma_\beta = \frac{2}{\mathrm{z}_1^2 + \mathrm{z}_0^2} \sqrt{\mathrm{z}_1 \mathrm{z}_0^2 \sigma_{\mathrm{z}_1}^2 - \mathrm{z}_1^2 \mathrm{z}_0 \sigma_{\mathrm{z}_0}^2} \tag{D.3}$$

From a fixed velocity limit the corresponding difference in redshifts can be calculated, too. Solving equation D.1 for the redshift z_1 of the object 1, which is examined whether it is close to object 0, yields:

$$\mathrm{z}_1 = (1 + \mathrm{z}_0)\sqrt{\frac{1+\beta}{1-\beta}} - 1 \tag{D.4}$$

Now two cases can be distinguished which account for the fact that β can also have negative values:

$$\mathrm{z}_{\mathrm{I}} = (1 + \mathrm{z}_0)\sqrt{\frac{1+|\beta|}{1-|\beta|}} - 1 \qquad \text{for} \quad \beta = +\beta \tag{D.5}$$

$$\mathrm{z}_{\mathrm{II}} = (1 + \mathrm{z}_0)\sqrt{\frac{1-|\beta|}{1+|\beta|}} - 1 \qquad \text{for} \quad \beta = -\beta \tag{D.6}$$

Combing these two conditions the difference in redshift which corresponds to a certain velocity difference β is calculated by:

$$\Delta\mathrm{z} = \mathrm{z}_{\mathrm{II}} - \mathrm{z}_{\mathrm{I}} = (1 + \mathrm{z}_0)\left(\sqrt{\frac{1+\beta}{1-\beta}} - \sqrt{\frac{1-\beta}{1+\beta}}\right) \tag{D.7}$$

Bibliography

Abell, G. O.: 1958, *The Distribution of Rich Clusters of Galaxies.*, ApJS **3**, 211

Abell, G. O., Corwin, H. G., & Olowin, R. P.: 1989, *A catalog of rich clusters of galaxies*, ApJS **70**, 1

Adami, C., Mazure, A., Ilbert, O., Cappi, A., Bottini, D., Garilli, B., Le Brun, V., Le Fèvre, O., Maccagni, D., Picat, J. P., Scaramella, R., Scodeggio, M., Tresse, L., Vettolani, G., Zanichelli, A., Arnaboldi, M., Arnouts, S., Bardelli, S., Bolzonella, M., Charlot, S., Ciliegi, P., Contini, T., Covone, G., Foucaud, S., Franzetti, P., Gavignaud, I., Guzzo, L., Iovino, A., Lauger, S., McCracken, H. J., Marano, B., Marinoni, C., Meneux, B., Merighi, R., Paltani, S., Pellò, R., Pollo, A., Pozzetti, L., Radovich, M., Zamorani, G., Zucca, E., Bondi, M., Bongiorno, A., Busarello, G., Gregorini, L., Mathez, G., Mellier, Y., Merluzzi, P., Ripepi, V., & Rizzo, D.: 2005, *The Vimos VLT deep survey: compact structures in the CDFS*, A&A **443**, 805

Adami, C., Mazure, A., Katgert, P., & Biviano, A.: 1998, *The ESO nearby Abell cluster survey. VII. Galaxy density profiles of rich clusters of galaxies*, A&A **336**, 63

Adami, C., Mazure, A., Ulmer, M. P., & Savine, C.: 2001, *Central matter distributions in rich clusters of galaxies from* $z\sim0$ *to* $z\sim0.5$, A&A **371**, 11

Andreon, S.: 2004, *Galaxy luminosity evolution: How much is due to model choice?*, A&A **416**, 865

Andreon, S., Lobo, C., & Iovino, A.: 2004, *Extending the Butcher-Oemler effect up to z˜ 0.7*, MNRAS **349**, 889

Bahcall, N. A.: 1999, in A. Dekel and J. P. Ostriker (eds.), *Formation of Structure in the Universe*, pp 135–+

Bartelmann, M. & White, S. D. M.: 2002, *Cluster detection from surface-brightness fluctuations in SDSS data*, A&A **388**, 732

Bell, E. F., Wolf, C., Meisenheimer, K., Rix, H.-W., Borch, A., Dye, S., Kleinheinrich, M., Wisotzki, L., & McIntosh, D. H.: 2004, *Nearly 5000 Distant Early-Type Galaxies in COMBO-17: A Red Sequence and Its Evolution since* $z\sim1$, ApJ **608**, 752

Belloni, P., Bruzual, A. G., Thimm, G. J., & Röser, H.-J.: 1995, *Detectability and in-*

cidence of E+A galaxies in the distance cluster C10930+472 (z = 0.41), A&A **297**, 61

Belloni, P. & Röser, H.-J.: 1996, *Galaxy population in distant galaxy clusters. I. CL 0939+472 (z=0.41) and CL 0016+161 (z=0.54).*, A&ASS **118**, 65

Bertin, E. & Arnouts, S.: 1996, *SExtractor: Software for source extraction.*, A&ASS **117**, 393

Botzler, C.: 2004, *Ph.D. thesis*, LMU München

Botzler, C. S., Snigula, J., Bender, R., & Hopp, U.: 2004, *Finding structures in photometric redshift galaxy surveys: an extended friends-of-friends algorithm*, MNRAS **349**, 425

Bronstein, I. N., Semendjajew, K. A., Musiol, G., & Mühlig, H.: 1999, *Taschenbuch der Mathematik*, Verlag Harri Deutsch AG, Frankfurt am Main, Thun

Butcher, H. & Oemler, A.: 1984, *The evolution of galaxies in clusters. V - A study of populations since Z approximately equal to 0.5*, ApJ **285**, 426

Christlein, D. & Zabludoff, A. I.: 2003, *Galaxy Luminosity Functions from Deep Spectroscopic Samples of Rich Clusters*, ApJ **591**, 764

Cimatti, A., Mignoli, M., Daddi, E., Pozzetti, L., Fontana, A., Saracco, P., Poli, F., Renzini, A., Zamorani, G., Broadhurst, T., Cristiani, S., D'Odorico, S., Giallongo, E., Gilmozzi, R., & Menci, N.: 2002, *The K20 survey. III. Photometric and spectroscopic properties of the sample*, A&A **392**, 395

Dalton, G. B., Maddox, S. J., Sutherland, W. J., & Efstathiou, G.: 1997, *The APM Galaxy Survey - V. Catalogues of galaxy clusters*, MNRAS **289**, 263

Dressler, A.: 1980, *Galaxy morphology in rich clusters - Implications for the formation and evolution of galaxies*, ApJ **236**, 351

Drory, N., Feulner, G., Bender, R., Botzler, C. S., Hopp, U., Maraston, C., Mendes de Oliveira, C., & Snigula, J.: 2001, *The Munich Near-Infrared Cluster Survey - I. Field selection, object extraction and photometry*, MNRAS **325**, 550

Elston, R. J., Gonzalez, A. H., McKenzie, E., Brodwin, M., Brown, M. J. I., Cardona, G., Dey, A., Dickinson, M., Eisenhardt, P. R., Jannuzi, B. T., Lin, Y.-T., Mohr, J. J., Raines, S. N., Stanford, S. A., & Stern, D.: 2006, *The FLAMINGOS Extragalactic Survey*, ApJ **639**, 816

Faber, S. M., Willmer, C. N. A., Wolf, C., Koo, D. C., Weiner, B. J., Newman, J. A., Im, M., Coil, A. L., Conroy, C., Cooper, M. C., & et al.: 2006, *Galaxy luminosity functions zo z$\sim$1: DEEP2 vs. COMBO-17 and implications for red galaxy formation*, Mon. Not. R. Astron. Soc., in prep.

Faßbender, R.: 2003, *Diploma thesis*, University of Heidelberg

Finlator, K., Ivezić, Ž., Fan, X., Strauss, M. A., Knapp, G. R., Lupton, R. H., Gunn, J. E., Rockosi, C. M., Anderson, J. E., Csabai, I., Hennessy, G. S., Hindsley, R. B., McKay, T. A., Nichol, R. C., Schneider, D. P., Smith, J. A., York, D. G., & the SDSS Collaboration: 2000, *Optical and Infrared Colors of Stars Observed by the Two Micron All Sky Survey and the Sloan Digital Sky Survey*, AJ **120**, 2615

Fioc, M. & Rocca-Volmerange, B.: 1997, *PEGASE: a UV to NIR spectral evolution model of galaxies. Application to the calibration of bright galaxy counts.*, A&A **326**, 950

Fruchter, A. S. & Hook, R. N.: 2002, *Drizzle: A Method for the Linear Reconstruction of Undersampled Images*, PASP **114**, 144

Gal, R. R., de Carvalho, R. R., Lopes, P. A. A., Djorgovski, S. G., Brunner, R. J., Mahabal, A., & Odewahn, S. C.: 2003, *The Northern Sky Optical Cluster Survey. II. An Objective Cluster Catalog for 5800 Square Degrees*, AJ **125**, 2064

Gilli, R., Cimatti, A., Daddi, E., Hasinger, G., Rosati, P., Szokoly, G., Tozzi, P., Bergeron, J., Borgani, S., Giacconi, R., Kewley, L., Mainieri, V., Mignoli, M., Nonino, M., Norman, C., Wang, J., Zamorani, G., Zheng, W., & Zirm, A.: 2003, *Tracing the Large-Scale Structure in the Chandra Deep Field South*, ApJ **592**, 721

Gladders, M. D. & Yee, H. K. C.: 2000, *A New Method For Galaxy Cluster Detection. I. The Algorithm*, AJ **120**, 2148

Goto, T., Sekiguchi, M., Nichol, R. C., Bahcall, N. A., Kim, R. S. J., Annis, J., Ivezić, Ž., Brinkmann, J., Hennessy, G. S., Szokoly, G. P., & Tucker, D. L.: 2002, *The Cut-and-Enhance Method: Selecting Clusters of Galaxies from the Sloan Digital Sky Survey Commissioning Data*, AJ **123**, 1807

Hamana, T.: 2005, *http://www.noao.edu/meetings/subaru/Session-4/Hamana.pdf*

Hamuy, M., Walker, A. R., Suntzeff, N. B., Gigoux, P., Heathcote, S. R., & Phillips, M. M.: 1992, *Southern spectrophotometric standards.*, PASP **104**, 533

Hogg, D.: 1999, *Distance measures in cosmology*, astro-ph/9905116

Hogg, D., Baldry, I. K., & Blanton, M. R. Eisenstein, D. J.: 2002, *The K correction*, astro-ph/0210394

Horne, K.: 1986, *An optimal extraction algorithm for CCD spectroscopy*, PASP **98**, 609

Kauffmann, G., Colberg, J. M., Diaferio, A., & White, S. D. M.: 1999, *Clustering of galaxies in a hierarchical universe - I. Methods and results at z=0*, MNRAS **303**, 188

Kiang, T.: 1966, *Random Fragmentation in Two and Three Dimensions*, Zeitschrift fur Astrophysics **64**, 433

Kim, R. S. J., Kepner, J. V., Postman, M., Strauss, M. A., Bahcall, N. A., Gunn, J. E., Lupton, R. H., Annis, J., Nichol, R. C., Castander, F. J., Brinkmann, J., Brunner, R. J., Connolly, A., Csabai, I., Hindsley, R. B., Ivezić, Ž., Vogeley, M. S., & York, D. G.: 2002, *Detecting Clusters of Galaxies in the Sloan Digital Sky Survey. I. Monte Carlo Comparison of Cluster Detection Algorithms*, AJ **123**, 20

King, I. R.: 1968, *The Probable Ages of the Oldest Open Clusters*, ApJ **151**, L59+

Kovács, Z.: 2005, *Ph.D. thesis*, University of Heidelberg

Lawrence, I. R., Warren, S. J., Almaini, O., Edge, A., Hambly, N. C., Jameson, R. F., Lucas, P., Casali, M., Adamson, A., Dye, S., Emerson, J. P., Foucaud, S., Hewett, P., Hirst, P., Hodgkin, S., Irwin, M., Lodieu, N., McMahon, R. G., Simpson, C., Smail, I., Mortlock, D., & Folger, M.: 2006, *The UKIRT Infrared Deep Sky Survey (UKIDSS)*, astro-ph/0604426

Le Fèvre, O., Vettolani, G., Paltani, S., Tresse, L., Zamorani, G., Le Brun, V., Moreau, C., Bottini, D., Maccagni, D., Picat, J. P., Scaramella, R., Scodeggio, M., Zanichelli, A., Adami, C., Arnouts, S., Bardelli, S., Bolzonella, M., Cappi, A., Charlot, S., Contini, T., Foucaud, S., Franzetti, P., Garilli, B., Gavignaud, I., Guzzo, L., Ilbert, O., Iovino, A., McCracken, H. J., Mancini, D., Marano, B., Marinoni, C., Mathez, G., Mazure, A., Meneux, B., Merighi, R., Pellò, R., Pollo, A., Pozzetti, L., Radovich, M., Zucca, E., Arnaboldi, M., Bondi, M., Bongiorno, A., Busarello, G., Ciliegi, P., Gregorini, L., Mellier, Y., Merluzzi, P., Ripepi, V., & Rizzo, D.: 2004, *The VIMOS VLT Deep Survey. Public release of 1599 redshifts to* $I_{AB} \leq 24$ *across the Chandra Deep Field South*, A&A **428**, 1043

Lopes, P. A. A., de Carvalho, R. R., Capelato, H. V., Gal, R. R., Djorgovski, S. G., Brunner, R. J., Odewahn, S. C., & Mahabal, A. A.: 2006, *X-ray Galaxy Clusters in NoSOCS I. Substructure and the Correlation of Optical and X-ray Properties*, astro-ph/0605292

Lopes, P. A. A., de Carvalho, R. R., Gal, R. R., Djorgovski, S. G., Odewahn, S. C., Mahabal, A. A., & Brunner, R. J.: 2004, *The Northern Sky Optical Cluster Survey. IV. An Intermediate-Redshift Galaxy Cluster Catalog and the Comparison of Two Detection Algorithms*, AJ **128**, 1017

Miller, C. J., Nichol, R. C., Reichart, D., Wechsler, R. H., Evrard, A. E., Annis, J., McKay, T. A., Bahcall, N. A., Bernardi, M., Boehringer, H., Connolly, A. J., Goto, T., Kniazev, A., Lamb, D., Postman, M., Schneider, D. P., Sheth, R. K., & Voges, W.: 2005, *The C4 Clustering Algorithm: Clusters of Galaxies in the Sloan Digital Sky Survey*, AJ **130**, 968

Mohr, J.: 2005, *http://www.mpia-hd.mpg.de/ringberg-clusters/Vortraege/Mohr-Ringberg-partial.pdf*

Monet, D. G., Levine, S. E., Canzian, B., Ables, H. D., Bird, A. R., Dahn, C. C., Guetter, H. H., Harris, H. C., Henden, A. A., Leggett, S. K., Levison, H. F., Luginbuhl, C. B., Martini, J., Monet, A. K. B., Munn, J. A., Pier, J. R., Rhodes, A. R., Riepe, B., Sell, S., Stone, R. C., Vrba, F. J., Walker, R. L., Westerhout, G., Brucato, R. J., Reid, I. N., Schoening, W., Hartley, M., Read, M. A., & Tritton, S. B.: 2003, *The USNO-B Catalog*, AJ **125**, 984

Mullis, C. R., Rosati, P., Lamer, G., Böhringer, H., Schwope, A., Schuecker, P., & Fassbender, R.: 2005, *Discovery of an X-Ray-luminous Galaxy Cluster at z=1.4*, ApJL

623, L85

Oke, J. B.: 1964, *Photoelectric Spectrophotometry of Stars Suitable for Standards.*, ApJ **140**, 689

Oke, J. B.: 1965, *Absolute Spectral Energy Distributions in Stars*, ARA&A **3**, 23

Oke, J. B.: 1974, *Absolute Spectral Energy Distributions for White Dwarfs*, ApJS **27**, 21

Oke, J. B.: 1990, *Faint spectrophotometric standard stars*, AJ **99**, 1621

Paolillo, M., Andreon, S., Longo, G., Puddu, E., Gal, R. R., Scaramella, R., Djorgovski, S. G., & de Carvalho, R.: 2001, *Luminosity function of clusters of galaxies*, A&A **367**, 59

Pei, Y. C.: 1992, *Interstellar dust from the Milky Way to the Magellanic Clouds*, ApJ **395**, 130

Pen, U.-L.: 1999, *Analytical Fit to the Luminosity Distance for Flat Cosmologies with a Cosmological Constant*, ApJS **120**, 49

Perry, J. J. & O'Dell, S. L.: 1978, *On the correlation between the absolute magnitudes of quasi-stellar objects and the velocities of ejected gas*, A&A **62**, 229

Pickles, A. J.: 1998, *A Stellar Spectral Flux Library: 1150-25000 Å*, PASP **110**, 863

Poggianti, B. M.: 1997, *K and evolutionary corrections from UV to IR*, A&ASS **122**, 399

Poggianti, B. M. & Barbaro, G.: 1996, *Starbursts and the Butcher-Oemler effect in galaxy clusters.*, A&A **314**, 379

Popesso, P., Biviano, A., Böhringer, H., & Romaniello, M.: 2006, *RASS-SDSS Galaxy cluster survey. IV. A ubiquitous dwarf galaxy population in clusters*, A&A **445**, 29

Postman, M., Franx, M., Cross, N. J. G., Holden, B., Ford, H. C., Illingworth, G. D., Goto, T., Demarco, R., Rosati, P., Blakeslee, J. P., Tran, K.-V., Benítez, N., Clampin, M., Hartig, G. F., Homeier, N., Ardila, D. R., Bartko, F., Bouwens, R. J., Bradley, L. D., Broadhurst, T. J., Brown, R. A., Burrows, C. J., Cheng, E. S., Feldman, P. D., Golimowski, D. A., Gronwall, C., Infante, L., Kimble, R. A., Krist, J. E., Lesser, M. P., Martel, A. R., Mei, S., Menanteau, F., Meurer, G. R., Miley, G. K., Motta, V., Sirianni, M., Sparks, W. B., Tran, H. D., Tsvetanov, Z. I., White, R. L., & Zheng, W.: 2005, *The Morphology-Density Relation in z ˜ 1 Clusters*, ApJ **623**, 721

Postman, M., Lubin, L. M., Gunn, J. E., Oke, J. B., Hoessel, J. G., Schneider, D. P., & Christensen, J. A.: 1996, *The Palomar Distant Clusters Survey. I. The Cluster Catalog*, AJ **111**, 615

Ramella, M., Boschin, W., Fadda, D., & Nonino, M.: 2001, *Finding galaxy clusters using Voronoi tessellations*, A&A **368**, 776

Ramella, M., Geller, M. J., Pisani, A., & da Costa, L. N.: 2002, *The UZC-SSRS2 Group Catalog*, AJ **123**, 2976

Röser, H.-J., Hippelein, H. H., & Wolf, C.: 2004, in J. S. Mulchaey, A. Dressler, and A. Oemler (eds.), *Clusters of Galaxies: Probes of Cosmological Structure and Galaxy*

Evolution

Röser, H.-J. & Meisenheimer, K.: 1991, *The synchrotron light from the jet of 3C 273*, A&A **252**, 458

Schechter, P.: 1976, *An analytic expression for the luminosity function for galaxies.*, ApJ **203**, 297

Schlegel, D. J., Finkbeiner, D. P., & Davis, M.: 1998, *Maps of Dust Infrared Emission for Use in Estimation of Reddening and Cosmic Microwave Background Radiation Foregrounds*, ApJ **500**, 525

Schücker, P.: 2005, *New Cosmology with Clusters of Galaxies*, astro-ph/0502234

Shectman, S. A.: 1985, *Clusters of galaxies from the Shane-Wirtanen counts*, ApJS **57**, 77

Skrutskie, M. F., Cutri, R. M., Stiening, R., Weinberg, M. D., Schneider, S., Carpenter, J. M., Beichman, C., Capps, R., Chester, T., Elias, J., Huchra, J., Liebert, J., Lonsdale, C., Monet, D. G., Price, S., Seitzer, P., Jarrett, T., Kirkpatrick, J. D., Gizis, J. E., Howard, E., Evans, T., Fowler, J., Fullmer, L., Hurt, R., Light, R., Kopan, E. L., Marsh, K. A., McCallon, H. L., Tam, R., Van Dyk, S., & Wheelock, S.: 2006, *The Two Micron All Sky Survey (2MASS)*, AJ **131**, 1163

Stanford, S. A., Eisenhardt, P. R., Brodwin, M., Gonzalez, A. H., Stern, D., Jannuzi, B. T., Dey, A., Brown, M. J. I., McKenzie, E., & Elston, R.: 2005, *An IR-selected Galaxy Cluster at* $z = 1.41$, ApJL **634**, L129

Strazzullo, V., Paolillo, M., Longo, G., Puddu, E., Djorgovski, S. G., De Carvalho, R. R., & Gal, R. R.: 2005, *Morphology of low-redshift compact galaxy clusters - I. Shapes and radial profiles*, MNRAS **359**, 191

Struble, M. F. & Rood, H. J.: 1999, *A Compilation of Redshifts and Velocity Dispersions for ACO Clusters*, ApJS **125**, 35

Sunyaev, R. A. & Zeldovich, I. B.: 1980, *Microwave background radiation as a probe of the contemporary structure and history of the universe*, ARA&A **18**, 537

Taylor, A. N., Bacon, D. J., Gray, M. E., Wolf, C., Meisenheimer, K., Dye, S., Borch, A., Kleinheinrich, M., Kovacs, Z., & Wisotzki, L.: 2004, *Mapping the 3D dark matter with weak lensing in COMBO-17*, MNRAS **353**, 1176

Thimm, G. J., Röser, H.-J., Hippelein, H., & Meisenheimer, K.: 1994, *The galaxy population in the cluster Cl1409+524 (3C295)*, A&A **285**, 785

Valageas, P., Lacey, C., & Schaeffer, R.: 2000, *Scaling laws in gravitational clustering for counts-in-cells and mass functions*, MNRAS **311**, 234

van Dokkum, P. G., Förster Schreiber, N. M., Franx, M., Daddi, E., Illingworth, G. D., Labbé, I., Moorwood, A., Rix, H.-W., Röttgering, H., Rudnick, G., van der Wel, A., van der Werf, P., & van Starkenburg, L.: 2003, *Spectroscopic Confirmation of a Substantial Population of Luminous Red Galaxies at Redshifts* $z \gtrsim 2$, ApJL **587**, L83 van Dokkum, P. G. & Franx, M.: 2001, *Morphological Evolution and the Ages of Early-Type Galaxies in Clusters*, ApJ **553**, 90

van Dokkum, P. G., Franx, M., Fabricant, D., Illingworth, G. D., & Kelson, D. D.: 2000, *Hubble Space Telescope Photometry and Keck Spectroscopy of the Rich Cluster MS 1054-03: Morphologies, Butcher-Oemler Effect, and the Color-Magnitude Relation at* $z = 0.83$, ApJ **541**, 95

Walsh, J. R.: 1995, in *Calibrating and Understanding HST and ESO Instruments*, pp 27–+

White, S. D. M., Clowe, D. I., Simard, L., Rudnick, G., de Lucia, G., Aragón-Salamanca, A., Bender, R., Best, P., Bremer, M., Charlot, S., Dalcanton, J., Dantel, M., Desai, V., Fort, B., Halliday, C., Jablonka, P., Kauffmann, G., Mellier, Y., Milvang-Jensen, B., Pelló, R., Poggianti, B., Poirier, S., Rottgering, H., Saglia, R., Schneider, P., & Zaritsky, D.: 2005, *EDisCS - the ESO distant cluster survey. Sample definition and optical photometry*, A&A **444**, 365

White, S. D. M. & Frenk, C. S.: 1991, *Galaxy formation through hierarchical clustering*, ApJ **379**, 52

Wolf, C.: 1998, *Ph.D. thesis*, University of Heidelberg

Wolf, C., Meisenheimer, K., Kleinheinrich, M., Borch, A., Dye, S., Gray, M., Wisotzki, L., Bell, E. F., Rix, H.-W., Cimatti, A., Hasinger, G., & Szokoly, G.: 2004, *A catalogue of the Chandra Deep Field South with multi-colour classification and photometric redshifts from COMBO-17*, A&A **421**, 913

Wolf, C., Meisenheimer, K., Rix, H.-W., Borch, A., Dye, S., & Kleinheinrich, M.: 2003, *The COMBO-17 survey: Evolution of the galaxy luminosity function from 25 000 galaxies with* $0.2 < z < 1.2$, A&A **401**, 73

Wolf, C., Meisenheimer, K., & Röser, H.-J.: 2001, *Object classification in astronomical multi-color surveys*, A&A **365**, 660

York, D. G., Adelman, J., Anderson, J. E., Anderson, S. F., Annis, J., Bahcall, N. A., Bakken, J. A., Barkhouser, R., Bastian, S., Berman, E., Boroski, W. N., Bracker, S., Briegel, C., Briggs, J. W., Brinkmann, J., Brunner, R., Burles, S., Carey, L., Carr, M. A., Castander, F. J., Chen, B., Colestock, P. L., Connolly, A. J., Crocker, J. H., Csabai, I., Czarapata, P. C., Davis, J. E., Doi, M., Dombeck, T., Eisenstein, D., Ellman, N., Elms, B. R., Evans, M. L., Fan, X., Federwitz, G. R., Fiscelli, L., Friedman, S., Frieman, J. A., Fukugita, M., Gillespie, B., Gunn, J. E., Gurbani, V. K., de Haas, E., Haldeman, M., Harris, F. H., Hayes, J., Heckman, T. M., Hennessy, G. S., Hindsley, R. B., Holm, S., Holmgren, D. J., Huang, C.-h., Hull, C., Husby, D., Ichikawa, S.-I., Ichikawa, T., Ivezić, Ž., Kent, S., Kim, R. S. J., Kinney, E., Klaene, M., Kleinman, A. N., Kleinman, S., Knapp, G. R., Korienek, J., Kron, R. G., Kunszt, P. Z., Lamb, D. Q., Lee, B., Leger, R. F., Limmongkol, S., Lindenmeyer, C., Long, D. C., Loomis, C., Loveday, J., Lucinio, R., Lupton, R. H., MacKinnon, B., Mannery, E. J., Mantsch, P. M., Margon, B., McGehee, P., McKay, T. A., Meiksin, A., Merelli, A., Monet, D. G., Munn, J. A., Narayanan, V. K., Nash, T., Neilsen, E., Neswold, R., Newberg, H. J., Nichol, R. C., Nicinski, T., Nonino, M., Okada, N., Okamura, S., Ostriker, J. P., Owen, R., Pauls, A. G., Peoples, J., Peterson, R. L., Petravick, D., Pier, J. R., Pope, A., Pordes, R., Prosapio, A., Rechenmacher, R., Quinn, T. R., Richards, G. T., Richmond, M. W., Rivetta, C. H., Rockosi, C. M., Ruthmansdorfer, K., Sandford, D., Schlegel, D. J., Schneider, D. P., Sekiguchi, M., Sergey, G., Shimasaku, K., Siegmund, W. A., Smee, S., Smith, J. A., Snedden, S., Stone, R., Stoughton, C., Strauss, M. A., Stubbs, C., SubbaRao, M., Szalay, A. S., Szapudi, I., Szokoly, G. P., Thakar, A. R., Tremonti, C., Tucker, D. L., Uomoto, A., Vanden Berk, D., Vogeley, M. S., Waddell, P., Wang, S.-i., Watanabe, M., Weinberg, D. H., Yanny, B., & Yasuda, N.: 2000, *The Sloan Digital Sky Survey: Technical Summary*, AJ **120**, 1579

Zwicky, F.: 1933, *Die Rotverschiebung von extragalaktischen Nebeln*, Helvetica Physica Acta **6**, 110

Zwicky, F., Herzog, E., & Wild, P.: 1968, *Catalogue of galaxies and of clusters of galaxies*, Pasadena: California Institute of Technology (CIT), 1961-1968

Acknowledgement

This work would not have been possible without the guidance and advice from colleagues as well as the support from my family and friends. Thank you to all the people that contributed and supported me in all kinds to my scientific career.

I thank Mr. Hermann-Josef Röser for providing the theme of this thesis, the excellent supervision, and the friendly atmosphere.

Moreover, my sincere thanks go to:

> Mr. Hans Hippelein for valuable advice in programming issues, for the advice in scientific problems, and for reading my manuscript,
>
> Mr. Christian Wolf for providing the multi-color classification algorithm, the help and assistance in science questions as well as my job applications,
>
> Mr. Matthias Bartelmann for the appraisal of my PhD thesis,
>
> Mr. Zoltán Kovács for discussions about multi-color classification issues and for providing the data from the COMBO-17+4 survey,
>
> Mrs. Irini Sakelliou for the readiness to discuss scientific problems,
>
> Mr. Klaus Meisenheimer who made available a correction polynomial for the WFI data reduction,
>
> Mr. Michael Zatloukal for the reductions and analysis of the MOSCA spectra of the first HIROCS cluster candidate, and the corrections of my thesis manuscript,
>
> Mr. M. Ramella, Mr. W. Boschin, Mr. D. Fadda, and Mr. M. Nonino for providing the Voronoi tessellation code ”Voronoi Galaxy Cluster Finder”.

The observations of the tertiary standard stars were carried out in service mode at the Calar Alto observatory. Thanks to the staff and the support who provided excellent work. Thanks also for the engagement and support during my observing runs with LAICA.

Part of the HIROCS survey data were taken in service mode at the ESO/MPG 2.2m telescope equipped with the WFI as part of the MPIA guaranteed time. I thank the staff at La Silla observatory who performed the observations.

During the time at the MPIA I experienced a very friendly and stimulating atmosphere. It was a pleasure to work in such a convenient environment. The institute's directorate actively supports the students in addition to the funding of the PhD project. Thank you to the directorate for the financial support of the MPIA Student Workshops in Rügen, Oberau (Austria), and Brixlegg (Austria) and for the outstanding support in general.

Sporting activities like Basketball on Fridays or soccer on Wednesdays, which are traditional activities since years, give the opportunity to come together apart from the institute's business and relax from the daily stress.

Finally, I thank all the students for the help and providing an excellent atmosphere.